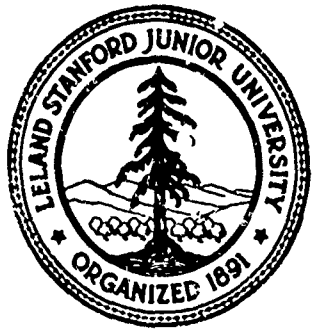

FINAL REPORT

SYNTHESIS OF COMPOUND SEMICONDUCTING MATERIALS AND DEVICE APPLICATIONS

July 1, 1971 - June 30, 1972

Grant No. DAHC15 71-G-9

CMR-72-10

CENTER FOR MATERIALS RESEARCH

STANFORD UNIVERSITY • STANFORD, CALIFORNIA

Final Report

July 1, 1971 - June 30, 1972

Sponsored by
Advanced Research Projects Agency
ARPA Order No. 1644

Program Code Number: POD10

Contractor: Stanford University

Grant No. DAHC15 71-G-9

Principal Investigator: D. A. Stevenson
Phone: (415) 321-2300, Ext. 4251

Co-Investigators:
R. H. Bube, Ext. 2535
R. S. Feigelson, Ext. 4007
G. S. Kino, Ext. 72289
B. L. Mattes, Ext. 2695
W. D. Nix, Ext. 4259
R. K. Route, Ext. 2695
W. A. Tiller, Ext. 2301

Effective Date of Grant: July 1, 1971

Grant Expiration Date: June 30, 1972

Amount of Grant $184,140

Grant Title: Synthesis of Compound Semiconducting Materials and Device Applications

1

Center for Materials Research
Stanford University
Stanford, California 94305
(415) 321-2300, Ext. 4118

TABLE OF CONTENTS

I.	INTRODUCTION	1
II.	EPITAXIAL CRYSTAL GROWTH	3
III.	APPLICATIONS OF COMPOUND SEMICONDUCTOR MATERIALS	16
IV.	PRECIPITATION STUDIES IN COMPOUND SEMICONDUCTORS	31
V.	RELATIONS BETWEEN DISLOCATIONS AND MECHANICAL PROPERTIES AND THE PRODUCTION AND CHARACTERIZATION OF DEFECT STRUCTURES IN COMPOUND SEMICONDUCTORS	36
VI.	SCIENTIFIC ASPECTS OF SEMICONDUCTOR CRYSTAL PREPARATION	46
VII.	VAPOR-PHASE GROWTH OF AlN, GaN AND AlN-GaN SOLID SOLUTIONS	49

I. INTRODUCTION

The present program concerns the synthesis of compound semiconducting materials, with particular emphasis on their use in new and novel microwave devices. The program is divided into three major sections: thin film epitaxial growth of III-V compounds; the design, fabrication and evaluation of microwave devices and fundamental studies of crystal synthesis and properties.

The devices of primary interest are of the planar microwave and acoustical type, employing thin films of GaAs as the active layer. The choice of GaAs was made based on its unique properties: exceptionally high carrier mobility, a moderately large band gap, the Gunn effect and piezoelectric response. These planar devices require high quality active layers of GaAs, with particularly strict requirements on film thickness, surface smoothness, carrier density, and mobility in the film. The layers intended for microwave devices are grown by the liquid phase epitaxial technique.

In the period covered by this report there have been three major accomplishments relating to materials synthesis and device fabrication: growth has been achieved for GaAs films with superior properties for microwave device applications; very thin layers (0.2 - 1.5 μ) of GaAs with optically smooth surfaces have been grown by liquid phase epitaxial techniques; and successful contacts have been made to the GaAs using both an n^+ liquid regrowth technique and an Ag-In-Ge alloy. Research in the closely related microwave acoustic device area has demonstrated the great potential of high mobility GaAs in bulk acoustic and surface acoustic wave devices and interaction techniques. Additional progress has been made in the utilization of this material for microwave space charge device

applications. Also during this period, significant progress has been made on the fundamental studies of crystal synthesis and properties of compound semiconductors. The topics include: observations of precipitation effects in GaAs by transmission electron microscopy; measurement of electrical property changes in GaAs induced by changes in dislocation density; a theoretical analysis of the GaAs/liquid gallium interface and a study of the vapor growth of GaN, AlN and GaN - AlN solid solutions. A description of the progress in these areas is given below.

II. EPITAXIAL CRYSTAL GROWTH

R. S. Feigelson, B. L. Mattes, R. K. Route, J. Yen, and P. Petit

A. PROGRAM OBJECTIVE

The principal objective of the epitaxial crystal growth program is the preparation of high quality, uniform and reproducible epitaxial layers of GaAs for the device applications program. The device program requires layers (not obtainable commercially) that have carrier densities in the low 10^{14} cm^{-3} to 10^{15} cm^{-3} range, 300°/77°K mobilities above 7000/50,000 cm^2/V-sec, thicknesses in the .5-30 μm range, and optically smooth surfaces. All of these requirements are being achieved in the present work by liquid phase epitaxial techniques.

In order to meet this objective, considerable effort has been devoted to the development of new methods of growth, the study of variables that influence growth, techniques to prepare and handle materials involved in growth, and methods to evaluate the growth and its properties. In addition, the epitaxial crystal growth program is coordinated with the materials studies and device applications programs to prepare materials with specific properties and dimensions and to interact on problems of mutual concern.

The most recent objective of this program is to develop reliable ohmic contacts for epitaxial layers that have carrier densities in the 10^{14} cm^{-3} range. There is also a continued effort to improve the quality of the GaAs layers in anticipation of more stringent device requirements.

The future objectives of the epitaxial crystal growth program will be: (1) to meet the device application and materials study program requirements for III-V materials with specific properties; (2) to continue

the development and evaluation of ohmic contacts on GaAs epitaxial layers; (3) to continue the analysis of the liquid phase growth process, in particular, nucleation; and (4) to develop new techniques for growing epitaxial GaAs on oxide substrates.

B. PROGRESS

1. Achievements

High quality GaAs epitaxial layers, that meet the critical property requirements for the device application program, have been grown by the liquid phase epitaxial method. The epitaxial crystal growth achievements that led to this objective are (1) improvements in the purity of the growth system and materials--to yield low 10^{14} cm^{-3} carrier density material with 300/77°K mobilities of 8000/60,000 cm^2/V-sec; (2) refinements in the temperature gradient cell--to yield layers with uniformity in thickness from .5 to 30 μm and with optically smooth surfaces; (3) n^+ contacts on low carrier density layers--to yield excellent ohmic contacts; and (4) a direct relation between surface terracing and temperature gradient--to yield information on the nucleation process on the substrate. These achievements demonstrate the success and potential of the liquid phase epitaxial method for the growth of high quality layers that in the past were only achieved by the vapor phase epitaxial method. Over 200 GaAs layers were grown for this program, and are listed in Table II-1. The majority of the layers were grown as part of the study of growth variables involved with the liquid phase epitaxial process. With the control of these variables, reproducible high quality layers and n^+ contacts are now being grown.

A detailed study of the liquid phase growth process has shown that a temperature gradient normal to the substrate increases the nucleation sites on the substrate. Thus, with control of the gradient and uniformity of the substrate temperature, extremely smooth uniformly thick layers are obtained. Because of this it appears that nucleation and growth are controlled by interface attachment kinetics and are not diffusion limited.

2. Growth Method

Epitaxial Layers

A temperature gradient cell was developed to study surface morphologies in the liquid phase growth process. The cell provides a very controllable means to establish a temperature gradient normal to the liquid-solid interface. Since the epitaxial layers grown in this cell have been consistently uniform in thickness, optically smooth and controllable in thickness from 2 μm to 20 μm in thickness, the cell is now used exclusively for all growths.

The Temperature Gradient Cell

The temperature gradient cell is designed to provide a temperature gradient normal to the substrate, Figure II-1, and to be used in a conventional horizontal tilt system, Figure II-2. The cell consists of a graphite growth cell that floats on a liquid Ga reservoir contained in a graphite cradle, and a quartz heat transfer tube which is immersed in the Ga reservoir. The temperature gradient is produced by forcing a suitable cooling gas, such as He or N_2, through the heat transfer tube. The liquid Ga reservoir serves two purposes: (1) to maintain intimate thermal contact between the boat and the heat transfer tube, and (2) to improve the temperature uniformity under the substrate.

The principal features of the temperature gradient cell include: (1) the bottom of the growth cell under the substrate which is machined very flat and thin (~0.8 mm) to decrease the thermal resistance; (2) a graphite lid which is used on the growth cell to act as a susceptor and to minimize H_2 flow turbulence in the cell; (3) the growth cell which is partitioned on the bottom to separate the Ga from both the substrate and the source during bakeout and saturation procedures; and (4) an expansion space which is allowed for in the cradle to develop a head of Ga in the reservoir that will maintain Ga in contact with the bottom of the growth cell.

Operation

The temperature gradient cell is used in a horizontal tilt system as shown in Figure II-2. The furnace is (1) stabilized in temperature to saturate the Ga solvent with As from a GaAs source; (2) tilted to roll the As-saturated Ga solution onto the GaAs substrate; and (3) cooled to epitaxially grow GaAs on the substrate from the As-saturated Ga solution. The temperature gradient is induced in the cell during the saturation period. This insures that when the As-saturated Ga solution is rolled onto the substrate, a temperature gradient will exist normal to the substrate and the Ga solution will be close to the temperature of the substrate.

To produce the temperature gradient, a controlled flow of He or N_2 is passed through the quartz heat transfer tube. The temperature gradient is determined by monitoring the difference between the temperature outside the cell and in the Ga reservoir. Once the desired temperature gradient is achieved, the saturation temperature is regulated by varying the He flow with the furnace temperature controller at a predetermined

setpoint. The temperatures are monitored with inconel sheathed chromel-alumel thermocouples inserted in quartz tubes.

The temperature gradient in the growth cell was actually measured during the initial evaluation of the cell. Thermocouples, in separate quartz tubes, were located on and 3 mm above the substrate, as well as in the Ga reservoir. A calibration for the temperature gradient vs. He flow is shown in Figure II-3. It was observed that the temperature gradient increased by 1°C/cm above the substrate when the As-saturated Ga solution was rolled onto the substrate for a He flow of 28 liters/min. This indicates that a definite gradient exists during the initiation of growth.

The temperature gradient cell can be used for both transient and steady-state methods of liquid phase growth. The majority of the growths have been by the former, where the furnace is initially cooled at a rate from 300°C/hr to 3000°C/hr from a saturation temperature in the 500°C to 750°C range. Since no means is provided to wipe the Ga solution off the substrate during growth, the thickness of the epitaxial layer is determined principally by the amount of As dissolved in the Ga at the saturation temperature, Figure II-4. The saturation temperature thus provides an accurate means to vary the layer thickness from .2 μm to 20 μm.

n^+ Contacts

The temperature gradient cell and techniques are also used for the n^+ contact growths. The Ga solution is heavily doped with Sn, an n-type dopant that produces a shallow donor level. Since the distribution coefficient of Sn is quite small, $<10^{-4}$, substantial amounts $\geq$ 10 atomic % Sn are required to obtain carrier densities of 5×10^{17} cm^{-3} or greater.

The cell is cooled rapidly during the growth process to insure a uniform carrier density throughout the thickness of the n^+ layer.

To localize the contact regions, an SiO_2 mask is deposited on the layer by silane decomposition or vacuum sputtering techniques. Photoresist techniques are next used to selectively remove unwanted portions of the mask and the n^+ contact material is then grown in the holes in the SiO_2 mask. At present, studies are underway to determine the minimum size and shape limits for the n^+ contact definition. Typical n^+ contact layers are approximately 0.5 μm thick, corresponding to convenient SiO_2 mask thicknesses varying from 0.3 μm to 0.5 μm.

3. Growth Studies

Nucleation and Terracing

A temperature gradient normal to the liquid-solid interface appears to increase the density of nucleation sites on the substrate. This deduction follows from the observations that the terrace width is the same as the spacing between nuclei[1] and decreases as temperature gradient is increased, Figure II-5. The terrace width is uniform over the entire layer surface, with the terraces extended in the form of long ripples. The terraces extend normal to a [100] direction on (100) and (110) substrate orientations and a [112] direction on (111) A and B orientations.

The decrease in terrace width with an increase in the temperature gradient appears to be related to the effect of thermal fluctuations on the liquid solid-interface. It will be shown later that the temperature fluctuation could arise from the heat of formation during nucleation. Figure II-6 illustrates this effect in terms of a thermal fluctuation, $\pm \Delta T$, and a gradient, G, superimposed on the interface temperature, T_f, at the position of the liquid-solid interface, Z. The perturbation on

the interface position, ΔZ, is given by

$$\Delta Z = \frac{\Delta T}{G-S} \quad , \qquad \text{(II-1)}$$

where S is the derivative of the interface temperature with interface position during growth. This assumes that the gradient G is constant and the same in both phases.

A detailed model on the nucleation and terracing, based on the nuclei spacing and terrace width, and the long ripple form of the terraces, is shown in Figure II-7. If ΔZ, from Figure II-6, represents the depth of melt-back over a diffuse liquid-solid interface region, $\delta - \rho$ in Figure II-7, then $\Delta Z \sim \Delta X/2$, for $\rho \ll \delta$.

To partially confirm this model, a plot of $\Delta X/2$ vs. $1/G$ is shown in Figure II-8. Assuming that $G \gg S$ in equation (II-1), the slope from Figure II-8 gives a fluctuation temperature ΔT to be approximately 5×10^{-3} °C. For smaller gradients, than included in Figure II-8, the slope decreases and limits according to equation (II-1). This evaluation of ΔT assumes that (1) the measured temperature gradient is the same as the gradient G at the interface and (2) the position of the interface is not kinetically limited, i.e., the growth velocity is determined by the rate of cooling and/or thermal fluctuation rate.

The scatter in the data, shown in Figure II-8, is due to variations in S, equation (II-1), which is determined by the saturation temperature and cooling rate during the initial stages of growth. Although the cooling rate and saturation temperature are controllable during growth, their actual control during nucleation is difficult to achieve. Their combined effect preceding nucleation is related to supercooling. If the initial saturation temperature and cooling rate are not consistently

applied during the initiation of growth the terrace width may range from 10 μm to 500 μm with or without a temperature gradient.

The height of the terraces, Δh in Figure II-7, appears to be directly related to the terrace width. Because of this, the height might indicate the size of nuclei that are spontaneously formed when the As-saturated Ga is supercooled on the substrate. Optical interferometric measurements indicate that the height is approximately 1/1000th of the terrace width.

Any interpretation of $\Delta T \sim 5 \times 10^{-3}$ °C, obtained from Figure II-8, must explain the following: (1) the terrace height and width ; (2) the independence of ΔT on an activation volume associated with the height x width x length of the terraces; and (3) the long parallel terraces normal to a particular direction for different substrate orientations. A plausible interpretation is given below.

A thermodynamic model based on the heat of formation, ΔH, evolved during nucleation on the substrate appears to account for $\Delta T \sim 5 \times 10^{-3}$ °C if the following assumptions are made: (1) the diffuse liquid-solid interface region, Figure II-7, develops from the ΔH evolved by each nucleus; (2) the nuclei are stably centered and spaced by the diffuse interfacial regions so that there is no appreciable overlap--nuclei formed within $\delta - \rho$ would tend to melt back; (3) the rate of cooling, R, is less than $\Delta T/\tau$, where τ is the period of a fundamental growth step, e.g., nucleation rate--for $R > \Delta T/\tau$ only a fraction of ΔH would be available to melt back $\delta - \rho$; and (4) the nucleus' radius, ρ, is approximately the terrace height or $\rho \sim \delta/500$. The temperature rise from the formation of nucleus is given by

$$\Delta T = \frac{\Delta H}{c_p} \quad , \qquad \text{(II-2)}$$

where ΔH is the heat of formation and c_p is the specific heat. Since ΔH is assumed to be distributed over the region $\delta - \rho$, in Figure II-7, the actual temperature rise of this region is given by

$$\Delta T = \frac{\Delta H}{c_p}\left(\frac{\rho}{\delta}\right)^2 , \qquad \text{(II-3)}$$

where $\rho/\delta = 1/500$. The heat of formation and specific heat for GaAs at $1000^{o}K$ are $\Delta H = 4308$ cal/mole and $c_p = 6.6$ cal/mole ^{o}C.[2] Substituting these values into equation (II-3) gives

$$\Delta T = 2.6 \times 10^{-3}\ ^{o}C.$$

This value for the thermal fluctuation is in excellent agreement with experiment, $\Delta T \sim 5 \times 10^{-3}\ ^{o}C$, considering that the above calculation was not rigorously evaluated.

The preceding thermodynamic model appears to be plausible, even though a number of assumptions were made. Within these limitations, the terrace height and width and the independence of ΔT on an activation volume have been explained. The general terrace formations and their orientation, however, are probably related to interface attachment kinetics, where the terraces are restricted to line up parallel to a (100) plane for all orientations. Why one (100) plane is preferentially selected over another is not known at present. However, this may be related to a slight misorientation of the substrate. This observation is based on different growths from the same batch of substrates that yield the same terrace orientations.

Layer Thickness

Another growth study was the correlation between the layer thickness

and the atom fraction of As in liquid Ga for a given saturation temperature, using the liquidus line from Hall's data on the Ga-As phase diagram,[3] shown in Figure II-4. It should be noted that (1) the liquidus line parallels the layer thickness very closely above 600°C; (2) the measured thickness of the layer is less than the theoretical thickness because of the excess GaAs formation on the surface of the Ga solution in the growth cell--approximately 1/2 of the total amount of GaAs dissolved in the solvent; and (3) below 600°C the thickness falls off very fast--this is the region where hillocks sometimes form on the substrate and/or layer and large numbers of platelets form in the liquid during growth.

Heteroepitaxial Growth

A preliminary attempt has been made to grow GaAs on a $(1\bar{1}02)$ Al_2O_3 substrate in the temperature gradient cell. The result, Figure II-9, was a large number of randomly oriented hillocks rigidly attached to the substrate. If the nucleation density can be increased and the orientation of the hillocks controlled by the proper selection of substrate lattice parameters, a heteroepitaxial layer is possible.

Electrical Studies

Preliminary measurements on the n^+ contacts have shown good ohmic contacts to 10^{15} cm^{-3} layers. Contacts to lower carrier density and submicron layers are now in progress. Extensive Schottky barrier and I-V studies are planned as part of the evaluation process. The carrier density of the n^+ contact material is about $5x10^{17}$ cm^{-3} and the doping is very uniform throughout the contact layer. No insulating barriers have been observed between the contact and the active layer, even though melt-back was not allowed during deposition.

Considerable uncertainties occur whenever van der Pauw and Schottky barrier measurements are attempted on low carrier density layers less than 2 μm thick. This is due to a depletion region which forms next to the substrate. The Schottky barrier then behaves as a Mott barrier and shows little sensitivity to forward or reverse bias.

C. PROPOSED FUTURE WORK

The future objectives of the epitaxial crystal growth program will be to (1) maintain the present capability for preparing material for new device requirements; (2) evaluate and develop electrical contacts on high purity material for device applications; (3) study and analyze growth variables in the liquid phase epitaxial process; and (4) develop liquid phase techniques for growing III-V materials on oxide substrates.

The basic responsibility of the epitaxial crystal growth program is to provide materials that will meet specific property and dimensional requirements for the device program. Therefore, the growth program must maintain a flexible capability to meet new requirements, which may include other III-V materials and their alloys. The facilities and technology for this capability have been established for GaAs but it may be extended to certain other III-V materials and their ternary solid solutions. The preparation of other materials may require the development of new growth methods, substrate preparation techniques and more detailed analyses of the growth conditions. For the majority of the device requirements, however, GaAs will be the primary material.

The study of electrical contact problems will continue. The new contacting procedures will be further developed for liquid phase grown n^+ contacts on n-type layers. The horizontal temperature gradient

process provides thin uniform n^+ contacts on n-type layers without insulating layers at their interface. These features are necessary for precise photomasking-etching procedures, and minimal contact resistance between the contact and active layer. Certain alloy contacts, such as Au-Ge and Ag-In-Ge, will also be pursued for some applications. It is proposed to study their deposition and electrical contact to the layer by investigating the surface states on the layer, their wettability to the layer, and their diffusion into the layer. The scanning electron microscope in the current scan mode will be used as a very sensitive means to study the uniformity and performance of the contacts.

A continued effort will be made to study the variables that control growth in the liquid phase epitaxial process. Since the surface morphology is determined by (1) the temperature at the start of growth, (2) the temperature gradients, (3) the rate of cooling, and (4) the substrate preparation, it appears that the morphology is related to the initial stages of nucleation. There is not only heterogeneous nucleation (growth on the substrate) but homogeneous nucleation (growth in the solvent) as well. The latter may be important in hillock formation that frequently occurs under certain conditions. If the process of nucleation were well understood, more efficient techniques for epitaxial growth could be pursued to tailor growths for special device requirements. There will also be a continued effort to analyze the impurities in the layers to achieve higher mobilities and lower carrier densities. It is essential to know the impurities and their source if high quality GaAs is to be produced to meet device requirements. Low frequency noise measurements will be used to evaluate the suitability of the material for device applications.

Detailed studies of growth phenomena involved in liquid phase epitaxial processes have led to our ability to prepare high quality GaAs layers. Use of the present techniques and modification of growth variables will extend our capability of controlling the growth of layers and perhaps even allow the growth of GaAs layers on insulating, piezoelectric and thermally conducting substrates, such as Al_2O_3, $LiNbO_3$ and BeO, respectively. Heteroepitaxial techniques such as these will generate the material for, and allow the design of many new devices which have so far been impossible to realize. Growth of a GaAs layer on an insulator will give better isolation between devices on the same substrate. Growth of a GaAs layer on a piezoelectric substrate will give stronger coupling of acoustic or piezoelectric modes to the carriers in the active layer. Growth of a GaAs layer on a good thermal conductor that is an electrical insulator will allow larger power handling capabilities for planar devices.

REFERENCES

II-1. Semi-Annual Technical Report, "Synthesis of Compound Semiconducting Materials and Device Applications", AD-738 470, ARPA Contract No. DAHC15-71-G-9, Stanford University, July 1, 1971 - December 31, 1971.

II-2. B. D. Lichter and P. Sommelet, Trans. Met. Soc. AIME 245, 1021 (1969).

II-3. R. N. Hall, J. Electrochem. Soc. 110, 385 (1963).

TABLE II-1

GaAs EPITAXIAL LAYER PROPERTIES

Growth No.*	Substrate Orientation†	Mobility RT/LN $cm^2/V\text{-}sec$	Carrier Density cm^{-3}	Thickness μm	Surface Morphology‡
139	(111)B	4,700/14,000	2×10^{16}	15	MT
140	(111)B	4,700/13,000	2×10^{16}	15	MT
141	(100)	Substrate Melt Back			
142	(100)	5,800/32,000	5×10^{15}	25	MT + GI
143	(100)	4,500/16,000	1×10^{16}	15	CT + GI
144	(111)B	5,600/25,000	5×10^{15}	21	MT
145	(111)B	5,700/44,000	9×10^{14}	23	CT
146	(111)B	6,200/46,000	4×10^{14}	15	MT
147	(111)B			15	MT
148	(111)B				MT + GI
149	(111)B				MT
150	(111)B	4,600/30,000	1×10^{15}	15	MT + GI
151	(111)B	5,500/31,000	4×10^{15}	15	FT + GI
152	(111)B	Surface Evaporation Study			
153	(111)B	Surface Evaporation Study			
154	(111)B	Surface Evaporation Study			

TABLE II-1 (cont.)

GaAs EPITAXIAL LAYER PROPERTIES

Growth No.*	Substrate Orientation†	Mobility RT/LN $cm^2/V\text{-}sec$	Carrier Density cm^{-3}	Thickness μm	Surface Morphology‡
155	(111)B	Substrate Melt Back			
156	(100)	Surface Evaporation Study			
157	(100)				FT
158	(111)A	Surface Evaporation Study			
159	(100)			15	FT + H
160	(111)A	4,700/30,000	4×10^{15}	27	FT
161	(100)	4,300/15,000			FT + GI
162	(100)	4,000/8,100	2×10^{16}	19	FT
163	(100)	5,400/26,000	7×10^{15}	21	ET
164	(111)B (LD)	5,200/23,000	8×10^{15}	20	ET
165	(111)B (LD)	4,400/31,000	2×10^{15}	24	ET
166	(111)B (LD)	4,500/16,000	1×10^{16}	22	ET
167	(111)B	4,200/15,000	7×10^{15}	30	FT
168	(111)B	5,500/17,000	2×10^{15}	15	FT
169	(111)B (LD)	2,600/7,400	5×10^{15}	20	ET + GI
170	(111)B (LD)	3,900/17,000	1×10^{16}	24	

TABLE II-1 (cont.)

GaAs EPITAXIAL LAYER PROPERTIES

Growth No.*	Substrate Orientation†	Mobility RT/LN $cm^2/V\text{-}sec$	Carrier Density cm^{-3}	Thickness μm	Surface Morphology‡
171	(100)			25	H
172	(100)			25	H
173	(100)	4,400/15,000	2×10^{16}	15	MT + GI
174	(111)B (LD)	3,900/32,000	6×10^{15}	25	ET
175	(100)				H
176	(111)B	4,600/12,000	3×10^{16}	14	MT
177	(100)	Surface Evaporation Study			
178 TG	(100)	5,200/21,000	1×10^{16}	13	FT + GI
179 TG	(100)	4,200/18,000	2×10^{16}	18	NT
180	(100)			20	H
181 TG	(111)A	6,300/8,800	4×10^{16}	10	ET
182 TG	(111)B (LD)	2,700/4,400	8×10^{15}	26	ET
183	(111)B (LD)	6,000/35,000	3×10^{15}	57	ET
184 TG	(100)	6,900/33,000	5×10^{15}	19	ET
185	(100)	4,800/12,000	3×10^{16}	16	FT + GI
186	(100)	3,800/8,400	2×10^{16}	14	MT + GI

TABLE II-1 (cont.)

GaAs EPITAXIAL LAYER PROPERTIES

Growth No.*	Substrate Orientation†	Mobility RT/LN $cm^2/V\text{-}sec$	Carrier Density cm^{-3}	Thickness μm	Surface Morphology‡
187 TG	(100)	2,300/3,700	6×10^{16}	6	MT + H + GI
188	(100)	3,300/5,600	1×10^{17}	8	FT + GI
189 TG	(100)	1,500/			H
190	(100)	1,500/	3×10^{16}	12	CT + H
191	(100)	3,900/6,700	3×10^{16}	9	MT + GI
192 TG	(100)	Substrate Melt Back			
193	(100)	3,300/6,600	3×10^{16}	17	MT + GI
194	(100)	3,100/13,000	2×10^{16}	13	CT
195 TG	(100)	5,600/16,000	1×10^{16}	20	ET + GI
196 TG	(100)	6,000/16,000	1×10^{16}	17	ET
197 TG	(100)	5,100/15,000	2×10^{16}	16	NT
198	(100)	5,800/21,000	7×10^{15}	30	ET
199 TG	(100)	5,600/17,000	8×10^{15}	20	NT
200	(100)	6,000/49,000	1×10^{15}	26	FT
201	(100)	5,900/28,000	3×10^{15}	47	FT
202 TG	(100)	5,400/25,000	3×10^{15}	26	ET

TABLE II-1 (Cont.)

GaAs EPITAXIAL LAYER PROPERTIES

Growth No.*	Substrate Orientation†	Mobility RT/LN cm^2/V-sec	Carrier Density cm^{-3}	Thickness μm	Surface Morphology‡
203 TG	(100)	5,500/30,000	1×10^{15}	20	MT + GI
204	(100)	4,600/13,000	2×10^{16}	25	MT
205	(111)B			25	ET
206 TG	(111)B	5,500/16,000	7×10^{15}	20	NT
207	(111)B	7,400/14,000	2×10^{16}	25	CT
208 TG	(111)B	3,600/7,100	4×10^{15}	6	NT
209	(111)B	5,800/24,000	1×10^{15}	25	MT
210	(111)B (LD)	5,800/32,000	3×10^{15}	9	ET
211 TG	(111)B	3,100/4,500	9×10^{16}	3	NT
212	(111)B	5,500/31,000	2×10^{15}	10	MT
213 TG	(111)B	6,400/23,000	3×10^{15}	3	NT
214	(111)B			25	FT
215 TG	(111)B	5,300/14,000	7×10^{15}	3	NT
216 TG	(111)B	4,900/8,900	6×10^{16}	2	NT
217	(111)B	7,100/22,000	9×10^{15}	18	CT
218	(111)B	7,000/34,000	2×10^{15}	18	ET

TABLE II-1 (Cont.)

GaAs EPITAXIAL LAYER PROPERTIES

Growth No.*	Substrate Orientation†	Mobility RT/LN $cm^2/V\text{-}sec$	Carrier Density cm^{-3}	Thickness μm	Surface Morphology‡
219	(111)B	8,000/53,000	8×10^{14}	22	ET
220	(111)B	7,800/59,000	5×10^{14}	12	ET
221 TG	(111)B	4,100/16,000	8×10^{15}	1	NT
222	(111)B	6,600/35,000	1×10^{15}	2-9	ET
223	(111)B	5,800/37,000	1×10^{14}	18	ET + H + GI
224 TG	(111)B n^+		2×10^{15}	3	NT
225	(111)B	6,400/26,000	7×10^{15}	22	ET
226	(111)B	6,500/59,000	5×10^{14}	18	ET + GI
227	(100)	8,200/50,000	5×10^{14}	10	FT
228	(100)	8,000/54,000	1×10^{15}	15	ET
229 TG	(111)B	3,100/	3×10^{17}	3	NT
230	(111)B	7,200/51,000	6×10^{14}	5-17	FT
231	(111)B			25	FT + GI
232	(111)B	8,200/51,000	6×10^{14}	15	FT
233 TG	(111)B	4,700/11,000	2×10^{15}	25	NT
234	(111)B	6,100/30,000	5×10^{15}	20	ET

TABLE II-1 (cont.)

GaAs EPITAXIAL LAYER PROPERTIES

Growth No.*	Substrate Orientation†	Mobility RT/LN $cm^2/V\text{-}sec$	Carrier Density cm^{-3}	Thickness μm	Surface Morphology‡
235 TG	(111)B	6,700/31,000	2×10^{15}	22	ET
236	(111)B	6,600/39,000	3×10^{15}	15	ET
237	(111)B	6,400/36,000	2×10^{15}	10-25	FT
238 TG	(111)B	6,111/22,000	1×10^{15}	16	NT + H
239	(111)B	7,000/36,000	2×10^{14}	10	FT
240	(111)B	6,400/34,000	2×10^{15}	15	FT
241 TG	(111)B	6,200/30,000	2×10^{15}	5-10	NT
242	(111)B	6,500/	3×10^{15}	20	FT
243	(111)B	3,300/	1×10^{15}	25	MT
244	(111)B	--	--	22	MT
245	(111)B	5,000/19,000	6×10^{14}	35	MT
246 TG	(111)B	5,200/12,000	5×10^{16}	13	ET
247 TG	(111)B	6,000/34,000	4×10^{15}	7	NT
248	(111)B	--	--	22	FT
249 TG	(111)B	6,300/29,000	--	--	ET
250 TG	(111)B	6,700/22,000	1×10^{16}	11	NT

TABLE II-1 (cont.)

GaAs EPITAXIAL LAYER PROPERTIES

Growth No.*	Substrate Orientation†	Mobility RT/LN $cm^2/V\text{-}sec$	Carrier Density cm^{-3}	Thickness μm	Surface Morphology‡
251	(111)B	5,200/22,000	8×10^{14}	21	FT
252	(111)B	6,800/33,000	2×10^{15}	13	MT
253 TG	(111)B	5,200/16,000	2×10^{16}	10	ET + H
254	(111)B	6,600/34,000	2×10^{15}	17	CT
255 TG	(111)B	6,000/22,000	3×10^{16}	8	ET
256	(111)B	6,500/24,000	1×10^{15}	15	FT
257	(111)B	--	--	18	FT
258	(111)B	--	--	17	FT
259 TG	(110)	6,900/21,000	2×10^{16}	1	NT
260 TG	(110)	7,600/28,000	1×10^{16}	1.5	ET
261	(111)B	6,300/21,000	2×10^{16}	2.5	MT
262 TG	(111)B	6,900/7,500	8×10^{16}	1	NT
263	(111)B	6,000/24,000	5×10^{15}	17	MT
264	(111)B	250/16,000	3×10^{15}	15	MT
265 TG	(111)B	1,900/9,400	4×10^{14}	2	ET
266	(111)B	0/11,000	2×10^{16}	17	MT

TABLE II-1 (cont.)

GaAs EPITAXIAL LAYER PROPERTIES

Growth No.*	Substrate Orientation†	Mobility RT/LN $cm^2/V\text{-}sec$	Carrier Density cm^{-3}	Thickness μm	Surface Morphology‡
267 TG	(111)B	6,500/23,000	--	--	NT
268	(111)B	5,200/16,000	9×10^{14}	18	MT
269	(111)B	--	--	1[illegible]	MT
270	(111)B	5,900/20,000	1×10^{16}	17	CT
271	(111)B	6,600/33,000	2×10^{15}	12	MT
272	(111)B	6,600/21,000	7×10^{15}	15	MT
273	(111)B	6,600/30,000	1×10^{15}	15	MT
274	(111)B	7,200/34,000	3×10^{15}	9	MT
275	(111)B	6,600/27,000	3×10^{15}	15	FT
276	(111)B	5,100/27,000	4×10^{15}	11	MT
277	(111)B	7,200/32,000	1×10^{15}	15	CT
278	(111)B	7,100/41,000	7×10^{15}	18	CT
279	(111)B	4,900/28,000	6×10^{14}	19	CT
280	(111)B	6,000/22,000	4×10^{15}	16	MT
281 TG	(111)B	8,000/22,000	1×10^{16}	4	NT
282 TG	(111)B	--	--	--	NT

TABLE II-1 (cont.)

GaAs EPITAXIAI LAYER PROPERTIES

Growth No.*	Substrate Orientation†	Mobility RT/LN $cm^2/V\text{-}sec$	Carrier Density cm^{-3}	Thickness μm	Surface Morphology‡
283 TG	(111)B	--/27,000	2×10^{15}	0.8	ET
284 TG	(111)B	--	3×10^{16}	0.8	ET
285	(111)B	--	2×10^{16}	18	CT
286 TG	(111)B	--	8×10^{17}	0.4	ET
287	(111)B	5,900/25,000	4×10^{15}	20	CT
288 TG	(111)B	4,900/20,000	3×10^{16}	5	ET
289 TG	(111)B	7,400/43,000	3×10^{15}	4	ET
290	(111)B	5,200/32,000	6×10^{15}	19	CT
291 TG	(111)B	6,200/39,000	1×10^{15}	2.8	ET
292	(111)B	6,000/66,000	9×10^{14}	19	CT
293 TG	(100) n^+	--	8×10^{14}	16	FT
294 TG	(111)B	5,900/26,000	1×10^{16}	5	ET
295	(111)B	6,300/46,000	3×10^{15}	17	CT + GI
296	(111)B	7,000/54,000	2×10^{15}	17	CT + GI
297 TG	(111)B	6,100/28,000	1×10^{16}	10	ET
298	(111)A	--	--	15-25	CT

TABLE II-1 (cont.)

GaAs EPITAXIAL LAYER PROPERTIES

Growth No.*	Substrate Orientation†	Mobility RT/LN $cm^2/V\text{-}sec$	Carrier Density cm^{-3}	Thickness μm	Surface Morphology‡
299 TG	(111 A	7,400/34,000	1×10^{16}	6	17
300	(111)B	7,000/45,000	2×10^{15}	23	CT
301 TG	(111)B	6,800/40,000	3×10^{15}	6	11
302	(111)B	6,500/44,000	1×10^{15}	23	CT + GI
303 TG	(100) n^+	--	6×10^{14}	13	14
304	(111)B	7,200/44,000	2×10^{15}	18	CT
305 TG	(100) n^+	--	1×10^{15}	15	14
306	(111)B	6,500/31,000	6×10^{15}	15	CT
307 TG	(100) n^+	--	2×10^{14}	13	10
308 TG	(110)	--	--	1.6	8
309 TG	(111)B	6,400/27,000	6×10^{15}	3	12
310	(111)B	5,500/20,000	2×10^{16}	17	MT
311 TG	(111)B	6,000/26,000	9×10^{15}	12	NT
312 TG	(111)B	7,200/30,000	4×10^{15}	4	11
313 TG	(111)B	8,000/40,000	2×10^{15}	10	8
314 TG	(111)B	7,500/29,000	4×10^{15}	4	7

TABLE II-1 (cont.)

GaAs EPITAXIAL LAYER PROPERTIES

Growth No.*	Substrate Orientation†	Mobility RT/LN $cm^2/V\text{-}sec$	Carrier Density cm^{-3}	Thickness μm	Surface Morphology‡
315 TG	(111)B	4,900/21,000	7×10^{15}	4	5
316 TG	(111)B	5,000/32,000	3×10^{15}	4	6
317 TG	(111)B	4,700/30,000	5×10^{15}	4	5
318 TG	(110)	--	$\sim 10^{15}$	--	8
319 TG	(110)	8,500/37,000	3×10^{15}	2.5	10
320 TG	(110)	--	--	1.2	11
321 TG	(110)	6,300/21,000	2×10^{16}	0.8	7
322 TG	(111)B	--	$\sim 10^{15}$	2.7	8
323 TG	(111)B	--	$\sim 10^{15}$	0.7	8
324 TG	(100)	--	6×10^{15}	1.5	12
325 TG	(111)B	--	4×10^{15}	2	10
326 TG′	(111)B	--	--	--	FT
327 TG	(111)B	4,300/12,000	9×10^{15}	1.2	11
328 TG′	(111)B	7,100/46,000	2×10^{15}	24	FT
329 TG	(100)	--	3×10^{15}	2.2	9
330 TG′	(111)B	--	--	--	MT + GI

TABLE II-1 (cont.)

GaAs EPITAXIAL LAYER PROPERTIES

Growth No.*	Substrate Orientation†	Mobility RT/LN $cm^2/V\text{-}sec$	Carrier Density cm^{-3}	Thickness μm	Surface Morphology‡
331 TG	(111)B	2,800/2,800	4×10^{17}	0.8	8
332 TG′	(111)B	7,000/27,000	7×10^{15}	2.6	ET
333 TG	(100) n^+	--	5×10^{15}	8	8
334 TG′	(111)B	5,400/12,000	5×10^{16}	1.1	FT
335 TG	$1\bar{1}02$ Al_2O_3	--	--	--	H
336 TG	(111)B	4,900/16,000	2×10^{16}	2.6	8
337 TG	(111)B	5,900/19,000	1×10^{16}	4	9
338 TG′	(111)B	2,000/3,200	5×10^{16}	3	FT
339 TG	(111)B	5,000/21,000	5×10^{15}	5	10
340 TG	(111)B	2,800/14,000	4×10^{15}	2.6	FT + GI
341 TG′	(111)B	3,600/7,300	2×10^{16}	2	FT
342 TG	(111)B	6,600/29,000	6×10^{15}	7	15
343 TG′	(111)B	1,300/3,500	--	~ 0	FT
344 TG	(111)B	2,900/11,000	1×10^{16}	4	22
345 TG′	(111)B	2,200/3,700	--	~ 0	FT
346 TG	(111)B	--/16,000	7×10^{15}	1.4	36

TABLE II-1 (cont.)

GaAs EPITAXIAL LAYER PROPERTIES

Growth No.*	Substrate Orientation†	Mobility RT/LN $cm^2/V\text{-}sec$	Carrier Density cm^{-3}	Thickness μm	Surface Morphology‡
347 TG′	(111)B	3,300/3,600	--	< 1	16
348 TG′	(111)B	4,200/7,000	2×10^{16}	2.5	12
349 TG	(111)B	6,800/35,000	4×10^{15}	7	7
350 TG	(111)B	5,600/28,000	4×10^{15}	7	13
351 TG′	(111)B	n^+ Contacts Through SiO_2 Mask			
352 TG	(111)B	6,200/34,000	4×10^{15}	7	14
353 TG	(111)B	6,000/36,000	4×10^{15}	18	18
354 TG	(100)	6,500/27,000	6×10^{15}	11	17
355 TG′	(111)B	n^+ Contacts Through SiO_2 Mask			
356 TG′	(111)B	2,200/--	5×10^{17}	2	6
357 TG′	(111)B	2,700/2,500	2×10^{17}	2.4	10
358 TG	(111)A	Substrate Melt Back			
359 TG′	(111)B	2,000/2,000	8×10^{17}	0.25	10
360 TG	(111)A	Substrate Melt Back			
361 TG	(111)A	6,100/30,000	5×10^{15}	11	11
362 TG	(111)B	5,400/26,000	7×10^{15}	10	18

TABLE II-1 (cont.)

GaAs EPITAXIAL LAYER PROPERTIES

Growth No.*	Substrate Orientation†	Mobility RT/LN $cm^2/V\text{-}sec$	Carrier Density cm^{-3}	Thickness μm	Surface Morphology‡
363 TG	(111)B	7,000/39,000	4×10^{15}	9.9	10
364 TG	(111)B	7,000/42,000	3×10^{15}	6.8	11
365 TG	(111)B	6,600/35,000	6×10^{15}	7.1	14
366 TG	(111)B	6,600/38,000	1×10^{15}	20	13
367 TG'	(111)B	n^+ Contacts Through SiO_2 Mask			
368 TG	(111)B	6,700/32,000	4×10^{15}	9	11
369 TG'	(111)B	--	--	--	ET
370 TG	(111)B	7,100/39,000	4×10^{15}	8.3	15
371 TG	(111)B	5,900/19,000	2×10^{16}	12	14

* *All growths noted with a TG were grown in temperature gradient cell.

†All substrates were semi-insulating unless noted as n^+ . All substrates noted with an (LD) were 15° off the (111) direction.

‡CT: coarse terraces; MT: medium terraces; FT: fine terraces; ET: extremely fine terraces; NT: no terraces; GI: gallium inclusions; H: hillocks; terrace width, (μm).

Figure Captions

Figure II-1. Details of the temperature gradient cell.

Figure II-2. Horizontal tilt system with temperature gradient cell in place.

Figure II-3. Dependence of the temperature gradient normal to the substrate on the He flow through the heat transfer tube.

Figure II-4. Epitaxial layer thickness as a function of the saturation temperature. The atom fraction of As required to saturate liquid Ga (after Hall) is used to calculate the layer thickness assuming that all the GaAs comes out of solution onto the substrate.

Figure II-5. Surface terraces that formed (a) without a temperature gradient on growth No. 261; and (b) with a 15°C/cm temperature gradient on growth No. 315. The terrace heights on the surface are 0.1 μm and <0.01 μm, respectively. Interference contrast.

Figure II-6. The effect of a temperature gradient, G, on the perturbation of the interface position, $\mp\Delta Z$, due to a thermal fluctuation, $\pm\Delta T$, at an interface temperature T_f.

Figure II-7. A detailed model of the nucleation on the substrate and the resultant surface terraces. It is proposed that each nucleus is surrounded by a diffuse liquid-solid interface region.

Figure II-8. The slope of the terrace width/2 vs. the reciprocal of the temperature gradient, for large gradients, gives the fluctuation temperature $\Delta T = 5 \times 10^{-3}$°C.

Figure II-9. Growth No. 335 shows randomly oriented GaAs hillocks rigidly attached to a $(1\bar{1}02)$ Al_2O_3 substrate.

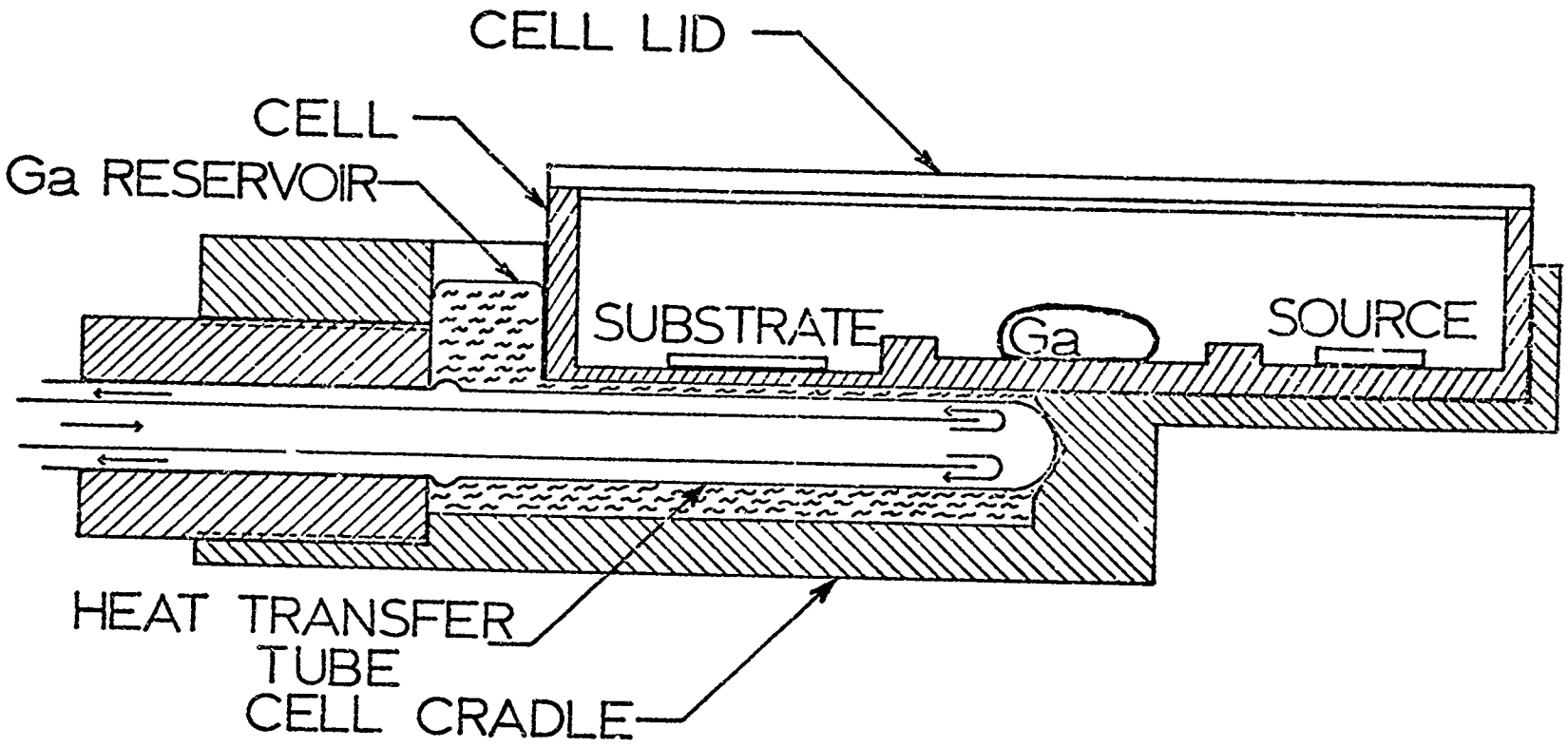

Figure II-1 Details of the temperature gradient cell.

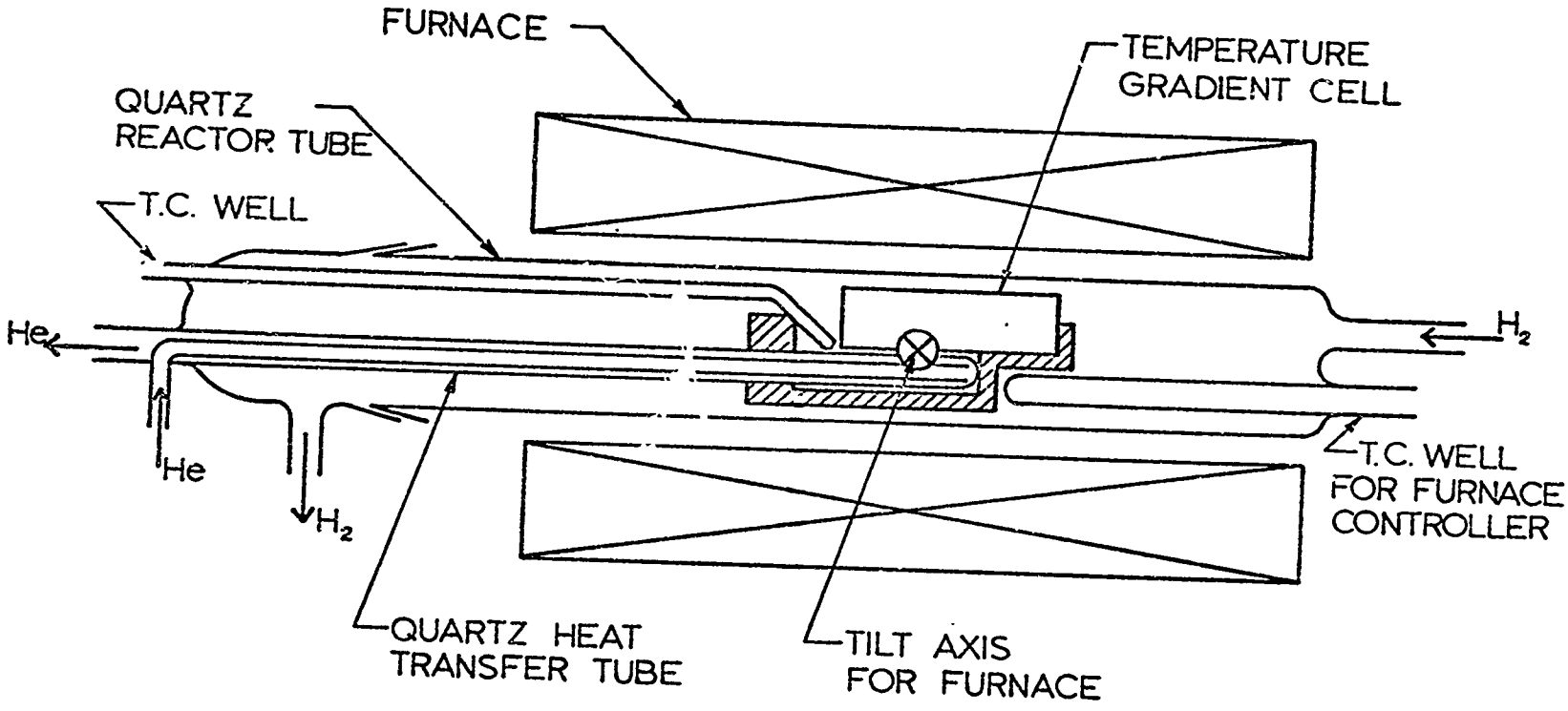

Figure II-2 Horizontal tilt system with temperature gradient cell in place.

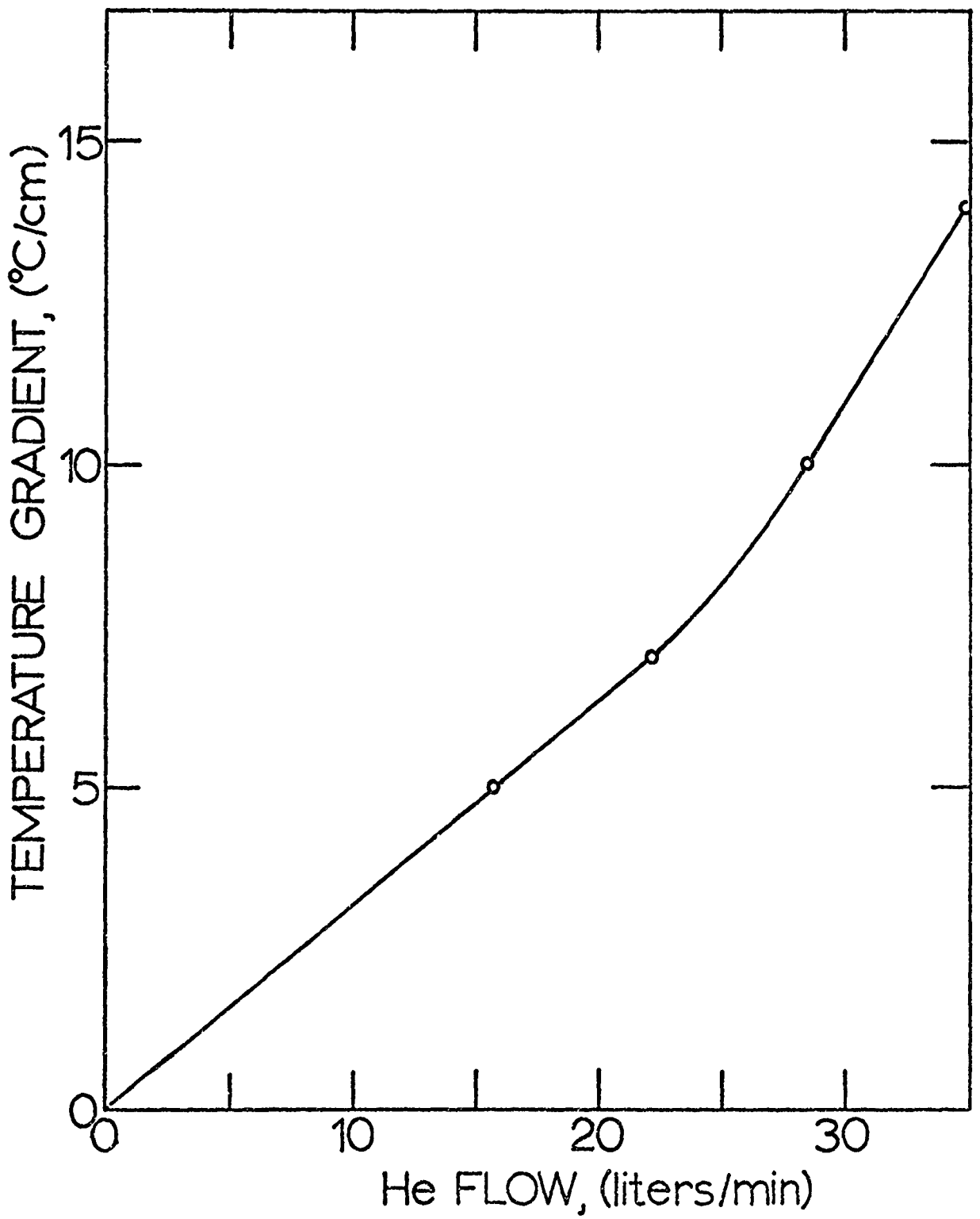

Figure II-3 Dependence of the temperature gradient normal to the substrate on the He flow through the heat transfer tube.

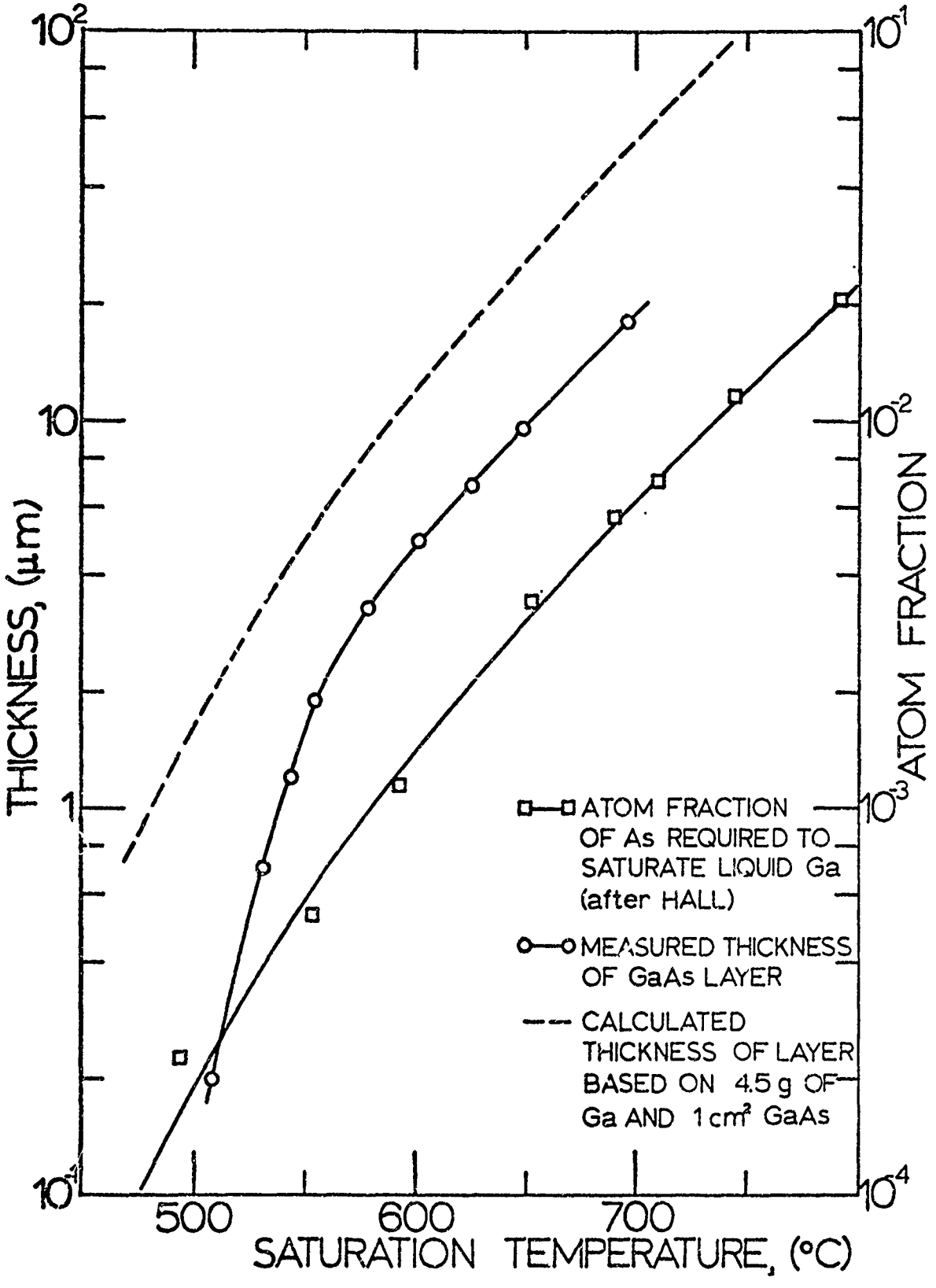

Figure II-4 Epitaxial layer thickness as a function of the saturation temperature. The atom fraction of As required to saturate liquid Ga (after Hall) is used to calculate the layer thickness assuming that all the GaAs comes out of solution onto the substrate.

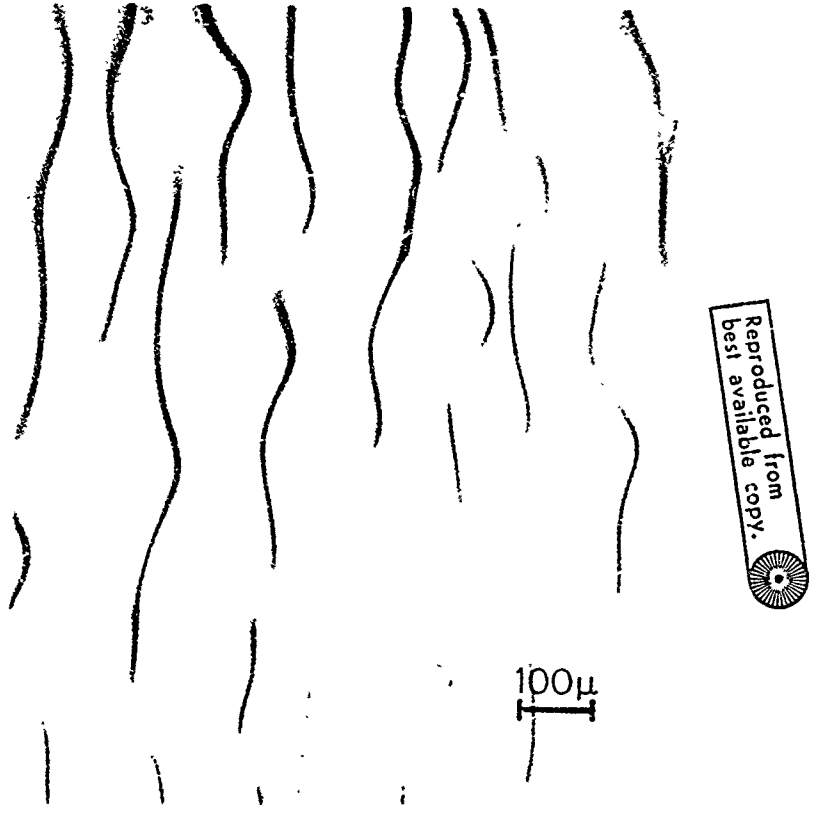

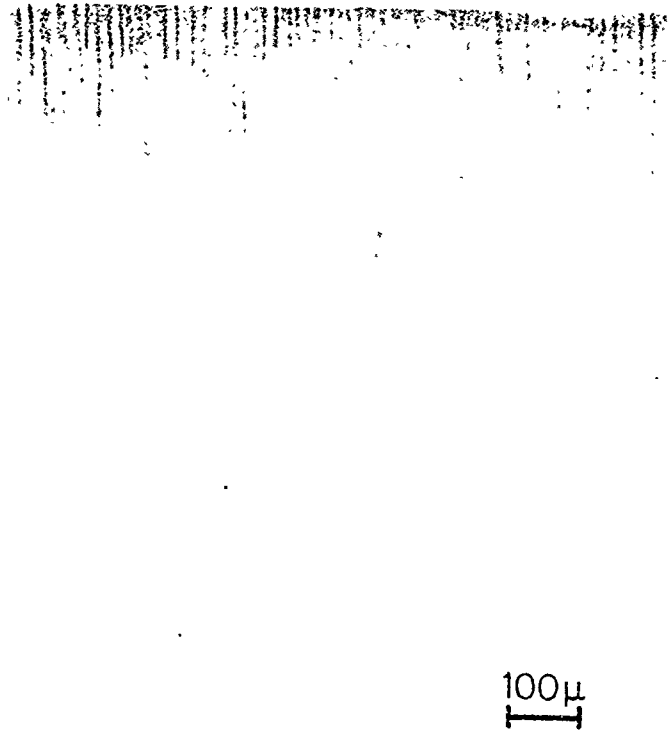

Figure II-5 Surface terraces that formed (a) without a temperature gradient on growth No. 261, and (b) with a 15 °C/cm temperature gradient on growth No. 315. The terrace heights on the surface are 0.1 μm and <0.01 μm, respectively. Interference contrast.

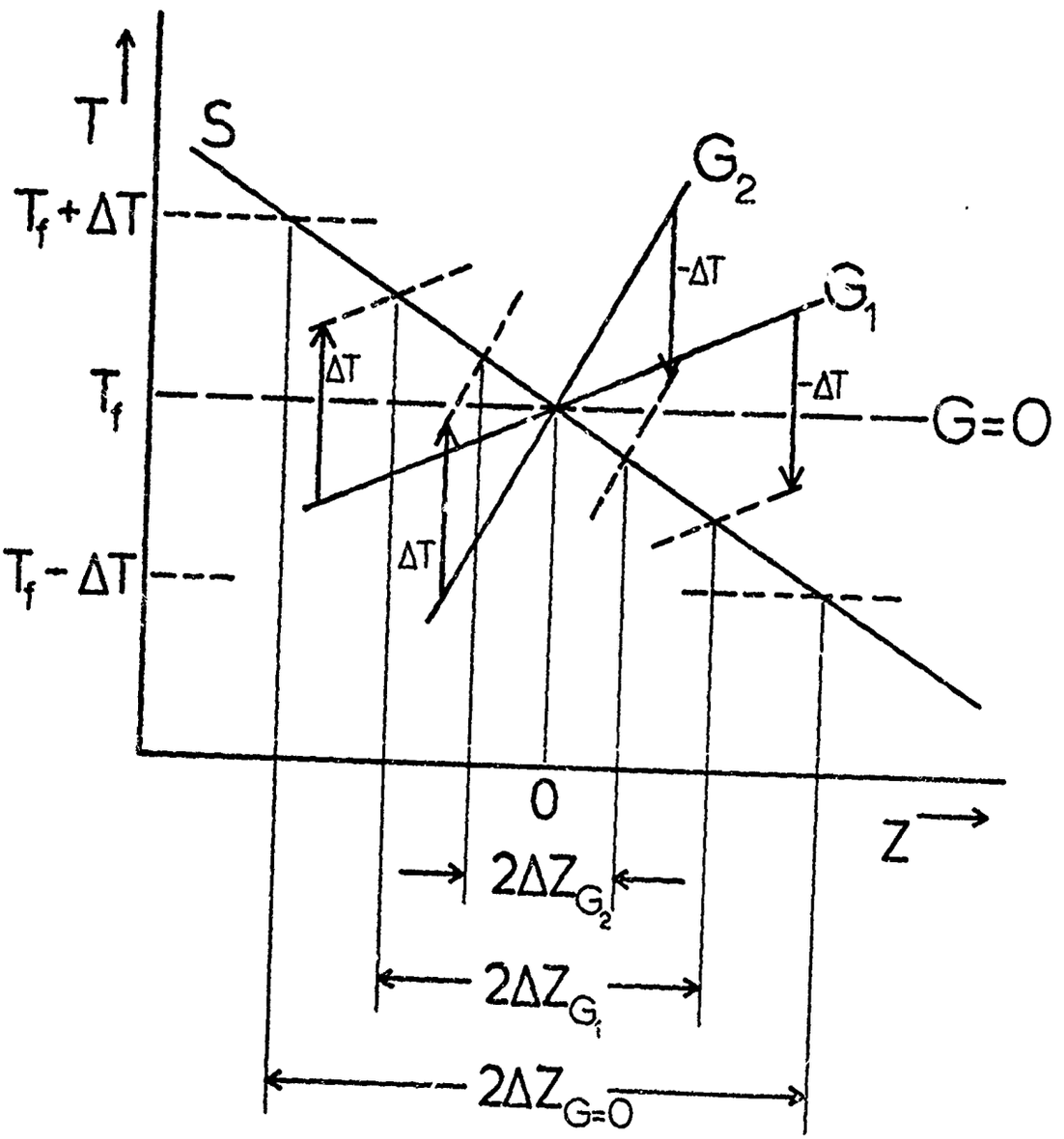

Figure II-6 The effect of a temperature gradient, G, on the perturbation of the interface position, $\mp \Delta Z$, due to a thermal fluctuation, $\pm \Delta T$, at an interface temperature T_f.

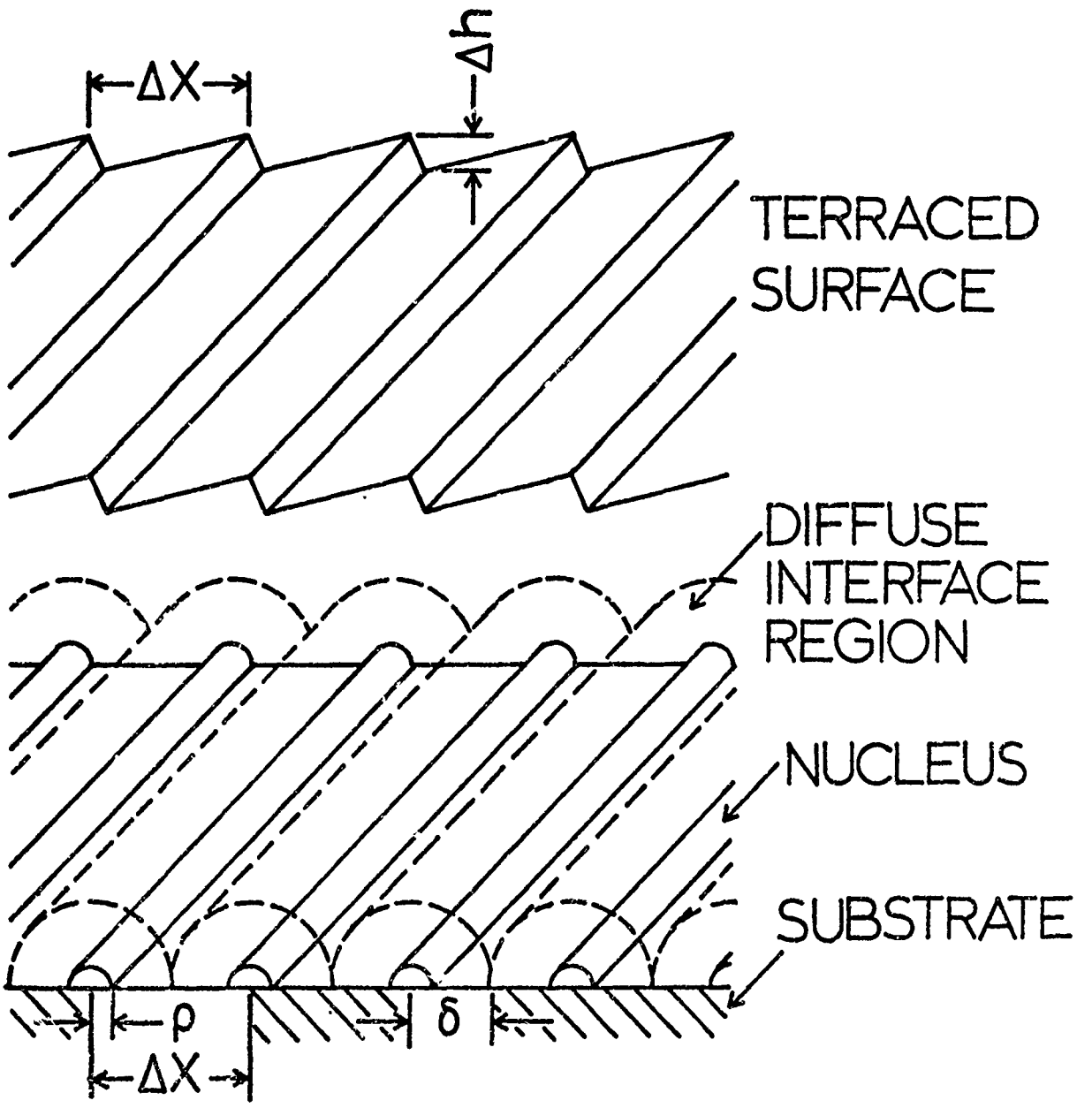

Figure II-7 A detailed model of the nucleation on the substrate and the resultant surface terraces. It is proposed that each nucleus is surrounded by a diffuse liquid-solid interface region.

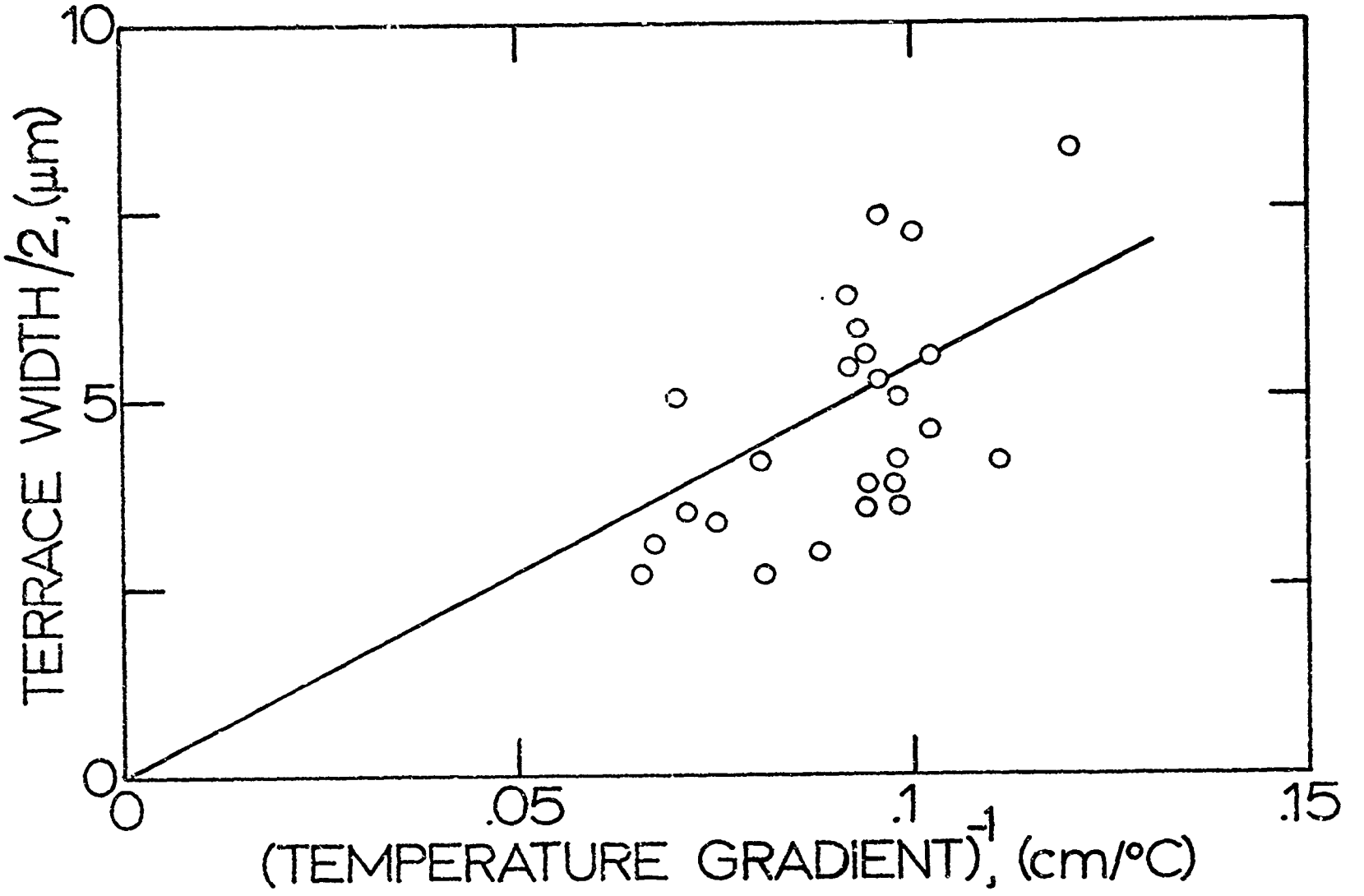

151

Figure II-8 The slope of the terrace width/2 vs the reciprocal of the temperature gradient, for large gradients, gives the fluctuation temperature $\Delta T = 5 \times 10^{-3}$ °C.

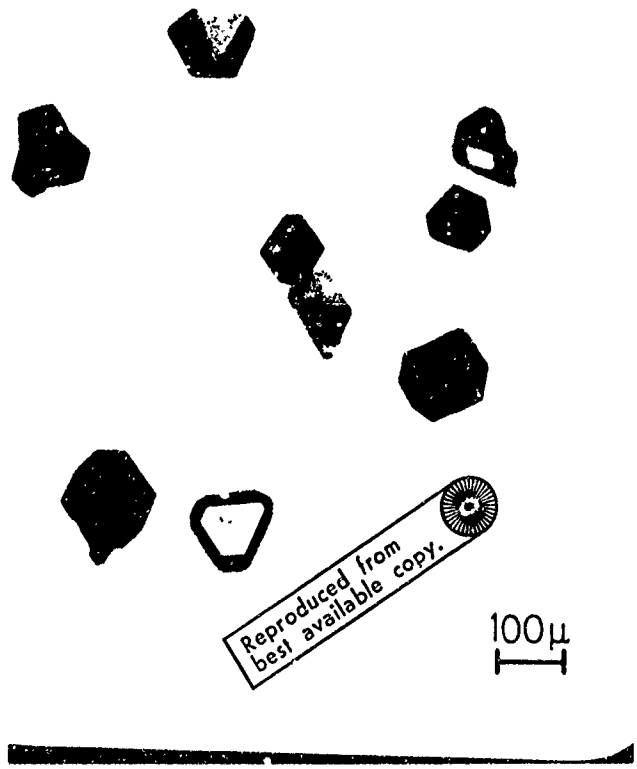

Figure II-9 Growth No. 335 shows randomly oriented GaAs hillocks rigidly attached to a $(1\bar{1}02)$ Al_2O_3 substrate.

III. APPLICATIONS OF COMPOUND SEMICONDUCTOR MATERIALS

G. S. Kino, C. Quate, M. Bini, G. R. Bisio,
A. Chiabrera, and S. Ludvik

A. GENERAL OBJECTIVES

The purpose of this work is to design and fabricate new and unique microwave space charge and acoustical devices. We are interested primarily in planar devices in which the conduction is along a thin film of GaAs deposited on a semi-insulating substrate. These devices are fabricated using modifications of silicon integrated circuit technology, and for their successful realization we require high quality GaAs epitaxial material of specific thickness and carrier density on high quality substrates having several different orientations. These requirements are unique and, hence, make a closely integrated materials growth effort essential to the success of the program.

B. PROGRESS TO DATE AND FUTURE WORK

1. Gallium Arsenide Space Charge Devices

During the past reporting period additional progress has been made on the unilateral space charge amplifier program, after some initial difficulties with the contact technology and material quality. The material requirements are typically for high quality GaAs layers 0.2-20 μm thick with carrier densities in the 10^{14}-10^{15} cm^{-3} range deposited on semi-insulating substrates. The material must be of very high quality in order to be resistant to avalanching in the contact regions where high fields inevitably occur. Furthermore, the substrate-active layer interface must be free of defects and impurities in order that breakdown through or along the substrate may be avoided. Finally, the surface of the epitaxial layers must be smooth enough that photomasking techniques having

sub-micron resolution may be used; the devices are by necessity quite small, the width being of the order of 1 mm and the length 1-100 μm.

Several months ago a limited quantity of exceptionally high quality GaAs material meeting all three of our requirements became available from the Center for Materials Research (CMR) crystal growth effort of this program. With this material we have been able to construct for the first time devices which show no signs of avalanche at the contacts nor any indication of substrate-interface breakdown or substrate "punch through" breakdown. Before this, we had tried epitaxial GaAs material from a number of other sources (mostly commercial, but including earlier CMR growth facility material) and in no instance was the material quality high enough nor was our contacting technology perfected to the point where we could construct a diode that would saturate without oscillation and without breakdown.

We are currently using an Ag-In-Ge evaporated alloy in our photomasking procedure to make the ohmic contacts to the new high quality material. Previously, we had developed an evaporated Au-Ge alloy contact and we could make good contacts to epitaxial material having $n > 10^{15}$ cm^{-3}. However, for the lower density, high quality material required for the present devices, the Au-based alloy does not seem to be adequate. Part of the problem may be the fact that the Au film tends to "ball up" during the alloying step, reducing the effective area of the contact and increasing localized fields. With the Ag-based alloy this is not a problem, even though the alloying temperature is higher (500°C). Using this new alloy we are now able to make very good quality ohmic contacts to the lower carrier density, higher quality material.

The goal of the unilateral space charge amplifier program is the

design and construction of a solid state equivalent to the traveling wave tube for use at X band and higher frequencies. For the design of these devices we have performed detailed calculations of the exact dc field distribution within a thin epitaxial diode using the empirically measured velocity-field characteristics for GaAs. These calculations show that the dc field increases monotonically from the cathode to the anode, passing through the threshold point for negative differential mobility approximately one third of the way from the cathode for a long diode biased just above threshold, as shown in Figure III-1. We see then that to make a successful microwave amplifier, the input of signal must be injected as close as possible to the threshold point at a level well above the background noise level there. Also, the total gain of the device must be limited in order to prevent Gunn oscillations or saturation on noise originating in the cathode region.

A few devices based on these calculations have been constructed, two batches of amplifiers with the rf input on an insulated gate and one batch with the rf input on a Schottky-barrier gate. The first kind is in the form of an insulated gate field effect transistor with <u>two</u> evaporated aluminum gates instead of a single one, as shown in Figures III-2 and III-3. The gates are capacitively coupled to the active material through a thin SiO_2 layer. The longer, grounded gate in conjunction with an active layer nd product $< 10^{12}$ (n is the carrier density in number cm^{-3} and d is the layer thickness in cm) is intended to suppress oscillations by limiting the total gain to a value of less than 50 db. The size of this electrode also determines the input and output impedances. The narrow, upstream gate is used to inject the rf signal which is then detected at the drain electrode. The narrow gate is positioned so that

the input signal is injected just at the beginning of the negative differential mobility range. The total device represents the first solid state equivalent of the conventional traveling wave tube with a calculated gain of perhaps 40 db in the frequency range 8-12 GHz.

Two batches of devices having insulated rf gates were made from two CMR epitaxial GaAs layers, wafer I with $n = 8 \times 10^{14}$ cm^{-3}, $\mu \approx 8000$ cm^2/V-sec, thickness $d \approx 10\,\mu$m and wafer II with $n = 3 \times 10^{14}$ cm^{-3}, $\mu \approx 8000$ cm^2/V-sec, thickness $d \approx 10\,\mu$m. All devices were 70 μm long with the longer gate 35 μm long, the shorter gate 5 μm long and 5 μm spacing between gates and contacts. With batch I, due to alignment problems, the spacing between the long gate and the drain in the final device was 10 μm. Typically, we made approximately 9 devices at a time (three rows of three) on a substrate. The contacts were good in all but 1 out of 18 devices (a device near the edge of one of the substrates). Some of the smaller gates, 5 μm wide, had breaks so that the yield was 5 good devices from batch I and 4 from batch II. Our first devices constructed from the CMR epitaxial material have yielded some rather encouraging results. The source-drain I-V characteristics show very flat current saturation with no coherent Gunn oscillations, as shown in Figure III-4. Incoherent noise is emitted at voltages significantly above threshold as expected. Terminal resistances are in agreement with values calculated for the active region, showing that there is low contact resistance and that the active region thickness corresponds closely to the actual layer thickness. So far, we have not seen any gain from the initial devices because our first estimates for the best position of the input gate were incorrect and because a capacitively coupled rf input is inherently weak. The incoherent noise was observed in the frequency range 4-12 GHz, and is nothing more than

highly amplified background noise. This means that the original dimensions chosen give a little too much gain and that the input signal is not being injected at the optimum point. (It is difficult practically to locate the optimum point because of the inevitable nonuniformities in any real device.) The threshold voltages for onset of noise and for saturation seemed to be very consistent between all devices from batch I, and lower than for devices from batch II which were again consistent among themselves. However, the threshold current and the low field resistances of the devices did vary from one to the other by as much as 20%. We believe that this is due to nonuniform thickness of the epitaxial layer rather than contact problems. We have operated these devices so far on a pulsed basis rather than dc, because the power dissipation is of the order of 2 watts. An increase in the duty cycle tends to lead to excessive heating. However, at no time have we experienced problems with breakdown of the semiconductor material or contacts up to the point of melting. The only breakdown problems in pulsed devices have been due to breakdown in the SiO_2 caused by application of excessive voltages. These results are encouraging indeed, considering that this was the first test on devices in which the technology was reliable enough to give good physical measurements.

Though these devices did not function properly as amplifiers, we were able to make use of them to obtain some preliminary information on the dc field distribution along the devices. To do this, we mounted an electrically etched tunsten filament onto the tip of a high-impedance oscilloscope probe. The probe impedance is 1 megohm in parallel with 1.7 pfarad. The tungsten filament is about 10 μ in diameter and it is bent into the shape of a hook. By using a micropositioner we lowered

this filament onto the large gate of the device. Both gates were allowed to float. We then fed the drain-source contacts with dc pulses, 200 nsec in width. The circuit is shown in Figure III-5. Because both gates are insulated from the GaAs layer by SiO_2, we relied upon the capacitive coupling between the epitaxial layer and the large gate to provide us with a direct measurement of the average potential of the epitaxial layer immediately below the large gate.

In the first experiments we found that the capacitance to the surrounding epitaxial GaAs of the pad attached to the large gate was shorting out our signal, so we carefully scratched away the connection between the pad and the gate at the position labeled "A" in Figure III-2. This result implied also that the large pad on the rf input gate would short out in the rf input signal. So, in the subsequent device design of batch III we have drastically reduced the pad size and in other devices will etch away the semiconductor layer beneath the pad.

Returning to Figure III-1, it is evident that most of the potential drop above the threshold potential will be developed very near the drain. If we consider the drain-to-source voltage V_{ds} vs. the drain-to-gate voltage V_G, we would expect that for V_{ds} below the threshold voltage V_T, a curve of V_{ds} vs. V_G would be a straight line. However, as V_{ds} exceeds the threshold V_T, the curve should slope sharply upward because all the additional voltage drop appearing across the device will occur between the grounded gate and the drain.

In Figure III-6 we show a plot of the value of V_G measured on the probe vs. V_{ds} taken with the circuit shown in Figure III-5. It will be noted that the curve does, indeed, double its slope for $V_{ds} > V_T \cong 30$ volts. This indicates, as expected, that most of the potential drop is near the drain electrode, and that a better means of controlling the

field variation along the device is needed.

To utilize the same technique to extract more detailed knowledge of the field along a device, we have made a photolithographic mask which will be used to deposit a series of narrow insulated gates in the region between the source and drain. A diagram of the configuration is shown in Figure III-7. This configuration will allow us to probe the potentials at several positions along the device.

We are also working on a moveable probe which will eliminate the need for vacuum deposition of gates on the device's surface. Such a probe will allow us to measure the dc potential at any point along any diode at will. We have added one other improvement to our probe which should allow much more accurate potential readings: we have very carefully constructed a stainless steel tip which surrounds the tungsten and very effectively shields it from the leads which go to the source and the drain, eliminating pick-up from the bias circuitry.

In the previous report we suggested that one way of controlling the dc field distribution along a device would be to use a back-biased Schottky-barrier as an input rf gate. A longitudinal view and the associated circuitry of such a device are shown in Figure III-8. The additional control of the dc field distribution is obtained with the adjustable dc bias on the rf input gate. During this present reporting period we have designed and built a batch of such Schottky-barrier amplifiers incorporating a much-reduced pad size on the rf input gate. A schematic diagram and an actual photo are shown in Figure III-9. In this latest design, the gap between ohmic contacts is 35 μm. The input gate is 5 μm long and has a small pad to reduce the capacitive coupling to ground. The grounded gate is 15 μm long and the SiO_2 layer is 5,000 Å

thick. Figure III-10 indicates the fabrication sequences of a batch of such devices. We hope to test these amplifiers in the near future, pending the construction of new input circuitry and mechanical mounting to the Schottky barrier input gate.

We are presently carrying out experiments on etching techniques to remove the GaAs semiconducting layer from underneath the pad region. This appears to be a controllable process , so that we should, in the next set of devices, be able to obtain reasonable size pads to which we can bond gold wires, without undue problems with the pad capacity.

2. Linear Acoustic Amplifiers

In our last report we showed that appreciable electronic gain was possible using GaAs as an acoustoelectric amplification medium for a particular type of surface wave, the Bleustein mode. Following these results, our main objective in this area has been to improve the acoustic transducer coupling so that an overall device gain can be achieved for the amplifier. Additional work has also been done on a comparison of the amplification characteristics of another type of surface wave, the Rayleigh mode.

There are two methods we have been considering for improving the transducer efficiencies. The most promising at this stage relies on a volume longitudinal wave to surface shear wave conversion at a reflecting boundary using the configuration shown in Figure III-11. The angle of the boundary is chosen so that the phase velocities of the two waves match. The launching transducer employed is a ZnO thin film which, with present technology, is readily capable of conversion efficiencies in the range of 15 dB. This compares with conversion efficiencies of 25-30 dB

for typical interdigital transducers which have been employed in earlier investigations.

At the output end of the amplifier, the surface shear wave is reconverted by a similar mode conversion back to a longitudinal wave for detection. Our study to the present on this transducer configuration has been with O_2 doped GaAs in the form of platelets 0.020" thick. In view of the small cross-section of the crystal we expect a surface shear-type wave to propagate along the length. A second advantageous property of ZnO transducers is the extremely large bandwidth ($\geq$200 MHz) available. So far, the basic principle of mode conversion outlined above has been demonstrated experimentally and further investigations are proceeding to establish the amplification properties of the structure.

Another technique for improving the transducer coupling efficiency makes use of thin layers of a good piezoelectric material deposited on the semiconductor surface. This approach is essentially the inverse of earlier surface wave amplifier structures where one used a good piezoelectric substrate and superimposed a semiconducting film. Our work using this method is at a preliminary stage, although other investigations[1] have indicated promising results at frequencies below 100 MHz.

We have pointed out that the amplification characteristics of the surface shear, or Bleustein wave, come from its deep penetration depth and from the particle motion being essentially the same as the strongly coupled bulk shear wave propagating in the <110> direction. Along the same direction of propagation, but instead on the (001) surface, it is possible to excite a pure Rayleigh wave which by contrast has two particle motions. We have investigated the amplification characteristics of this Rayleigh wave mode on material similar to that used for the Bleustein

wave device and from Figure III-12 it is apparent that a smaller amplification is obtained for this case. The approach used for the measurement of Rayleigh wave amplification was similar to that used previously, where the temperature of the sample was adjusted to produce the carrier concentration yielding maximum gain. The lower gain obtained for the Rayleigh wave is partly due to the weaker coupling of this mode to the longitudinal drift field, but it is also due to the greater sensitivity of this mode to sample homogeneity and surface imperfections since most of the acoustic fields are confined to a narrow region just below the surface.

3. Nonlinear Interaction of Surface Waves on GaAs

There has been considerable interest recently in mechanisms producing nonlinear interactions of both acoustic surface and bulk waves in piezoelectric crystals. Much of the effort in this area has been largely to isolate suitable materials and structures for application to various signal processing schemes, such as real time convolution, which can be conveniently achieved through acoustic wave interactions. Among the interactions which have been reported are the direct acoustic nonlinearity[2,3] arising out of departures from Hooke's law at large strains, and also interactions[4,5] produced by the presence of carriers in a piezoelectric semiconductor. Other approaches[6] have involved placing a semiconductor near the surface of a strong piezoelectric, where again the main source of nonlinear interaction occurs from the carriers in the semiconductor.

In the following we present some results on nonlinear coupling processes which occur for surface waves in GaAs. Such interactions have

been observed both for surface shear waves on bulk material and for Rayleigh waves on epitaxial material. It has been found necessary to introduce different processes to describe the coupling for the two cases, but for both situations the nonlinear coefficient for the same internal acoustic power level has been demonstrated to be around 30 dB greater than for the more strongly piezoelectric materials, such as $LiNbO_3$, where the nonlinear effect results from large strains.

Nonlinear Interaction of Surface Shear (Bleustein) Waves in GaAs

The configuration for studying the nonlinear interaction is shown in Figure III-13. Surface waves which are launched at either end of the crystal are allowed to interact in the central region between the two electrodes across the semiconductor. The lower contact is ohmic while the upper consists of a Schottky barrier contact. The material used in these investigations was O_2 doped GaAs with room temperature resistivity of 222 ohm cm. The convolution signal is detected on the center electrode at the second harmonic frequency.. The nonlinear interaction strength is measured by using two oppositely traveling pulses which both have the same width as the detecting electrode. The convolution output in this case has a triangular form and the peak value is used to determine the nonlinear figure of merit. We refer to two definitions of figure of merit. One is based[7] on overall device quantities which are the actual electrical input and output powers:

$$K_e \equiv \frac{P_3}{P_1 P_2 \ell^2} \quad w^{-1} \; cm^{-2}$$

where P_1, P_2, P_3 are the electrical powers at the device terminals and ℓ is the length of the interaction region. It is also useful to have a

definition which is not dependent on the input transducer efficiency or propagation loss and we call this the electroacoustic figure of merit:

$$K_{ea} \equiv \frac{P_3}{P_1^a P_2^a \ell^2} \quad w^{-1} \; cm^{-2}$$

where P_3 is still the electrical output power but P_1^a , P_2^a are the acoustic powers in the crystal.

The convolution property has been checked over a 25 dB range and has been found to be quite linear (± 0.2 dB), P_3 ranging linearly with P_1 and P_2. No saturation was observed up to acoustic power levels of 1 mw, the current limit due to interdigital transducer efficiency. The electrical output power P_3 showed a strong dependence on temperature as the sample was cooled but a broad maximum occurred at low temperatures. This effect shown in Figure III-14 has been determined for fixed electrical and acoustic powers into the device, where the latter is obtained by allowing for the variation of the transducer and propagation losses. The details of this characteristic are not yet clearly understood, but it is associated with the rapidly varying carrier concentration.

The convolution signal is not symmetrical with respect to the dc bias applied to the detecting electrode. For the low carrier concentrations and high trap densities in the material used for these devices there was no consistent behavior of the convolution signal with dc bias. In one case it was found that in the forward bias direction the signal increased while in the reverse direction the signal initially increased but then decreased with increasing bias. In another, the signal decreased in the forward direction but increased in the reverse direction. These effects may be attributed to a variation of the zero bias depletion

layer thickness in relation to the potential associated with the surface wave. The position of the zero field depletion layer is a function of the carrier density and can be strongly influenced by traps.[8]

Nonlinear Interaction of Rayleigh Waves in Epitaxial GaAs

One of the difficulties in interpreting fully the surface shear wave interaction has been due to the high level of trapping in the bulk O_2 doped material which makes the initial depletion layer conditions uncertain. The use of an epitaxial layer on a semi-insulating substrate, however, provides an ideal situation for studying the Rayleigh wave interactions since their penetration depth is so small. Here it is possible to use material with a fairly high carrier concentration (2×10^{15} cm^{-3}) and since the layer thickness is only a small fraction of an acoustic wavelength, there is negligible attenuation produced.

The structure we have used for studying the nonlinear interactions of Rayleigh waves is shown in Figure III-15. The center plate is again a Schottky barrier, but the ohmic contacts in this case run parallel to the plate along the propagation direction. In the transverse dimension we have then essentially a field effect arrangement. We view the surface wave coupling in this situation as originating from the basic nonlinearity of the field effect structure when the active layer under the reverse biased Schottky barrier contact is biased into and out of the pinch-off region. The material used in these experiments was n-type GaAs with carrier concentration 2×10^{15} cm^{-3} and layer thickness of 3-5 μ which is well within the capability of the CMR growth facility.

The convolution property of the epitaxial configuration is shown in Figure III-16. The input signals are at a fundamental carrier frequency

of 176 MHz and a dc bias has been applied between the contacts to maximize the nonlinearity. For various combinations of input pulses the convolution property was found to be satisfied.

The dependence of the convolution output on reverse bias applied to the electrodes is shown in Figure III-17. The maximum output occurs when the active layer is almost completely depleted. There is a correspondence between this point and the point of maximum second harmonic generation when the center plate is used as a simple diode and an external voltage source is applied to it, around the same frequency as the surface waves. In the latter case the second harmonic is monitored by a small resistance in series with the diode.

In Figure III-17 the behavior of the total propagation loss is also shown as a function of bias, and it is possible to separate out the variation in this loss from that of the nonlinear interaction. The loss is found to decrease with reverse bias and become almost constant at large bias. The latter effect is attributed to an increase in transducer efficiency as the epitaxial layer beneath each transducer is depleted of carriers. Similar observations have been reported on bulk material by Takeda et al.[9] We note that over the region where strongest nonlinearity is observed, the propagation loss changes by only a small amount.

From the work outlined above there is clear evidence for the value of GaAs in both bulk and epitaxial acoustic devices. For the linear amplifier configuration we have proposed, it appears likely that realization of a large bandwidth amplifier with relatively low dc power dissipation should be possible. Further investigation of the amplifier is, however, still required to achieve the advantage inherent in using an epitaxial layer structure with mode conversion transducers.

For the nonlinear surface wave interaction devices the merits in making use of the large nonlinearities associated with the free carrier interaction in an epitaxial structure have been clearly established. For both types of surface waves on GaAs structures the observed nonlinear coefficient is approximately 30 db greater than for the more strongly piezoelectric materials, such as $LiNbO_3$, where the nonlinearity arises from large strains. It is felt that practical signal processing devices based on this concept will emerge in the future.

REFERENCES

1. D. R. Evans; M. F. Lewis and E. Patterson, Electronic Letters 7, 557 (1971).
2. L. O. Svaasand, Appl. Phys. Letters 15, 300 (1969).
3. C. E. Quate and R. B. Thompson, Appl. Phys. Letters 16, 494 (1970).
4. W. C. Wang, APL 18, 337 (1971).
5. C. W. Turner, I. M. Mason & J. Chambers, Electronics Letters 7, 696 (1971).
6. C. W. Lee and R. L. Gunther, Appl. Phys. Letters 20, 288 (1972).
7. Hansen, Microwave Report No. 2000, (Dec. 1971).
8. A. M. Goodman, J. Appl. Phys. 34, 331 (1963).
9. S. Takeda et al., Jap. J. Appl. Phys. 11, 24 (1972).

FIGURE CAPTIONS

III-1. A plot of the dc field distribution in a 70μ diode.

III-2. A top view of the GaAs amplifier with rf input on an insulated gate.

III-3. (a) Photos of a completed traveling-wave Gunn Amplifier constructed from material grown at Stanford. (b) A photo of the active region showing the gate spacing, etc.

III-4. Typical I-V characteristic showing flat current saturation and incoherent noise above threshold value. Diode 222-4. Horizontal scale 5 V /division, vertical scale 10 mA/division.

III-5. Probe measurement circuit.

III-6. An experimental plot of the voltage V_G picked up on a probe strip as a function of the voltage V_{ds} across the device.

III-7. An arrangement of staggered probe strips.

III-8. (a) A schematic of a Schottky-barrier GaAs amplifier. (b) The circuit used with the device.

III-9. (a) A top view of the GaAs amplifier with rf input on a Schottky-barrier gate. (b) A photo of the amplifier with rf input on a Schottky-barrier gate (magnified 50X).

III-10. Fabrication sequence of Schottky-barrier amplifier.

III-11. Arrangement for obtaining bulk longitudinal to surface shear wave conversion.

III-12. Acoustoelectric gain for Rayleigh mode vs. drift field for a number of temperatures.

III-13. Schematic diagram for nonlinear interaction due to surface effects shown for the case of a depletion layer.

III-14. Temperature dependence of nonlinear interaction.

III-15. Schematic arrangement for nonlinear interaction of Rayleigh waves on an epitaxial GaAs layer. Interdigital transducer periodicity = 16 μ. N=20 pairs.

III-16. Convolution property shown for pulse inputs at a carrier frequency of 176 MHz.

III-17. Behavior of convolution output and propagation loss as a function of electrode bias.

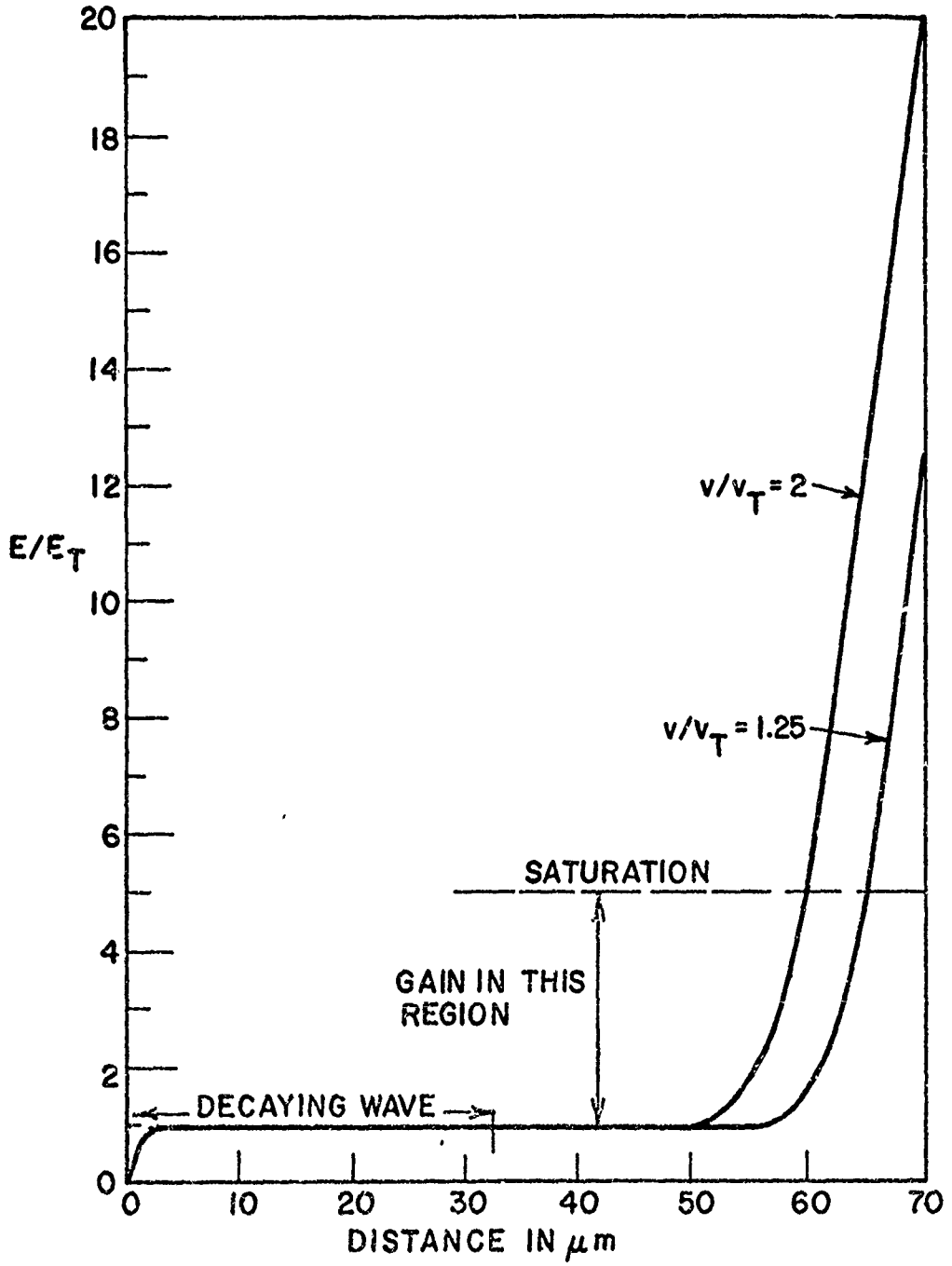

Figure III-1 A plot of the dc field distribution in a 70 μ diode.

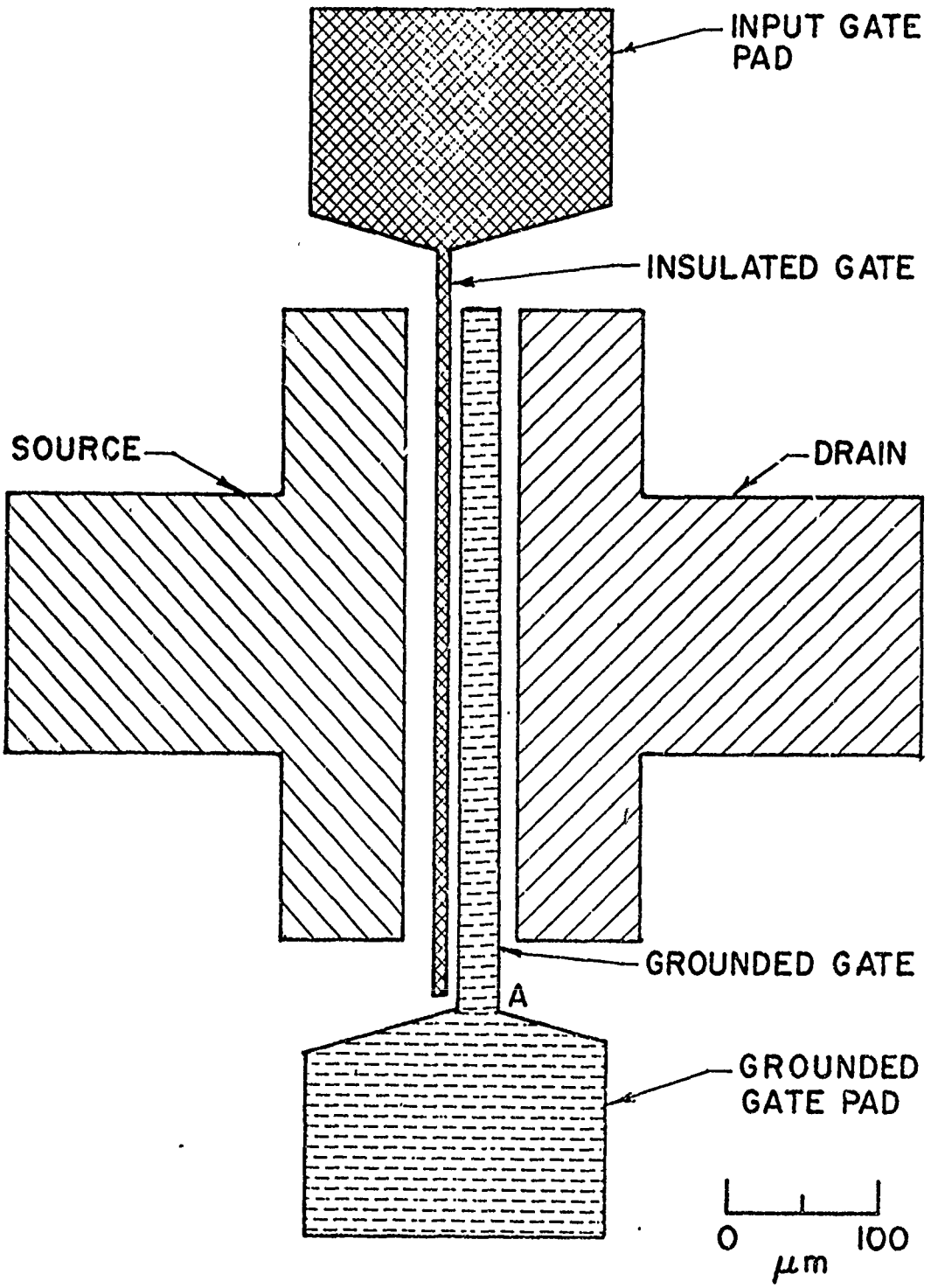

Figure III-2 A top view of the GaAs amplifier with rf input on an insulated gate.

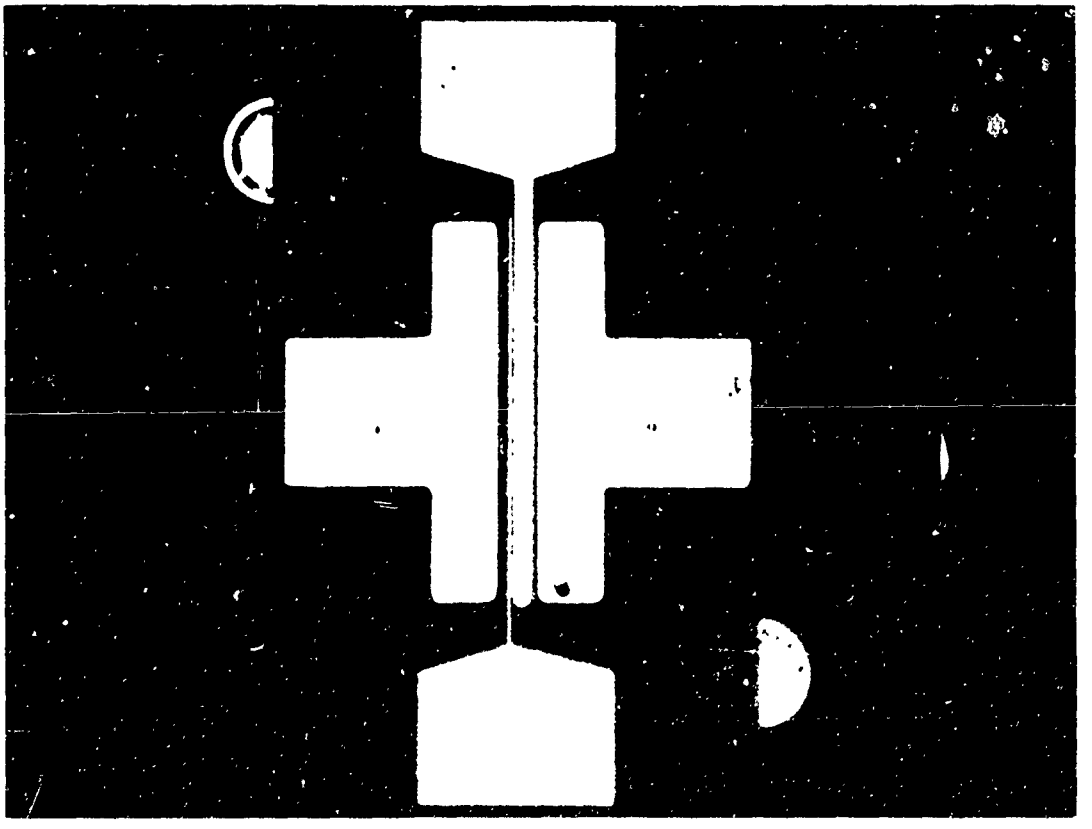

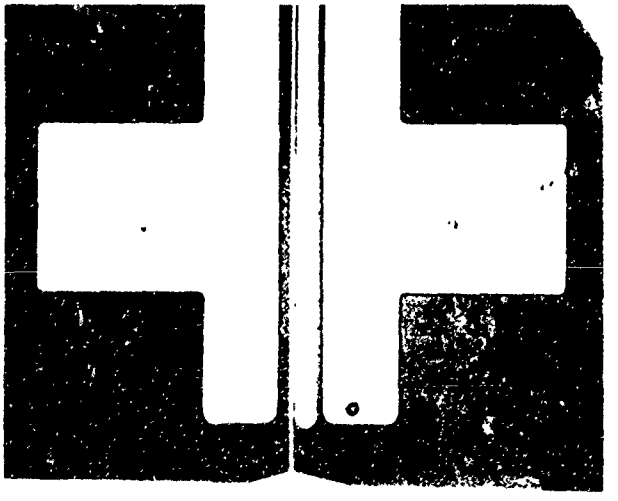

5 μ

70 μ

Figure III-3 (a) Photos of a completed traveling-wave Gunn amplifier constructed from material grown at Stanford. (b) A photo of the active region showing the gate spacing, etc.

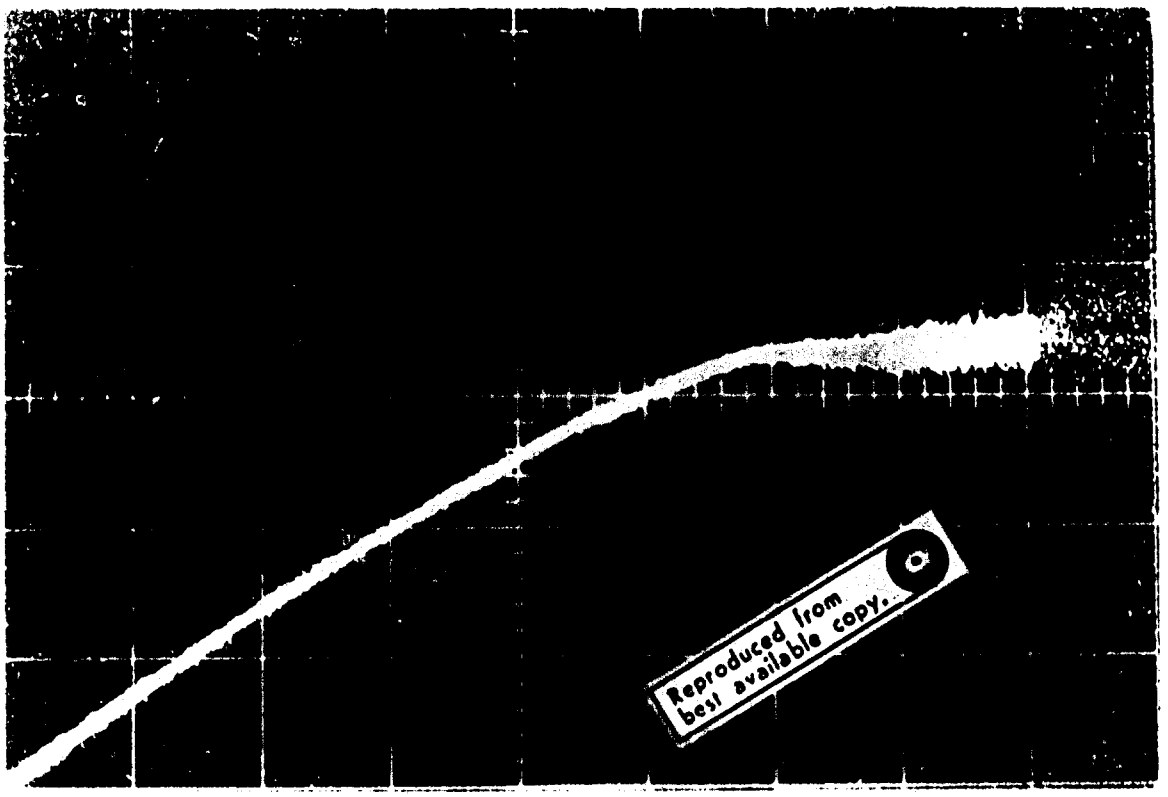

Figure III-4 Typical I-V characteristic showing flat current saturation and incoherent noise above threshold value. Diode 222-4. Horizontal scale 5 V./division, vertical scale 10 mA/division.

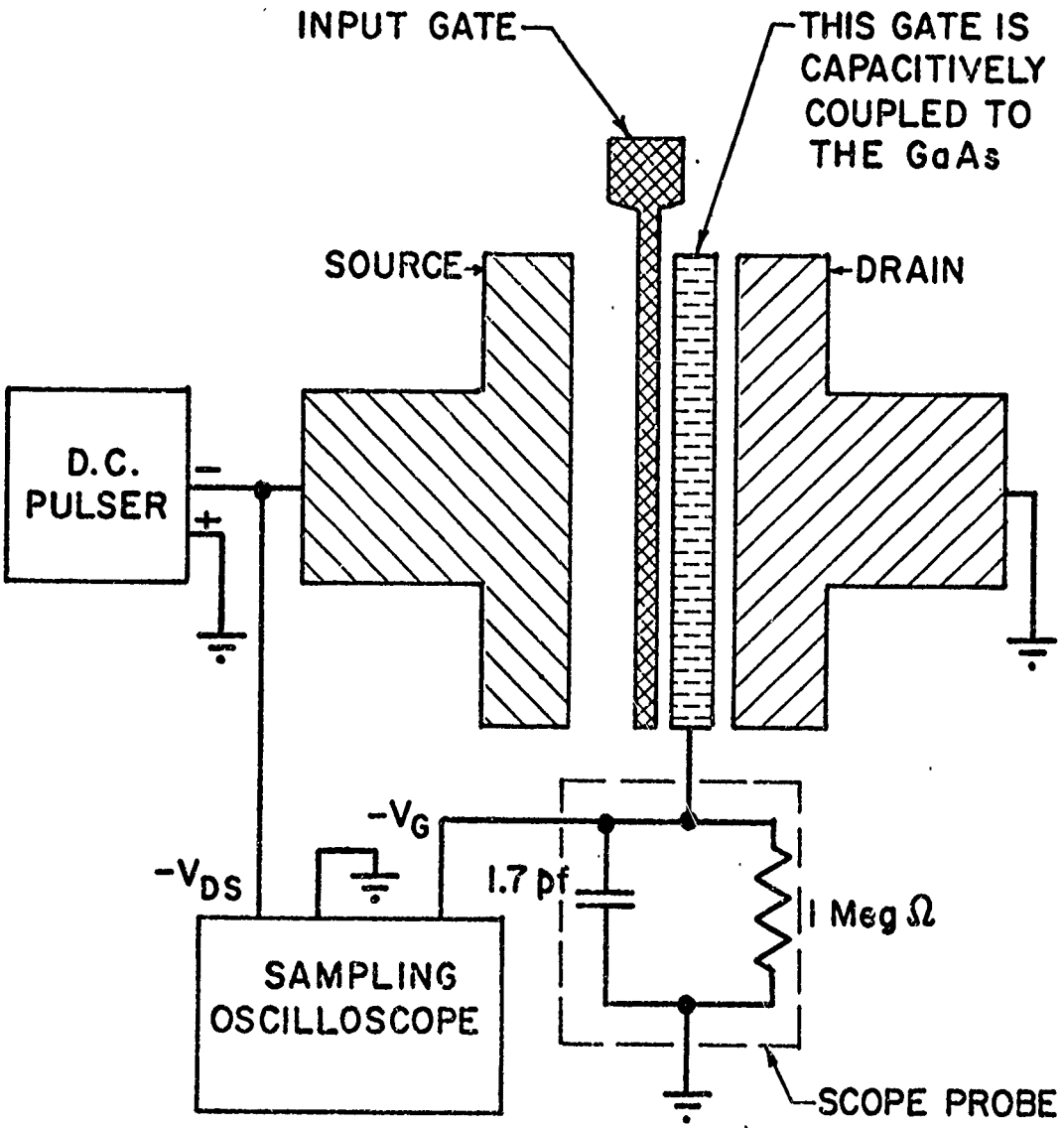

Figure III-5 Probe measurement circuit.

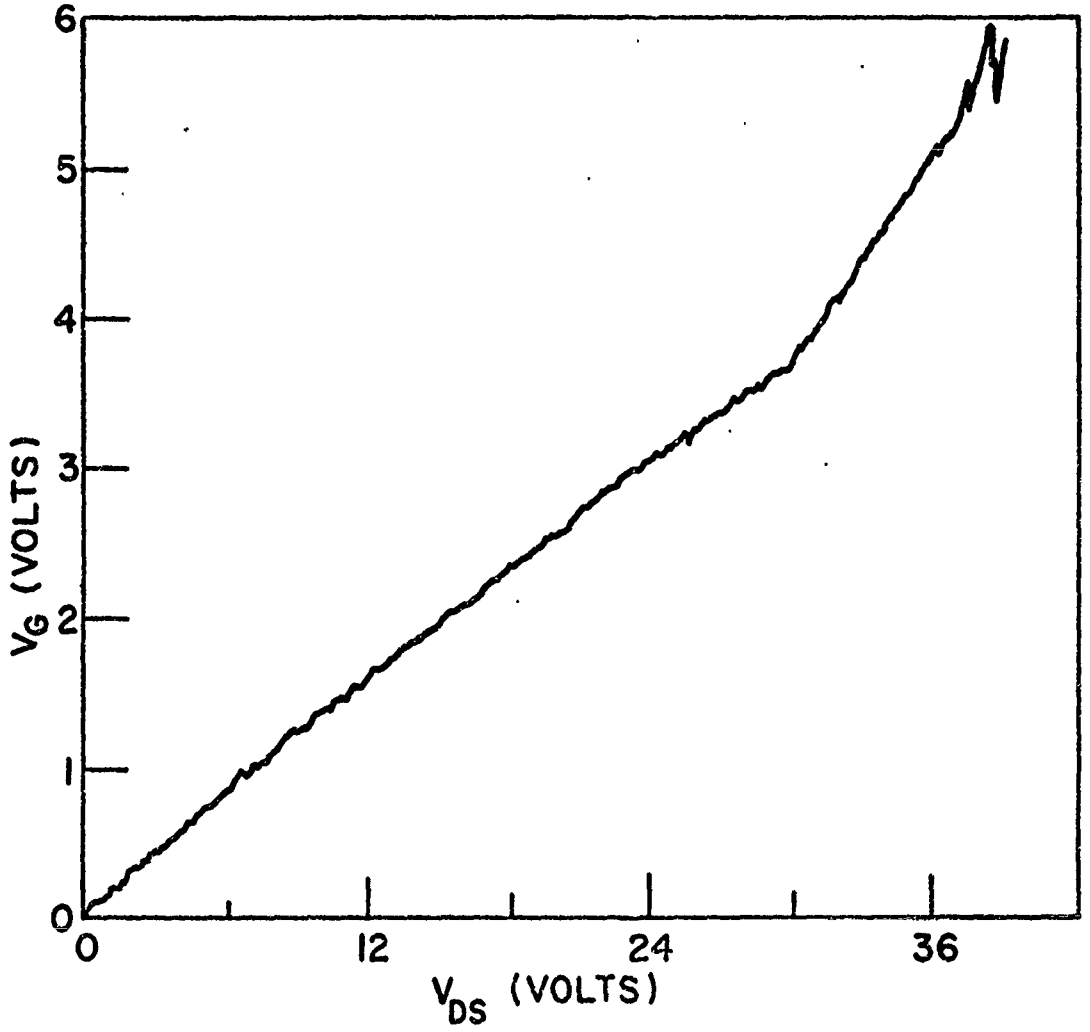

Figure III-6 An experimental plot of the voltage V_G picked up on a probe strip as a function of the voltage V_{DS} across the device.

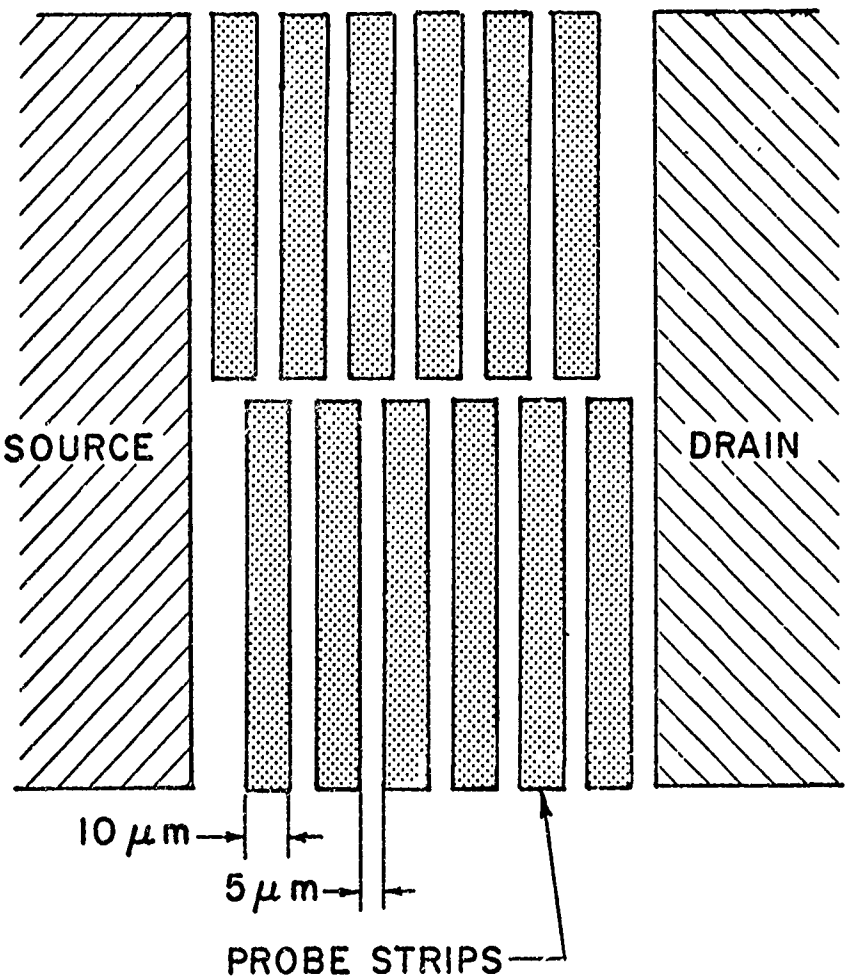

Figure III-7 An arrangement of staggered probe strips.

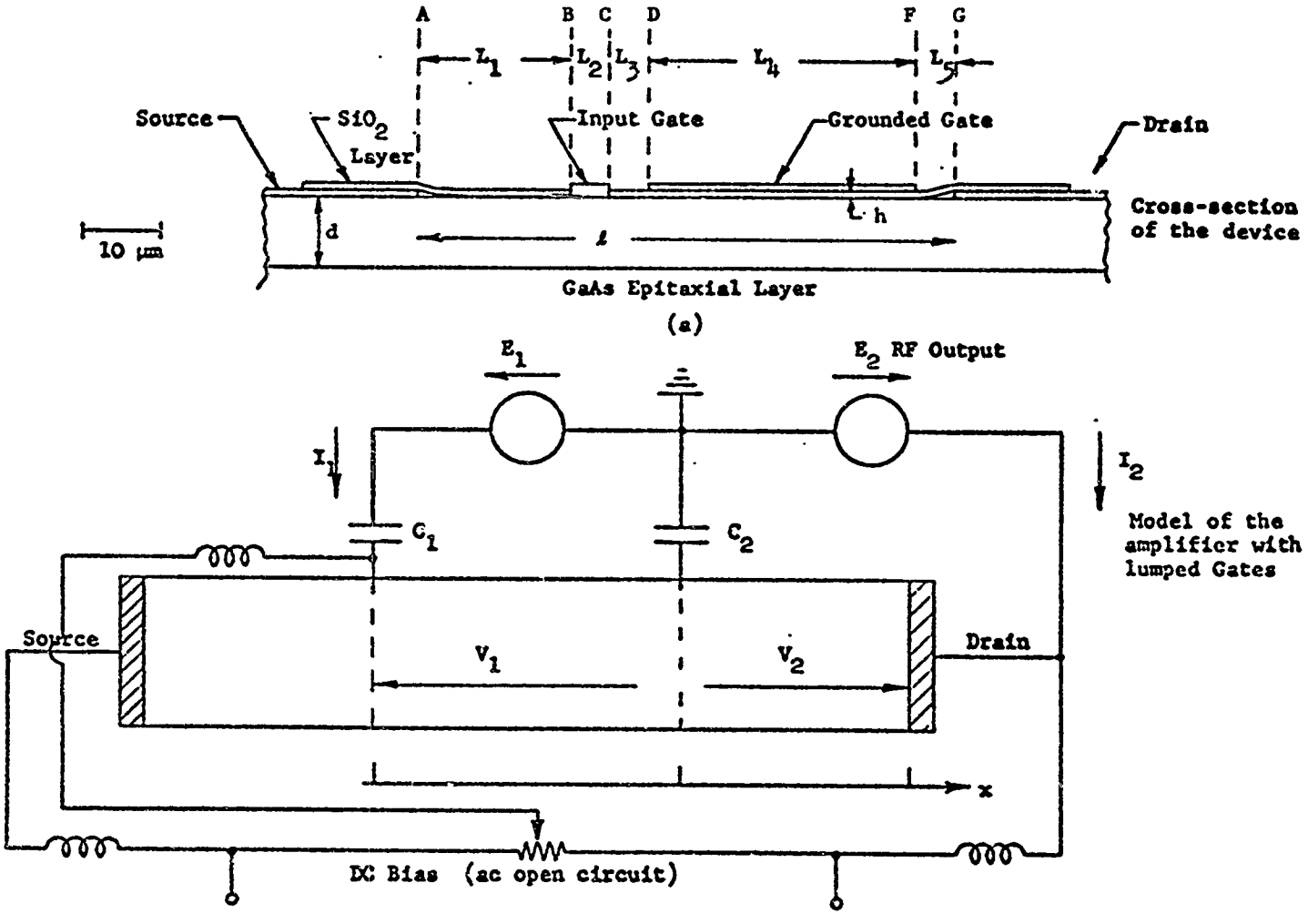

Figure III-8 (a) A schematic of a Schottky-barrier GaAs amplifier. (b) The circuit used with the device.

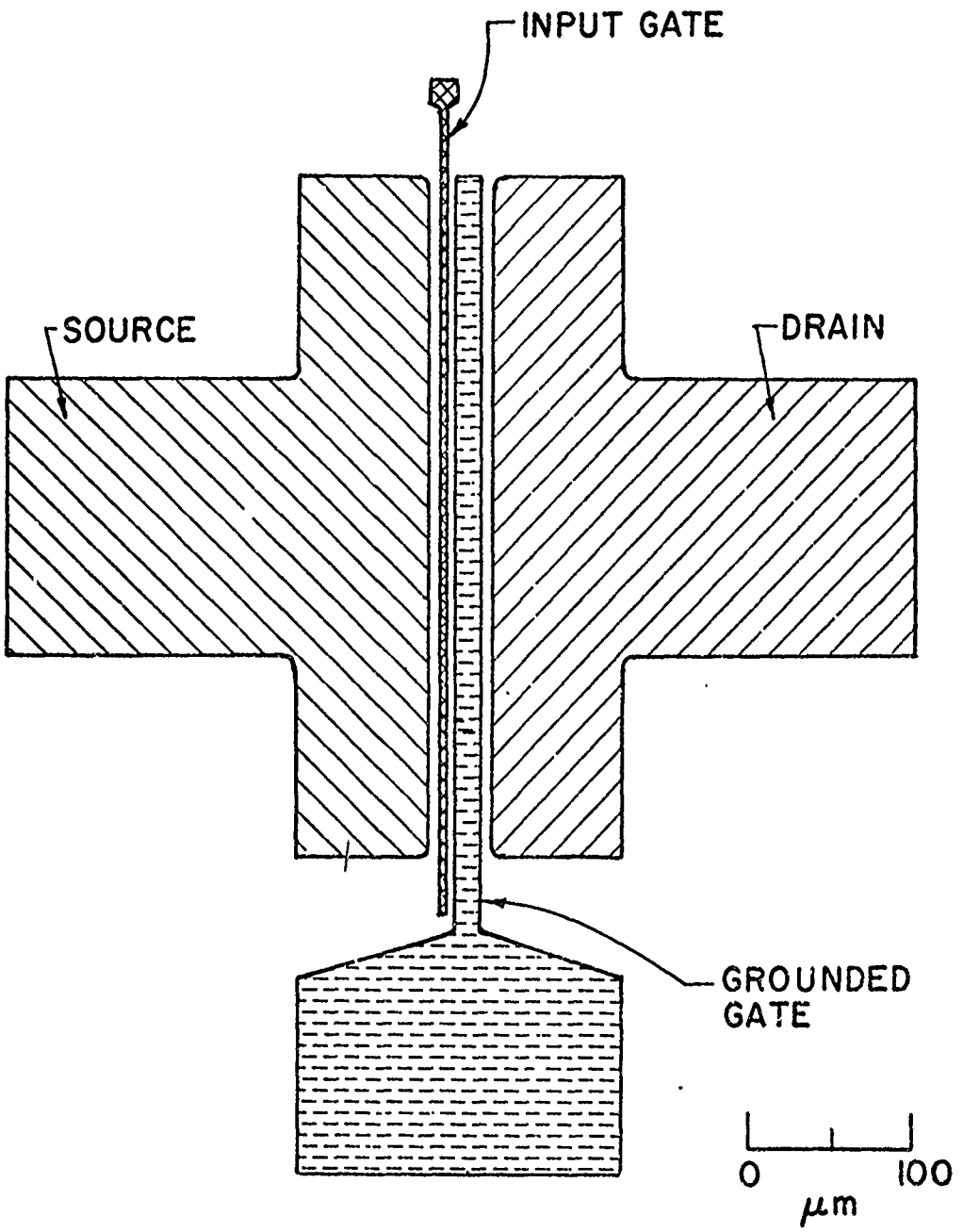

Figure III-9 (a) A top view of the GaAs amplifier with rf input on a Schottky-barrier gate.

30K

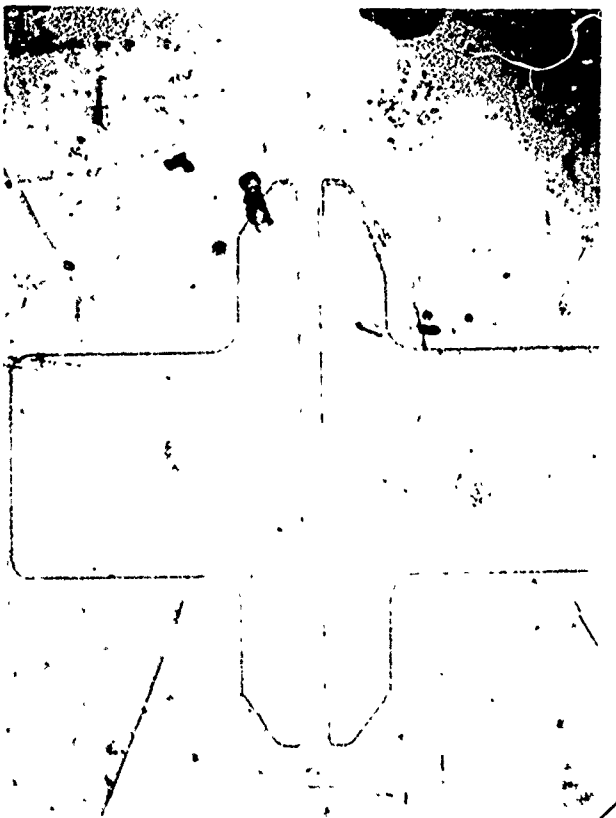

Figure III-9 (b) A photo of the amplifier with rf input on a Schottky-barrier gate (magnified 50 x).

30 x

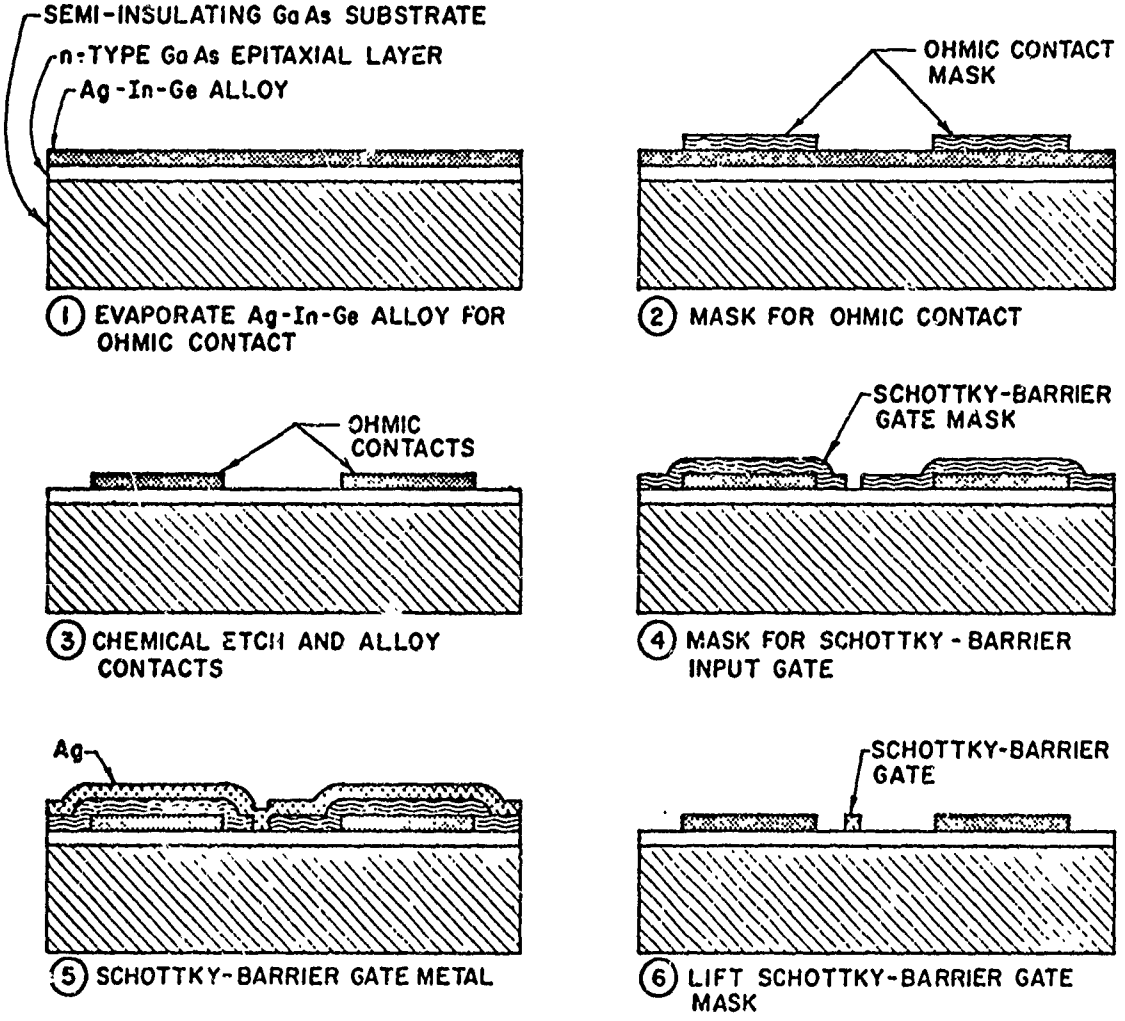

Figure III-10 Fabrication sequence of Schottky-barrier amplifier.

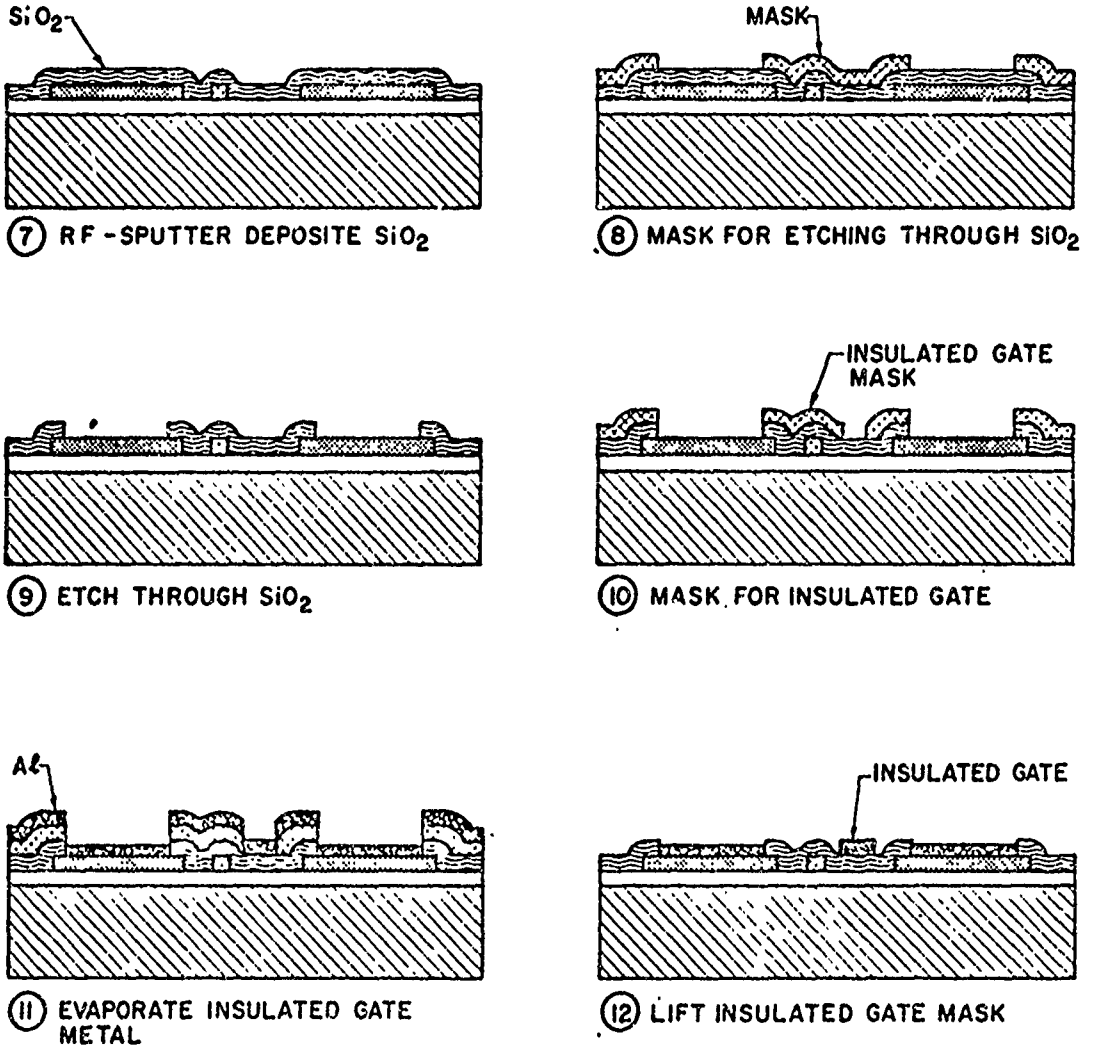

Figure III-10 (Continued)

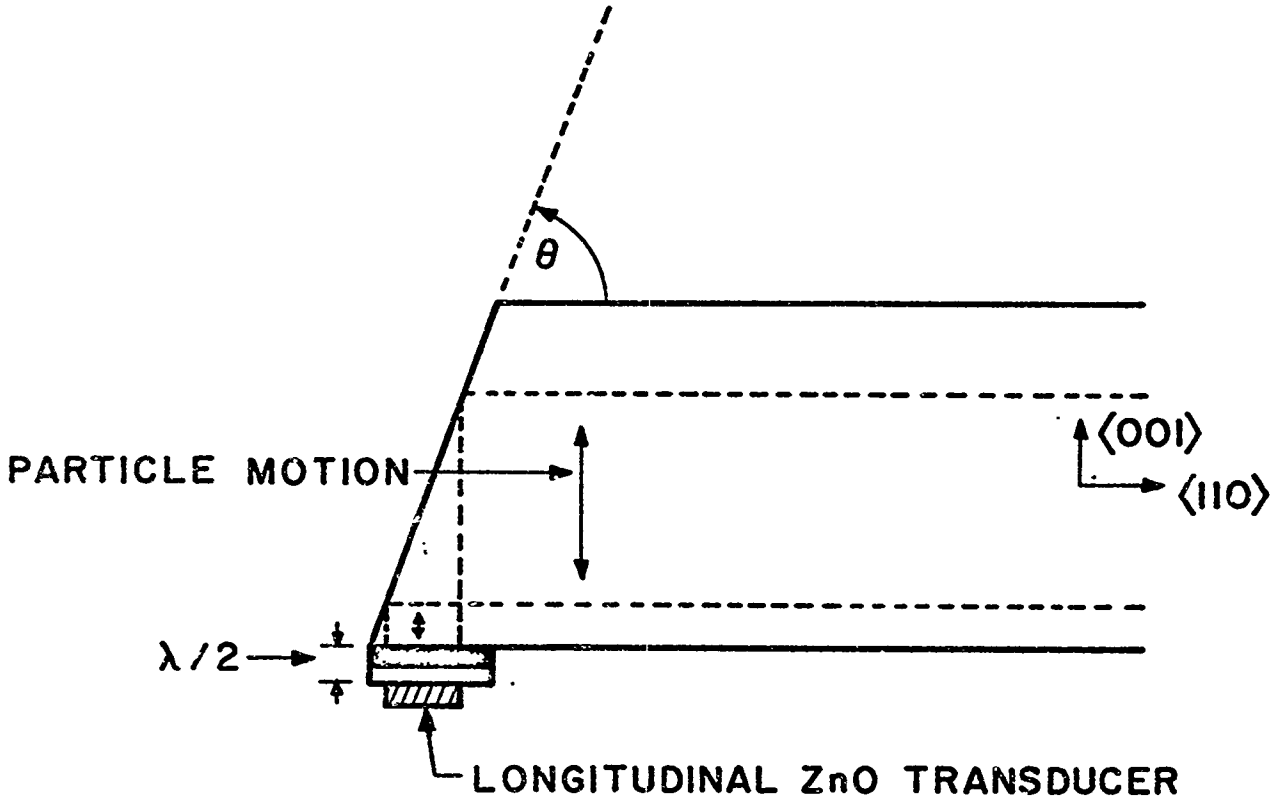

$$\tan\theta = \frac{v_{LONG.}}{v_{SURFACE}} = 54.5 \pm .5°$$

Figure III-11 Arrangement for obtaining bulk longitudinal to surface shear wave conversion.

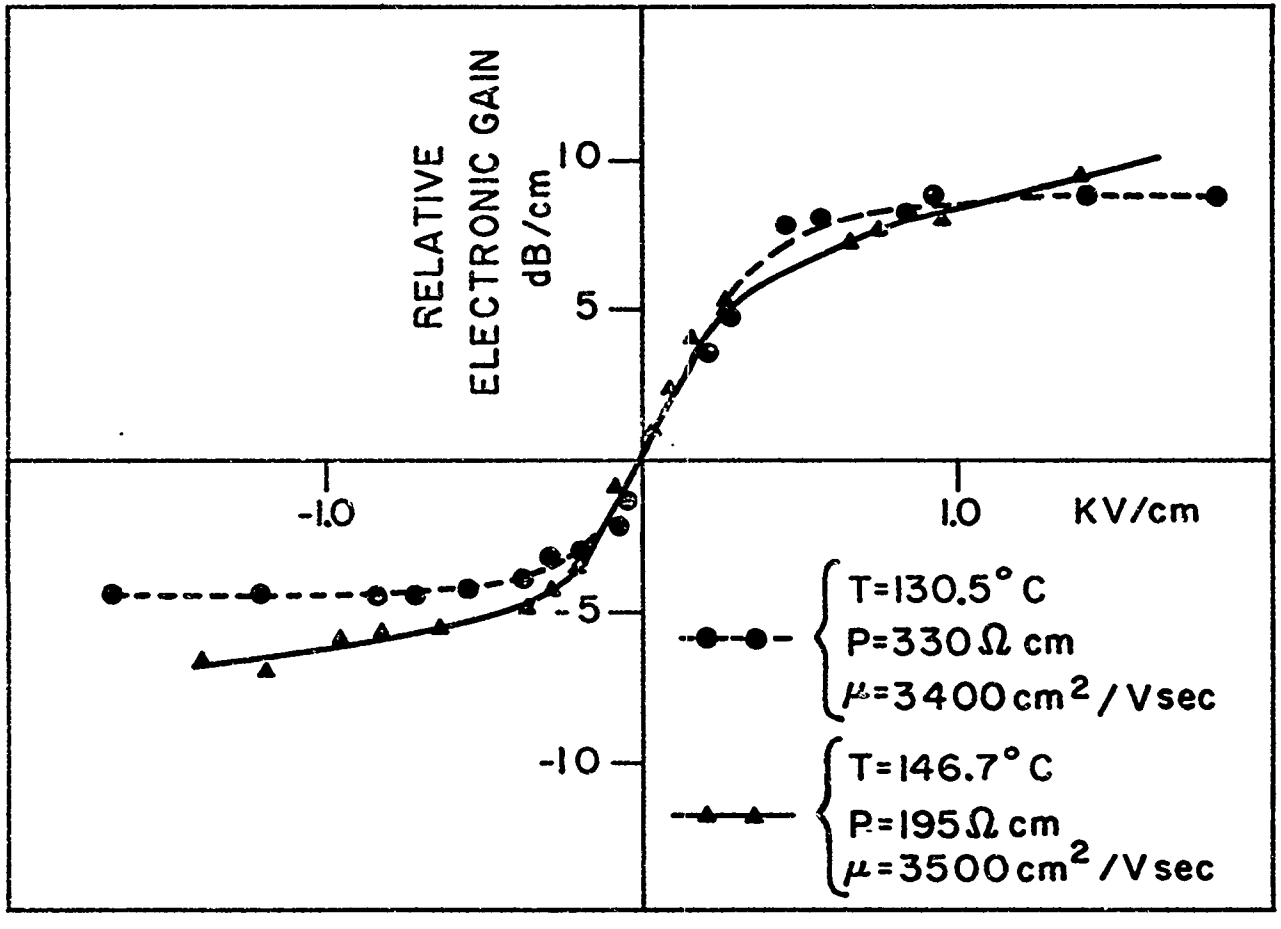

Figure III-12 Acoustoelectric gain for Rayleigh mode vs drift field for a number of temperatures.

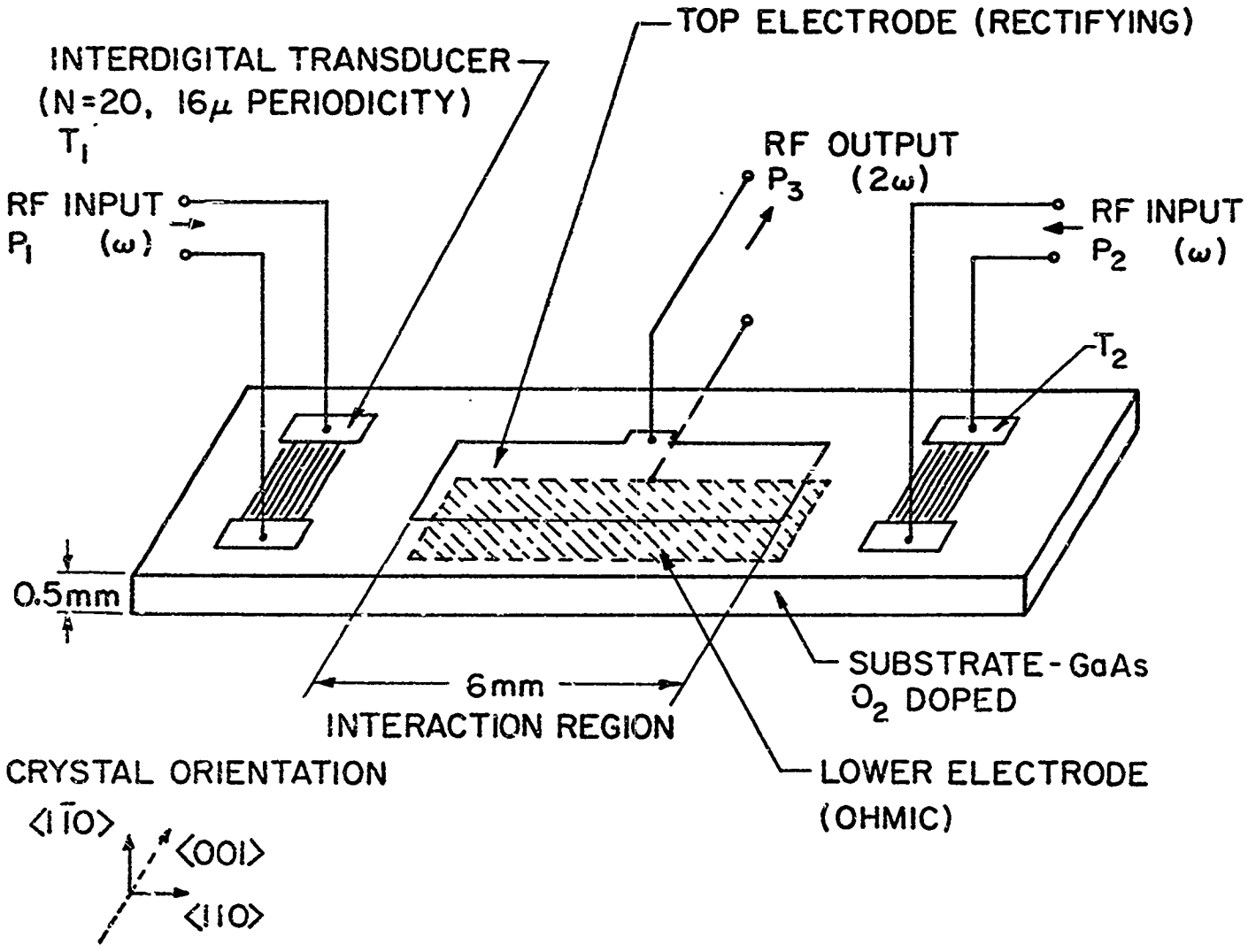

Figure III-13 Schematic diagram for nonlinear interaction due to surface effects shown for the case of a depletion layer.

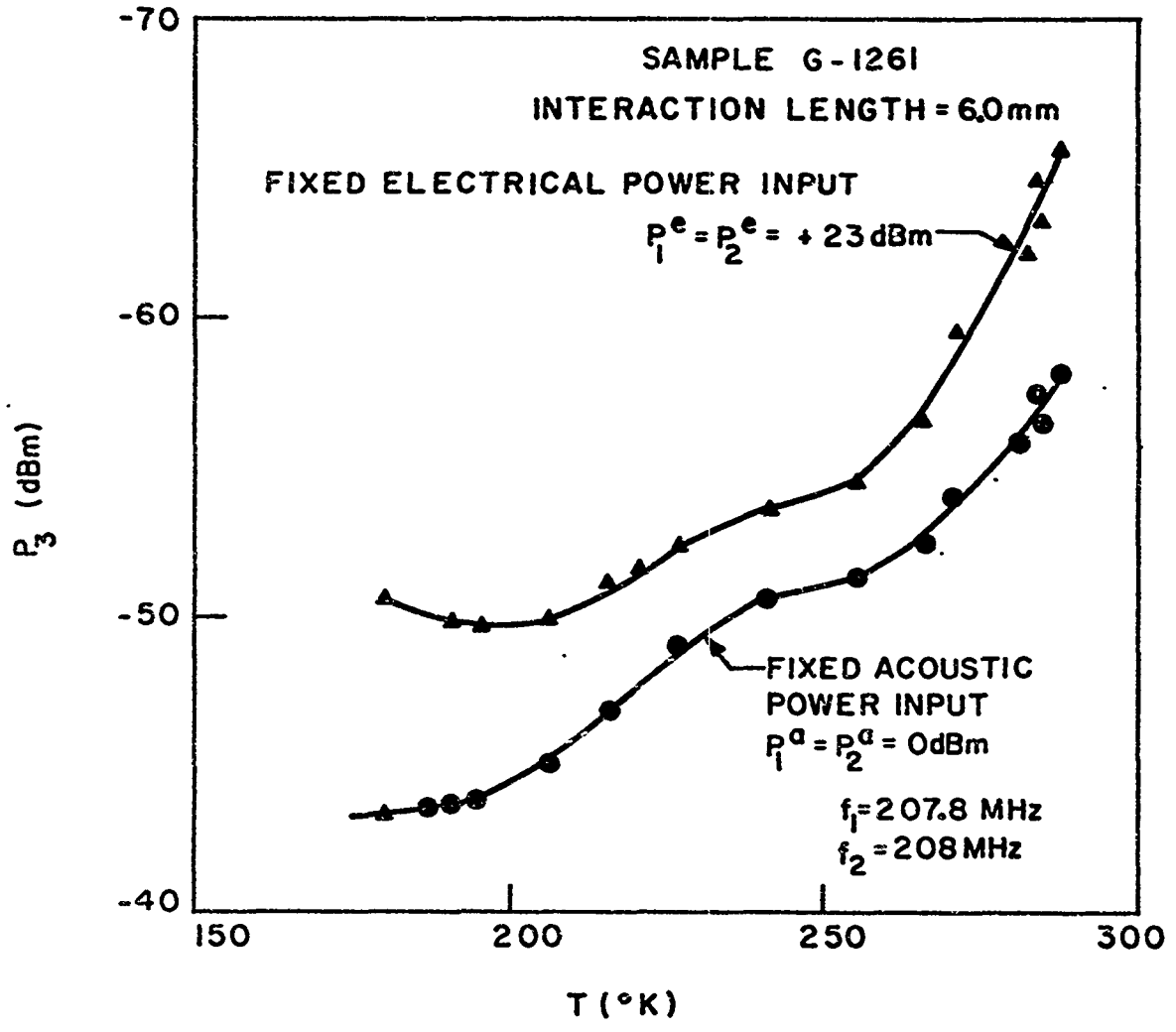

Figure III-14 Temperature dependence of nonlinear interaction.

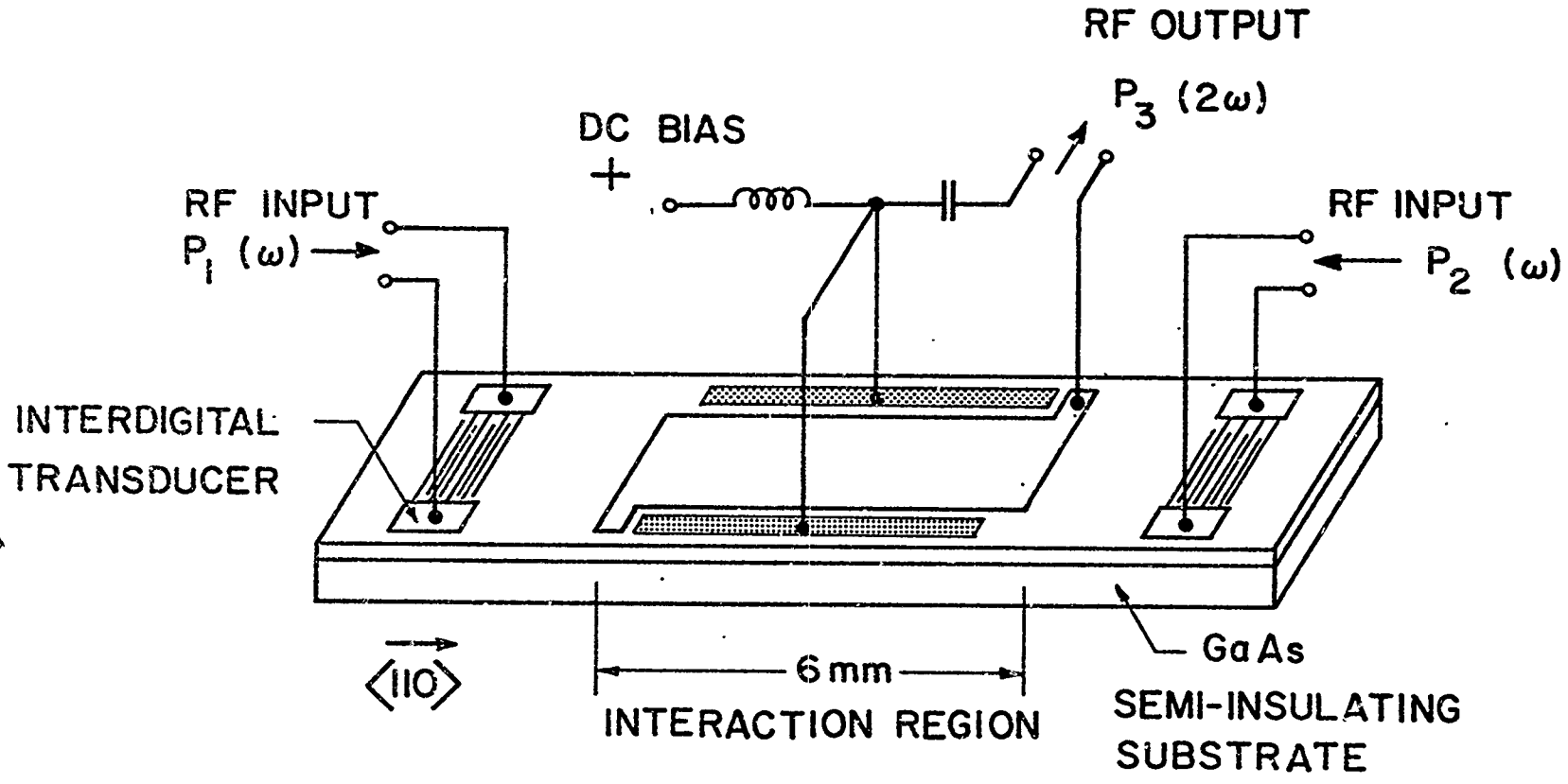

Figure III-15 Schematic arrangement for nonlinear interaction of Rayleigh waves on an epitaxial GaAs layer. Interdigital transducer periodicity = 16 μ. N = 20 pairs.

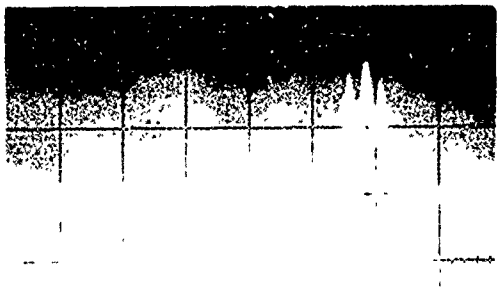

Figure III-16 Convolution property shown for pulse inputs at a carrier frequency of 176 MHz.

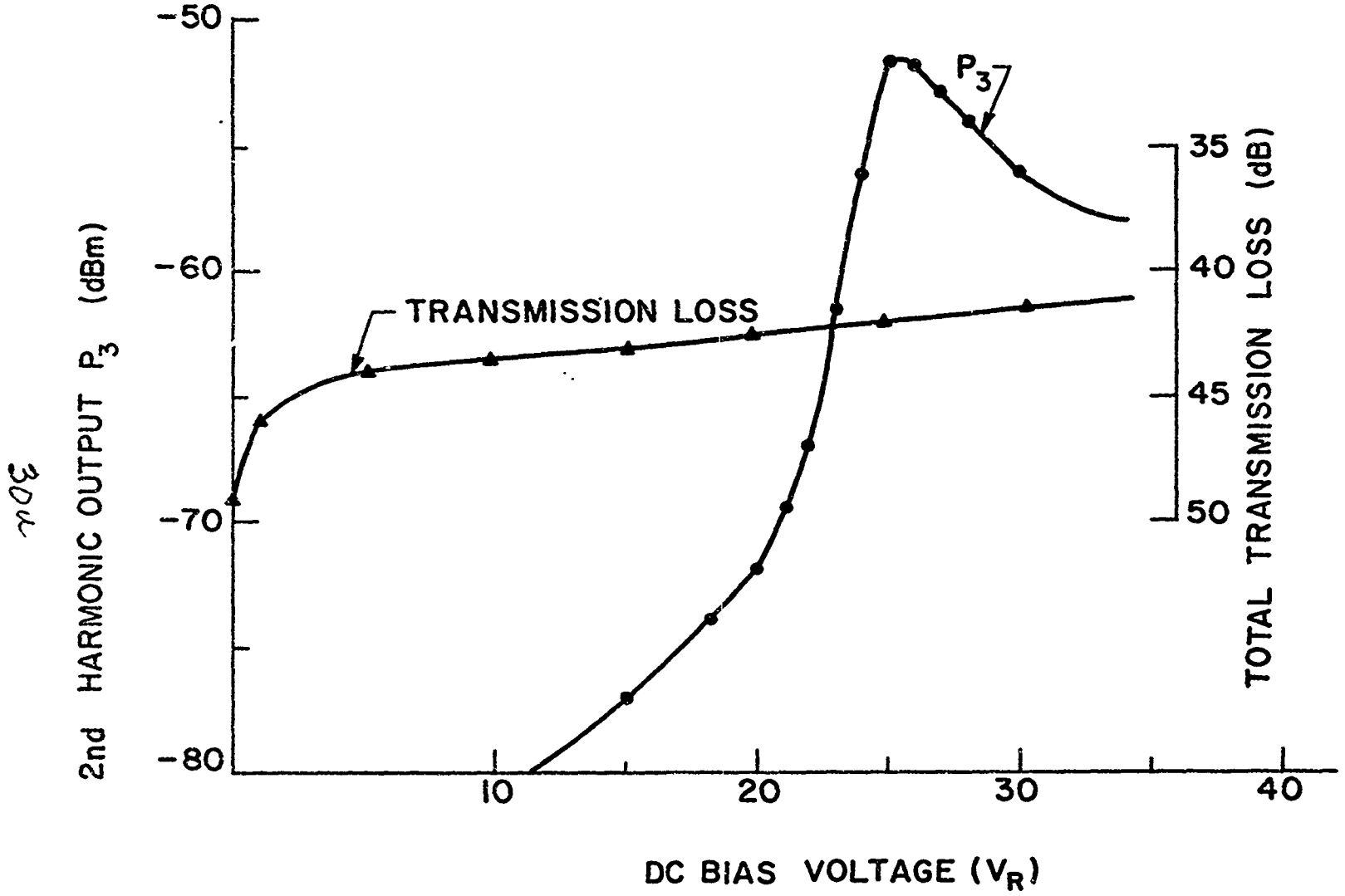

Figure III-17 Behavior of convolution output and propagation loss as a function of electrode bias.

IV. PRECIPITATION STUDIES IN COMPOUND SEMICONDUCTORS

D. A. Stevenson and W. C. Rhines

A. PROGRAM OBJECTIVES

The occurrence of precipitation in compound semiconductors is of practical interest because of the influence on the electrical and optical properties. The precipitation of electrically active foreign atoms may cause a disparity between the bulk concentration of foreign atoms and the concentration of foreign atoms that are in solution. If local distortion of the lattice accompanies precipitation, then changes in dislocation density may accompany the precipitation process. In addition, the mere presence of a dispersed precipitate will modify the electrical transport and optical properties of semiconductors. The question of the extent of precipitation, the nature of the precipitate and the mechanism of precipitation are questions of practical relevance.

Precipitation in zinc vapor-doped GaAs has been the major topic of study to date and was selected because of its relevance to devices and the conflicting reports in the literature on the characteristics and identity of precipitates in this system. The major emphasis in this study has been the use of transmission electron microscopy. The progress in the report period is described below.

B. PROGRESS

During the report period, the major portion of the experimental work on precipitation caused by Zn diffusion in GaAs has been completed and analysis is now in progress. Data have provided the first correlations between actual observation of precipitates and the variables of diffusion time, temperature, source, quench rate, and starting material. Although

no positive identification of the precipitates has been possible, experimental results indicate that it is formed by an isothermal, internal reaction of Zn with an unknown impurity in the GaAs.

1. Effect of Variables

The following general trends were observed concerning the influence of diffusion variables upon the precipitation process: (1) as time at the diffusion temperature increases, the precipitates show a slight size increase and a greater tendency toward faceting, as opposed to the predominant strain fields for short diffusion times; (2) increases in diffusion temperature from 700 through 900°C cause the precipitate size to increase. Precipitates in the high temperature diffusions are faceted while, at lower temperatures, they show distinct strain fields. Precipitate distribution is relatively uniform at high temperatures. At lower temperatures precipitates are isolated in linear patterns, mostly along dislocations; (3) precipitate character shows very little variation as the quantity of pure Zn in the diffusion source varies. The Zn+As diffusion source partially suppresses precipitation and decreases the rate of Zn diffusion; (4) undoped and Te-doped GaAs show identical precipitate distribution and size when diffused with Zn. Zn melt-doped GaAs (5×10^{18} cm^{-3}), when further diffused from a pure Zn source, shows a smaller number and size of precipitates than the undoped or Te-doped starting material; (5) rate of quench has very little effect on precipitates. Very rapidly quenched samples show enhanced strain fields, while slowly cooled samples are highly faceted.

2. Identification Attempts

Reflection electron diffraction was performed in the transmission

electron microscope on a variety of diffused samples. Diffraction from a second phase precipitate could not be detected. Several types of extraction replicas were prepared from cleaved cross-sections of diffused samples. Possible precipitates were observed in some cases, but no diffraction spots could be found. The scanning electron microscope was also used to observe cleaved cross-sections with little success. Differential thermal analysis showed no peaks characteristic of a second phase. Guinier de Wolff X-ray diffraction revealed two reflections from the precipitate phase. The reflections are not characteristic of any known compound or phase formed from Ga, As, and Zn, nor are they prominent reflections of any known Zn compound. Mass spectrographic analysis of Zn-diffused GaAs showed 26 ppm oxygen. Samples of oxygen-doped GaAs ($10^{18}/cm^3$) were, therefore, diffused with Zn and examined in the transmission electron microscope. Only a few very small precipitates were observed.

3. Hot Stage Electron Microscopy

Samples containing precipitates were heated to 786°C in the electron microscope and held for over two hours. Strain fields relaxed but no significant dissolution of the precipitates in the GaAs matrix occurred. This confirms the isothermal formation of precipitates at the diffusion temperature and strongly suggests an internal reaction of Zn with an unknown impurity.

Hot stage electron microscopy of GaAs is limited by the vaporization of As from the sample surface which destroys the polished surface and makes examination impossible after several hours at 800°C. Diffusion of Zn into GaAs was attempted in the microscope by preparing thin samples of GaAs with rf sputtered layers of Zn followed by SiO_2 on both surfaces.

Lattice deformation of the GaAs caused spalling of the SiO_2 and prevented transmission examination after a few hours at 800°C.

4. Deformation of Zn Melt-Doped GaAs

Heavily Zn melt-doped samples of GaAs were deformed at 800°C to see if precipitation would occur. Extensive dislocation tangles were seen by transmission electron microscopy but no evidence of precipitation appeared.

5. Ion Implantation

A proton-assisted diffusion of Zn into GaAs was conducted to see if appreciable Zn penetration and concentrations could be achieved by diffusion at lower temperatures. Samples with 100 Å thick, rf sputtered layers of Zn on the surface were heated to 500°C while bombarding with 2×10^{15} H_2^+/cm^2. No evidence of precipitation or dislocation damage was seen in the samples.

C. FUTURE PLANS

In addition to analysis of the data on Zn-doped GaAs, the following studies are planned:

(1) Electron microscopy of vapor and liquid phase epitaxial layers of GaAs and $GaAs_xP_{1-x}$ before and after diffusion.

(2) Electron microscopy of doped GaN epitaxial layers, thinned by ion bombardment.

(3) Electron microscopy of epitaxial $Ga_xAl_{1-x}As$ to detect chemical inhomogeneities.

(4) Proton-assisted diffusions of Zn into GaAs at a variety of temperatures, followed by electron microscopy.

(5) Further ternary diffusion path determinations in the Ga-As-Zn system.

(6) Electron microscopy of Zn-diffused GaP to study precipitation.

V. RELATIONS BETWEEN DISLOCATIONS AND MECHANICAL PROPERTIES AND THE PRODUCTION AND CHARACTERIZATION OF DEFECT STRUCTURES IN COMPOUND SEMICONDUCTORS

R. H. Bube, W. D. Nix, B. Liebert and A. L. Lin

A. PROGRAM OBJECTIVE

In this part of the research program we are attempting to devise techniques for modifying and characterizing the line defect structures in compound semiconductors, particularly GaAs, through high temperature mechanical deformation. The objectives of this work are to discover and understand the effects of various types of dislocations and dislocation arrays on the important electrical and opto-electronic properties of GaAs and to suggest ways of utilizing dislocations in devices. Our present work on GaAs is motivated by the extensive microwave device research on this material at Stanford. It is expected that our work will contribute to the device research and to the related crystal growing effort by providing basic information about the effect of dislocations in these crystals.

B. PROGRESS: Pure GaAs

In the previous progress report it was mentioned that the effects of dislocations on the carrier concentration should not be manifested until ρ/b, the dislocation density divided by the Burgers vector, was approximately equal to or greater than the carrier concentration. Since there exists a physical limitation on the density of dislocations that may be introduced, the only parameter than can be varied is the carrier concentration. For our experimental conditions it is necessary to have a carrier concentration of 10^{14} cm^{-3} or below to observe the intrinsic effects of dislocations. However, we are not able to obtain bulk GaAs

crystals of this purity. It would be possible for us to carry out the bending experiment on epi-layered crystals so long as the substrate is insulating and the epi-layer has a sufficiently low carrier concentration. We have attempted to obtain such material commercially, without success and some effort has been made by the Crystal Growing Group to prepare the epi-layers for our experiment, but as yet we have no results to report.

Because we have not yet obtained GaAs with a sufficiently low carrier concentration, we have been faced with two alternatives. We could drop gallium arsenide from consideration and begin a study of a different material, one in which a sufficiently low carrier concentration is readily available., e.g., silicon. However, since we have seen changes of carrier concentration in our samples after bending, it may be worthwhile to continue this study of GaAs in an attempt to understand the mechanisms responsible for these large effects. During the report period we have selected the latter alternative.

In order to determine the possible scattering mechanisms before and after bending, Hall measurements yielding a straight line when mobility is plotted vs. 1/T are desirable. An inspection of the mobility curves in our previous report indicates that low temperature ($4^{o}K$ to $77^{o}K$) measurements are therefore necessary. An existing helium system was modified for the purpose of making Hall measurements and an initial run (from $77^{o}K$ to $300^{o}K$) was made to check on our ability to reproduce our previous measurements with this system. A large discrepancy in both carrier concentration and mobility was observed (Figures V-1 and V-2). This may have been due to aging of the sample, poor contacts, or improper

functioning of the sample holder and helium dewar. Since no problems have been encountered with samples or contacts in the past, it is reasonable to conclude that this large discrepancy must lie with the equipment. Our present plan is to purchase a new helium system for our laboratory so that these low temperature measurements can be made. When this equipment becomes available, this phase of our study of the effects of plastic deformation on the electrical properties of GaAs will be terminated.

C. PROGRESS: HIGH RESISTIVITY GaAs:Cr

1. Analysis of Photo-Hall Data

Results are presented on three samples of GaAs from the same ingot and with the same initial dark conductivity: (1) an as-grown sample, (2) a sample heat-treated at 580°C for 1 hour, and (3) a sample subjected to deformation during 50 min. at 580°C after a 10 min. pre-heating, to produce excess Ga-dislocations by so-called α-bending. Initial results were reported in the Semi-Annual Report for the period 7/1-12/31/71. Measurements have been refined and completed, and some analysis of the results carried out.

Photoconductivity response spectra at 80°K in the extrinsic range are given in Figure V-3, and quantitative data for the intrinsic range are summarized in Table V-I. Measurements linking the extrinsic and intrinsic ranges between 1.2 and 1.5 eV were exceedingly difficult to make. Time constants exceeding 10 hours in magnitude characterized the attempt to establish a steady-state in this range after photoexcitation in the range from 1.0 to 1.2 eV. It is likely that at least some of the difficulty can be attributed to electrode effects, as summarized in a later

section.

The photo-Hall mobility as a function of photon energy for these three samples is given in Figure V-4. Heating introduces new structure in the range 0.85-1.0 eV, which is retained in the deformed sample. Deformation lowers the mobility in the intrinsic range.

On the assumption that most of the phenomena observed in Figure V-4 for the Hall mobility is due to two-carrier effects, the conductivity data of Figure V-3 and the mobility data of Figure V-4 were combined to permit the calculation of hole and electron densities. To achieve numerical values, it is necessary to assume values for the one-carrier mobilities. Guided by the measured values of mobility in Figure V-4, we chose a mobility ratio of 10, and electron mobilities of 3400 (as-grown), 7500 (heated), and 5000 (deformed) $cm^2/V\text{-}sec$, respectively. Absolute values depend on the actual choice, of course, but relative variations are not very sensitive. Results of such an analysis for p and n are given in Figure V-5 for the extrinsic range; intrinsic results are included in Table V-I. Since the measured mobilities are much less than the assumed electron mobility over most of the spectral range, the analysis predicts a value of p in excess of that of n. It is not likely for this actually to be the case in view of the optical quenching phenomena observed, and probably results from variations of effective carrier mobilities with exciting photon energy and from inhomogeneities in the crystals; other choices of μ_n and μ_p will be made in the future to arrive at a resolution of this question. Such changes in analysis are not likely to alter the basic variations with photon energy shown in Figure V-5, or the strong decrease in n in the heated crystals in the quenching range of 1.0 to 1.5 eV.

An initial attempt to begin the description of the detailed photo-Hall mobility vs. photon energy data of Figure V-4, in terms of the two-level model generally established for GaAs:Cr, is given in Table V-II. The numerical data given are for 80°K and the energy values have an uncertainty of ± 0.02 eV. Within this framework the observed dependence of μ_H on photon energy between 0.65 and 0.90 eV can be reasonably correlated. For higher photon energies than those included in Table V-II, the as-grown crystal appears to behave differently from the heated and bent crystals. Both of the latter indicate an increase in electron excitation when $\hbar\omega$ exceeds 0.90 eV, followed by an increase in hole excitation when $\hbar\omega$ exceeds 0.95 eV. Levels lying 0.1 eV below level A and 0.1 eV above level B would formally satisfy this requirement. Allen (Brit. J. Appl. Phys. 1, 593 (1968)) proposes a possible band of energies for Cr in GaAs with a width of about 0.1 eV. We shall continue to explore the best way to interpret the photo-Hall data.

2. Optical Quenching of Photoconductivity

Measurements of the optical quenching of photoconductivity at 80°K were completed and are compared for the three samples in Figure V-6. The quenching spectrum consists of a broad structure with minimum energy of 0.90 eV (corresponding to $\hbar\omega > 0.85$ eV in the model of Table V-II), and a small auxiliary quenching band with maximum at 0.8 eV (corresponding to 0.7 eV $< \hbar\omega <$ 0.8 eV in the model of Table V-II).

3. Thermally Stimulated Conductivity

The thermally stimulated conductivity of these three samples after photoexcitation at 80°K by monochromatic intrinsic or extrinsic radiation is summarized in Figure V-7. Striking structure is found in these

TSC curves, which is sensitive in absolute and relative magnitudes to the processes of heating and deformation. Of perhaps even greater interest is the correlation between the structure reported here for high-resistivity GaAs:Cr and other reports of high-resolution fine structure in TSC data on other forms of high-resistivity GaAs. Table V-III compares our data with that of Haisty, measured on undoped high-resistivity GaAs, and that of Blanc et al., measured on Cu-diffused high-resistivity GaAs:Cu. The agreement between the peaks found by us and those reported by Haisty is very close, indicating a real materials property, but probably not one related to Cr impurity. Estimate of the trap depths indicates that they probably all lie between 0.19 and 0.42 eV.

Haisty reported strange properties of the TSC peaks in his material, dependent on time and intensity of photoexcitation. His work was done with "white" light. Although our data seem well-behaved for monochromatic excitation, we also find marked differences if "white" light is used. Figure V-8 shows the TSC curves obtained after three different intensities of white-light excitation on our deformed sample (compare Figure V-7). For the highest intensity, three peaks are found, at 117^{o} and 130^{o}K (corresponding roughly to the two lowest-temperature peaks in Figure V-7) and a large peak at 284^{o}K (0.57 eV). A similar deep trap TSC peak is reported by Haisty for high-intensity long-time white-light photoexcitation. It is likely that at least some of the strange effects of white-light excitation are due to the simultaneous excitation and quenching effects. Long-time photoexcitation by monochromatic radiation, which both excites and quenches, was observed for our deformed sample to decrease the low-temperature TSC peaks and increase the higher-temperature TSC peaks. The dramatic effect of irradiating the sample with

1.08 eV quenching radiation after 0.85 eV exciting radiation is shown by Curve 4 in Figure V-8; all structure disappears.

4. Deformation to Produce Excess As-Dislocations: β-Bending

Attempts were made to produce β-bending of the GaAs:Cr crystals, in order to compare the effects with those reported above for α-bending. Successful α-bending had been accomplished, as mentioned above, with a total heating time of 1 hour at 580°C with a load of 1.2 kg in the 4-point bending apparatus.

Four attempts to produce β-bending all ended in a fractured sample. Fracture occurred in all cases for a deformation of the crystal considerably less than that produced by α-bending. The four samples fractured in different locations along the bar and into a different number of pieces. In each case the fracture occurs (at least macroscopically) along a $\{110\}$ plane. This observation is consistent with other studies of III-V compounds (M. S. Abrahams and L. Ekstrom, Acta Metall. 8, 654 (1960)). Optical examination of the fracture surfaces revealed "river patterns" which are indicative of cleavage fracture. A preliminary study of the river patterns indicates that the cleavage cracks are nucleated on the tension side of the bent sample, as one would expect. However, this observation will be checked with a more careful study with the electron microscope.

The observation that the samples are more brittle when deformed by β-bending is interesting not only from a mechanical viewpoint, but from the electronic point of view as well. It is not at all clear why β-dislocations should be more effective than α-dislocations in producing fractures. The fact that they are (or seem to be) may be indicative of some

important structural or electronic differences between the α and β dislocations. Some insight into this problem can be gained by considering the work of Abrahams and Ekstrom on cleavage nucleation in covalent materials. They pointed out that cleavage cracks in elemental semiconductors occur on $\{111\}$ planes, in contrast to the $\{110\}$ cleavage for III-V compounds. They suggested that this difference arises because of differences in the core structure of Lomer-Cottrell dislocations in these materials. Briefly, in all solids with the FCC lattice, pairs of glide dislocations of the type $\left[\frac{a}{2}\langle 110\rangle \{111\}\right]$ can react to form Lomer-Cottrell sessile dislocations. These dislocations are edge dislocations of the type $\left[\frac{a}{2}\langle 110\rangle \{100\}\right]$. Abrahams and Ekstrom showed that all of the atoms in the core of a Lomer-Cottrell dislocation in a group IV solid can form covalent bonds (although distorted) with their nearest neighbors. In contrast, the core structure of the Lomer-Cottrell dislocation in III-V compounds is such that covalent bonding cannot be satisfied. They suggested that cleavage in III-V compounds occurs on the $\{110\}$ planes because it is nucleated on those planes by the stress fields of the Lomer-Cottrell dislocations. It may be possible to extend this theory to explain the observation that the high resistivity GaAs crystals are more brittle in β-bending than in α-bending. This extension should take account of the possible effects of charge on the core structure of the Lomer-Cottrell dislocations as well as the effects of electric charge on the intensity of the stress at the point of cleavage (charges on dislocations will affect the dislocation distribution in pile-ups). Also, some consideration should be given to the fact that the brittleness observed for β-bending of high resistivity GaAs was not observed for conducting GaAs.

5. Electrode Effects

As shown clearly in Figures V-3 to V-5, low-temperature photoconductivity measurements on GaAs:Cr involve two-carrier effects. We have found that the magnitude of the measured probe voltage (i.e., the voltage drop along the crystal measured with a high-impedance voltage detector from two probes along the length of the crystal) is a very good indicator of the sign of the dominant carriers for a particular kind of electrode material. For indium contacts, as used in the results reported here, the probe voltage is large and normal in the intrinsic range and for photon energies less than 1.0 eV, but drops to much smaller values in the intermediate range where p-type photoconductivity is found. For zinc contacts, the probe voltage is large and normal in the intermediate range of p-type photoconductivity, but drops to much smaller values in the intrinsic and low energy ranges. Further investigation of electrode effects will be reported later.

D. FUTURE WORK: HIGH RESISTIVITY GaAs:Cr

(1) Continued development of a suitable model and interpretation of the data in terms of that model.

(2) Exploration of electrode effects and correlation with data interpretation.

(3) Investigation of the effects of heating at different temperatures and for different lengths of time.

(4) Attempts to produce β-bending without fracture.

(5) Anneal samples after deformation to see effects on photoelectronic properties measured subsequently.

(6) Start with GaAs:Cr material with lower initial dislocation density and carry out investigation of heating and deformation effects.

TABLE V-I

Photoconductivity for Intrinsic Excitation at 80°K

	1.49 eV photons*					1.7 eV photons				
	σ, $(ohm\text{-}cm)^{-1}$	μ, $cm^2/V\text{-}sec$	p, cm^{-3}	n, cm^{-3}	p/n	σ, $(ohm\text{-}cm)^{-1}$	μ, $cm^2/V\text{-}sec$	p, cm^{-3}	n, cm^{-3}	p/n
As-grown	1.8×10^{-6}	1900	1.5×10^{10}	1.5×10^{9}	10	7.2×10^{-8}	2900	1.2×10^{8}	7×10^{7}	1.7
Heated	1.5×10^{-7}	1600	10^{9}	2×10^{7}	50	2.3×10^{-8}	3100	10^{8}	9×10^{6}	11
Bent	1.1×10^{-7}	800	10^{9}	3×10^{7}	33	3.8×10^{-9}	550	4×10^{7}	9×10^{5}	44

*Photon energy for maximum photoconductivity.

TABLE V-II

Optical Transitions in Extrinsic Photoconductivity

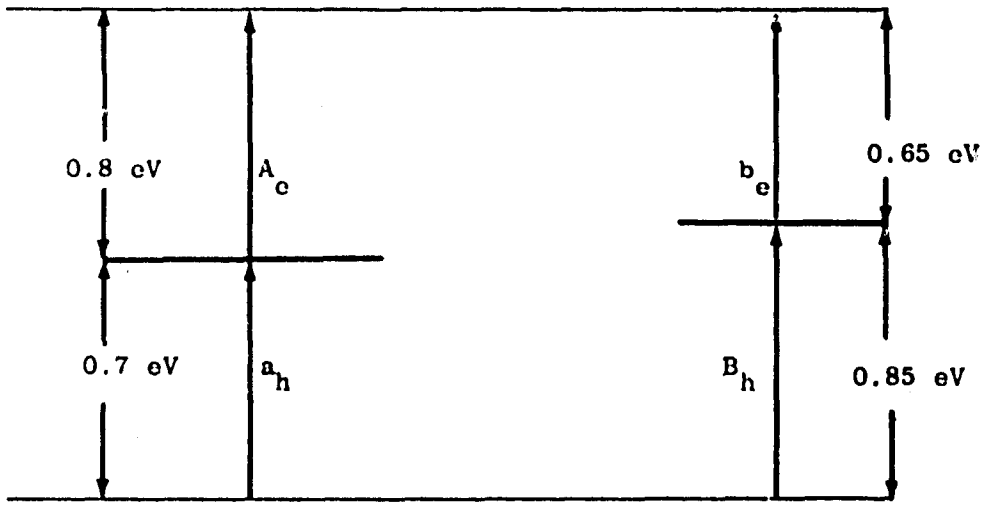

Photon Energy Range, eV	Major Transitions	Effects
$\hbar\omega < 0.65$	None	No photoconductivity
$0.65 < \hbar\omega < 0.7$	b_e	$\mu_H \approx \mu_n$
$0.7 < \hbar\omega < 0.8$	$b_e + a_h$	μ_H decreases
$0.8 < \hbar\omega < 0.85$	$b_e + a_h + A_e$	μ_H increases
$0.85 < \hbar\omega$	$b_e + a_h + A_e + B_h$	μ_H decreases

TABLE V-III

Peak Temperatures for Reported TSC Maxima for GaAs, ^{o}K

Haisty[a]	Present Work	Blanc et al.[b]	Approximate Trap Depth from $E_t = 23\ kT_m$, eV
95			0.19
115	116	107, 111	0.23
142	138	131, 136	0.28
160	158	156, 160, 162, 166, 168	0.31
193	189		0.38
208	212		0.42

[a]On "undoped semi-insulating" GaAs. R. W. Haisty, Appl. Phys. Letters 10, 31 (1967)

[b]On high-resistivity Cu-diffused GaAs. J. Blanc, R. H. Bube and H. E. MacDonald, J. Appl. Phys. 32, 1666 (1961).

Figure Captions

Figure V-1. Temperature dependence of the carrier concentration in n-type GaAs as measured in a helium dewar. Comparison with previous measurements shows a large discrepancy.

Figure V-2. Temperature dependence of the carrier mobility in n-type GaAs as measured in a helium dewar. Comparison with previous measurements shows a large discrepancy.

Figure V-3. Spectral response of photoconductivity in the extrinsic range for GaAs:Cr as-grown, after heating for 1 hour at 580°C, and after deformation at 580°C. Measurement at 80°K.

Figure V-4. Variation of photo-Hall mobility with exciting photon energy for GaAs:Cr as-grown, after heating for 1 hour at 580°C, and after deformation at 580°C. Measurements at 80°K.

Figure V-5. Results of a two-carrier analysis of the data given in Figures V-3 and V-4 using the mobility values given in the text.

Figure V-6. Optical quenching of photoconductivity spectra at 80°K for GaAs:Cr (1) as-grown, (2) after heating for 1 hour at 580°C, and (3) after deformation at 580°C.

Figure V-7. Thermally stimulated current curves for GaAs:Cr as-grown, after heating for 1 hour at 580°C, and after deformation at 580°C. Solid curves are for extrinsic (0.85 eV) photoexcitation, and dashed curves are for intrinsic (1.46 eV) excitation.

Figure V-8. Thermally stimulated current curves for deformed GaAs:Cr after the following photoexcitations: (1) white light, f = 1.0; (2) white light, f = 0.1; (3) white light, f = 0.013; (4) 0.85 eV radiation for 30 min. followed by 1.08-eV quenching radiation for 5 min.

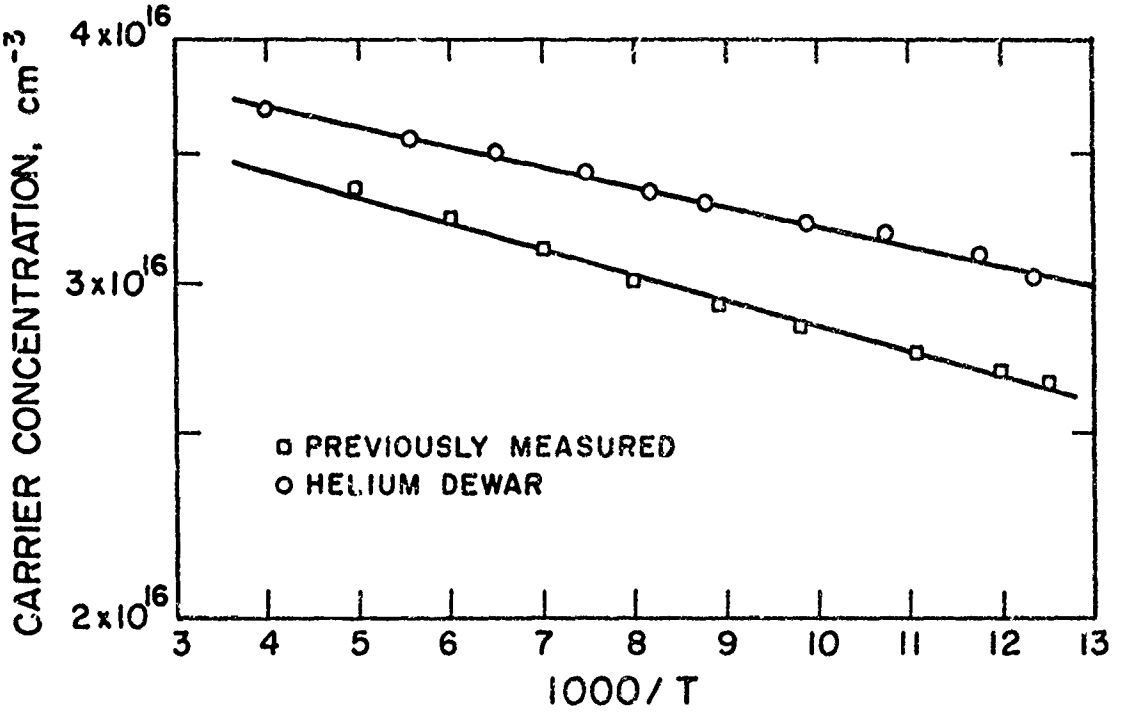

Figure V-1. Temperature dependence of the carrier concentration in n-type GaAs as measured in a Helium dewar. Comparison with previous measurements shows a large discrepancy.

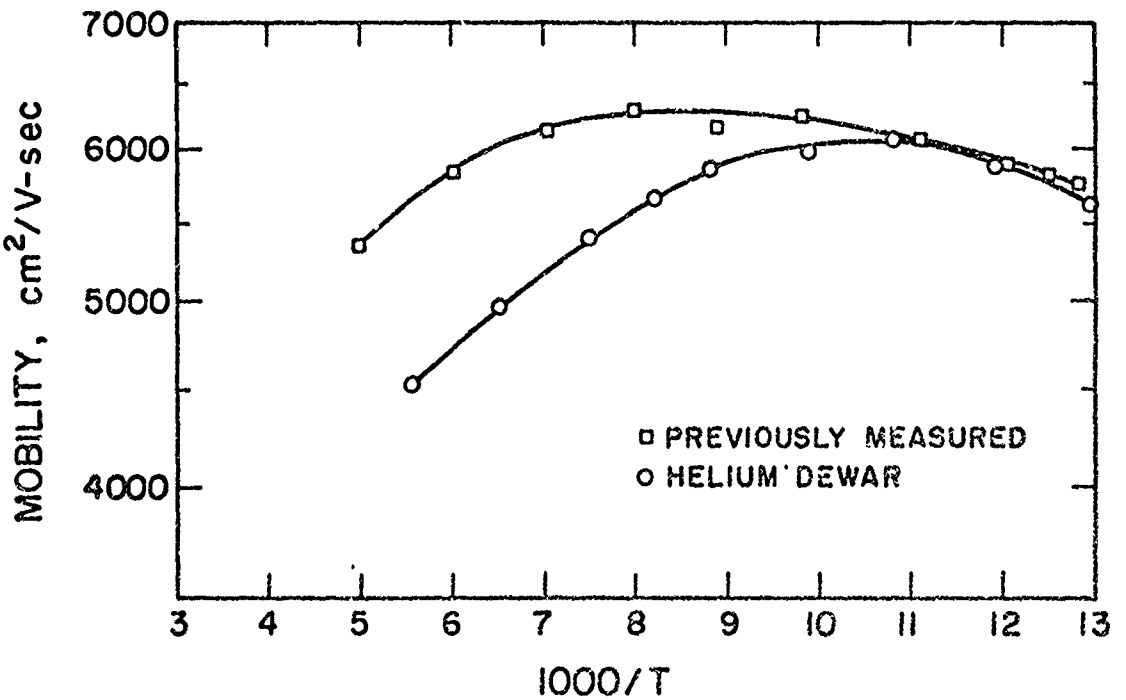

Figure V-2. Temperature dependence of the carrier mobility in n-type GaAs as measured in a Helium dewar. Comparison with previous measurements shows a large discrepancy.

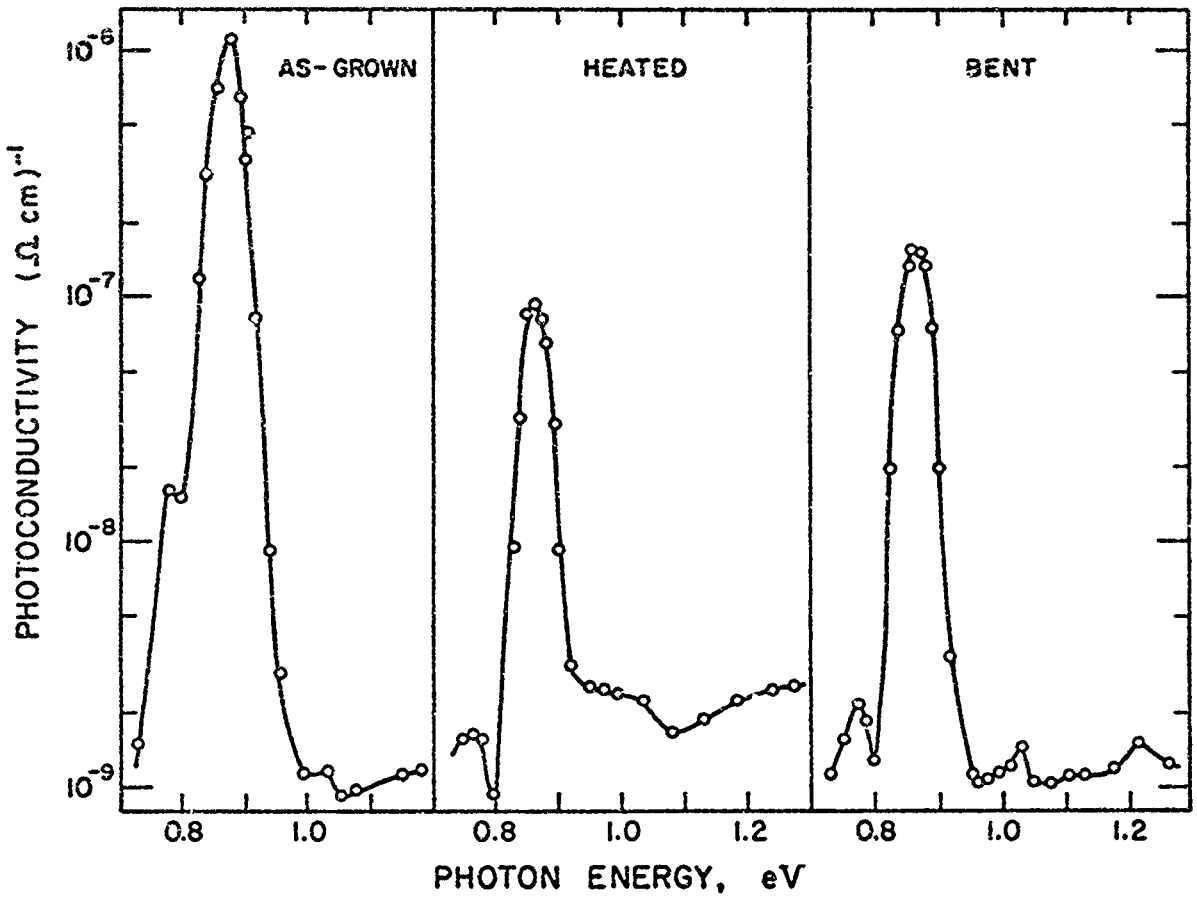

Figure V-3. Spectral response of photoconductivity in the extrinsic range for GaAs:Cr as-grown, after heating for 1 hour at 580°C, and after deformation at 580°C. Measurements at 80°K.

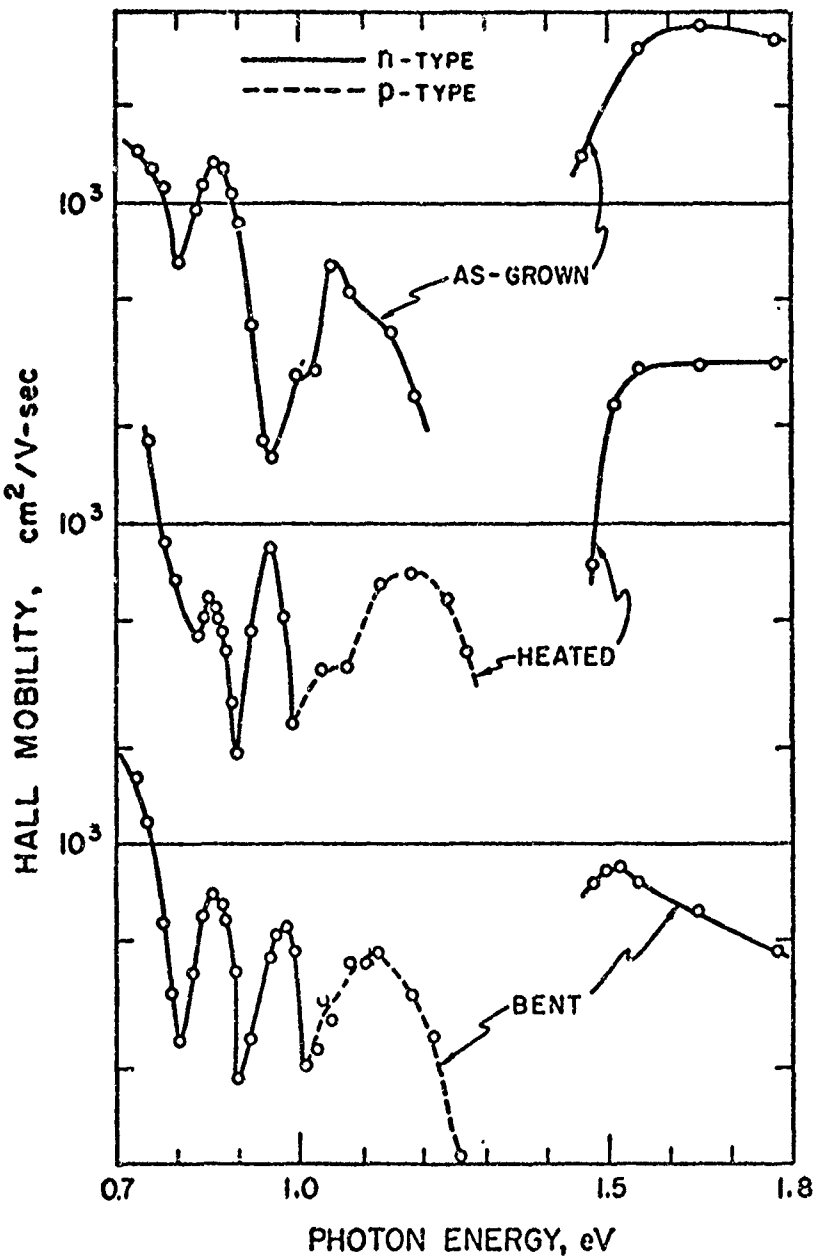

Figure V-4. Variation of photo-Hall mobility with exciting photon energy for GaAs:Cr as-grown, after heating for 1 hour at 580°C, and after deformation at 580°C. Measurements at 80°K.

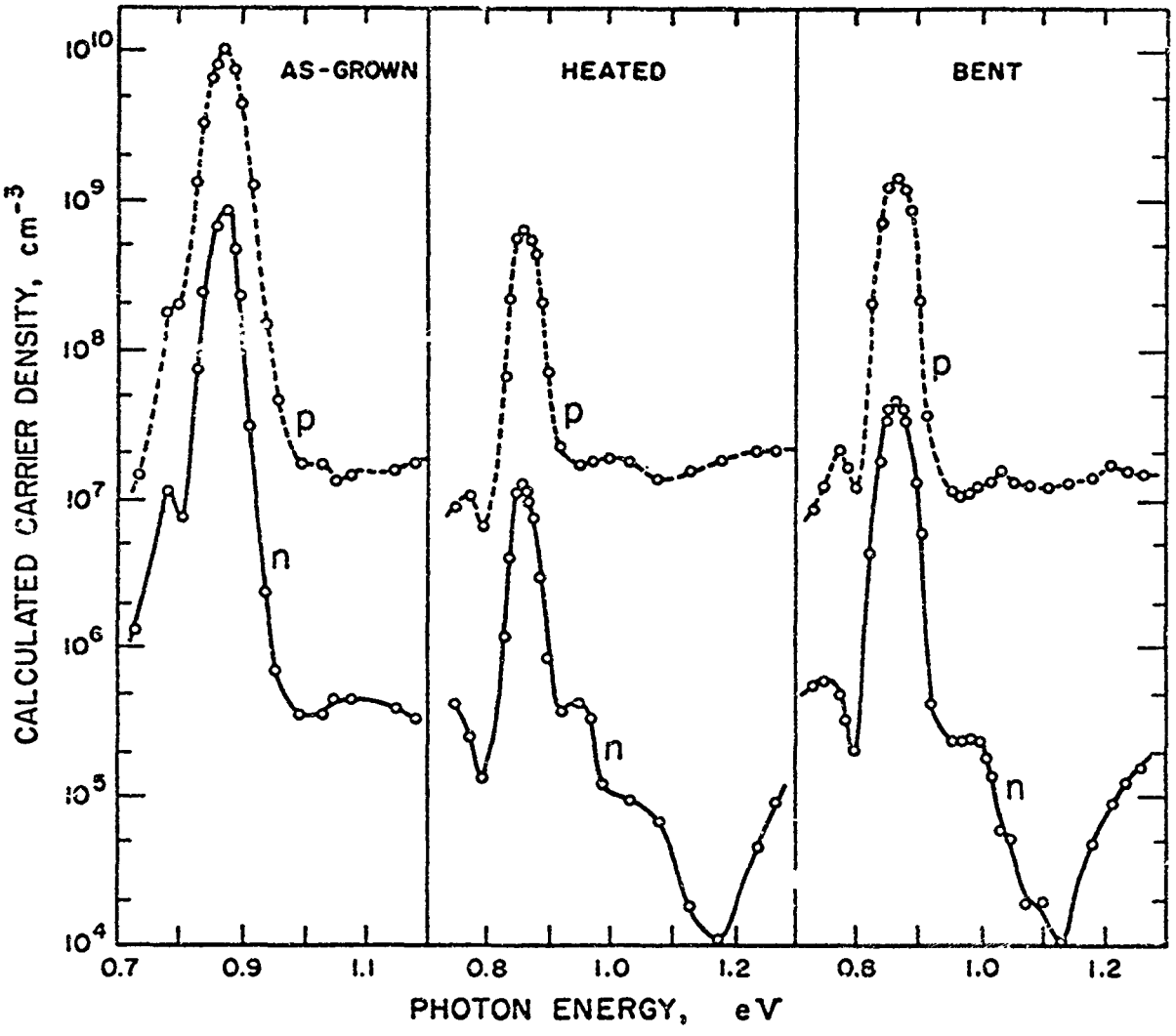

Figure V-5. Results of a two-carrier analysis of the data given in Figures V-3 and V-4 using the mobility values given in the text.

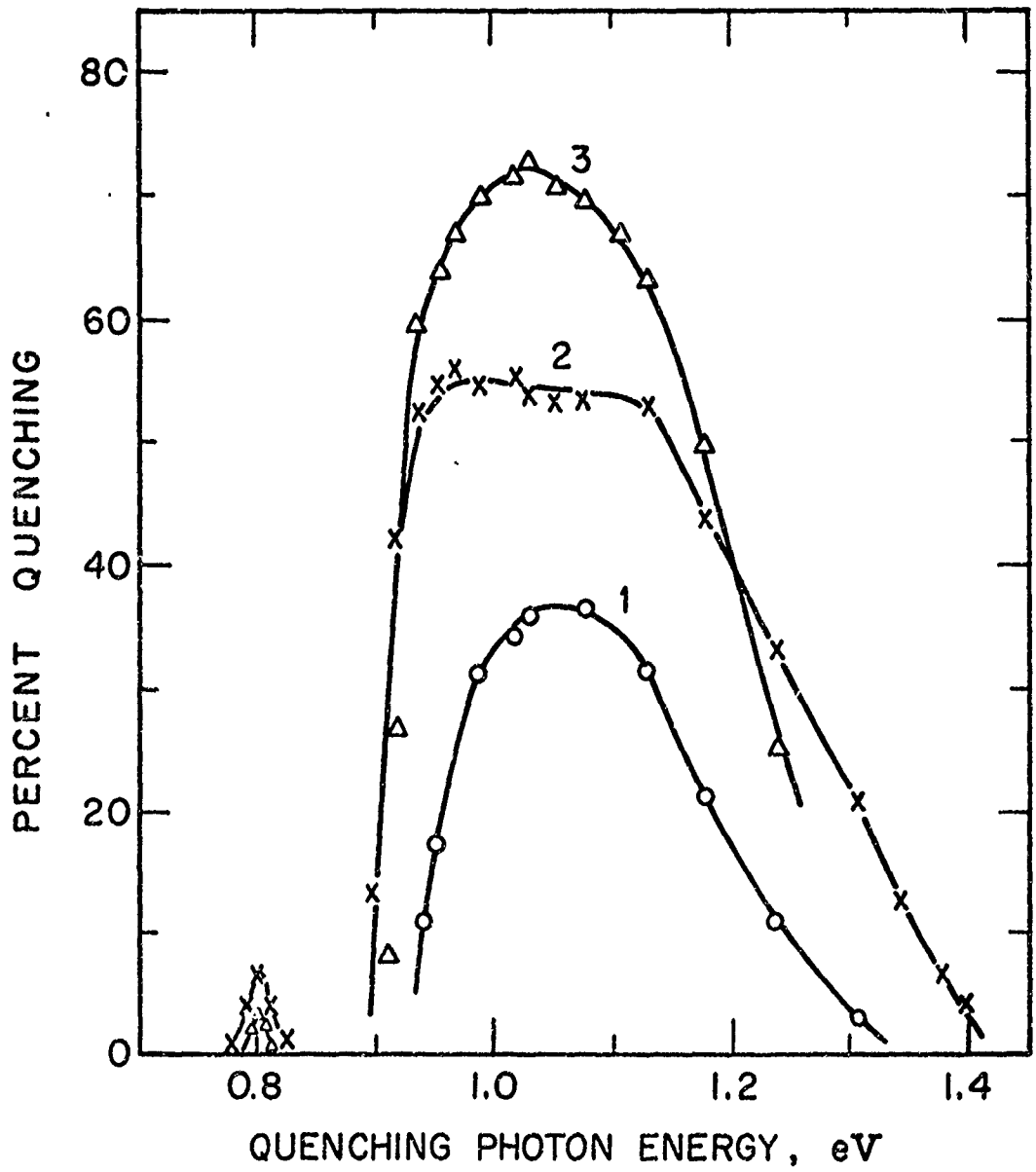

Figure V-6. Optical quenching of photoconductivity spectra at 80°K for GaAs:Cr (1) as-grown, (2) after heating for 1 hour at 580°C, and (3) after deformation at 580°C.

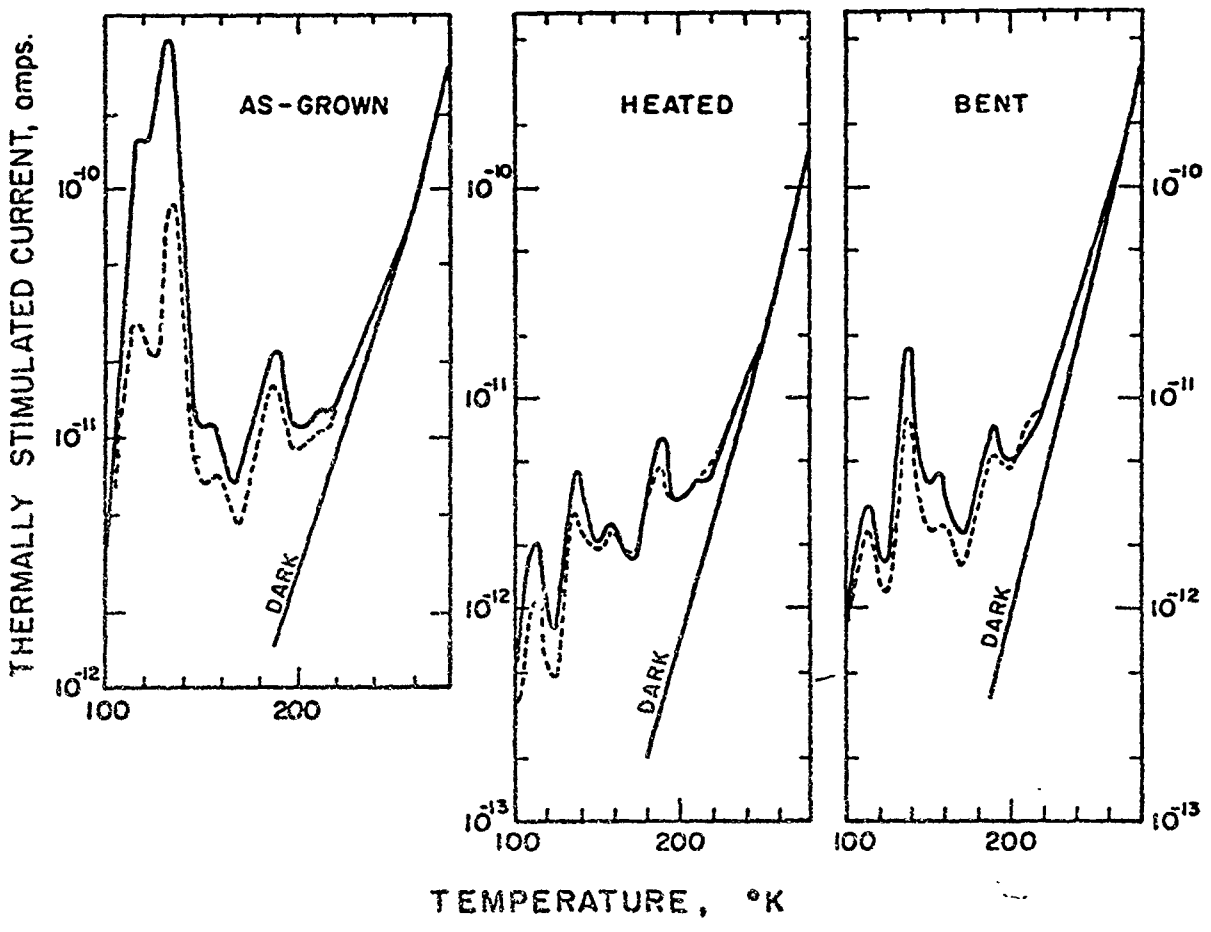

Figure V-7. Thermally stimulated current curves for GaAs:Cr as-grown, after heating for 1 hour at 580°C, and after deformation at 580°C. Solid curves are for extrinsic (0.85 eV) photoexcitation, and dashed curves are for intrinsic (1.46 eV) excitation.

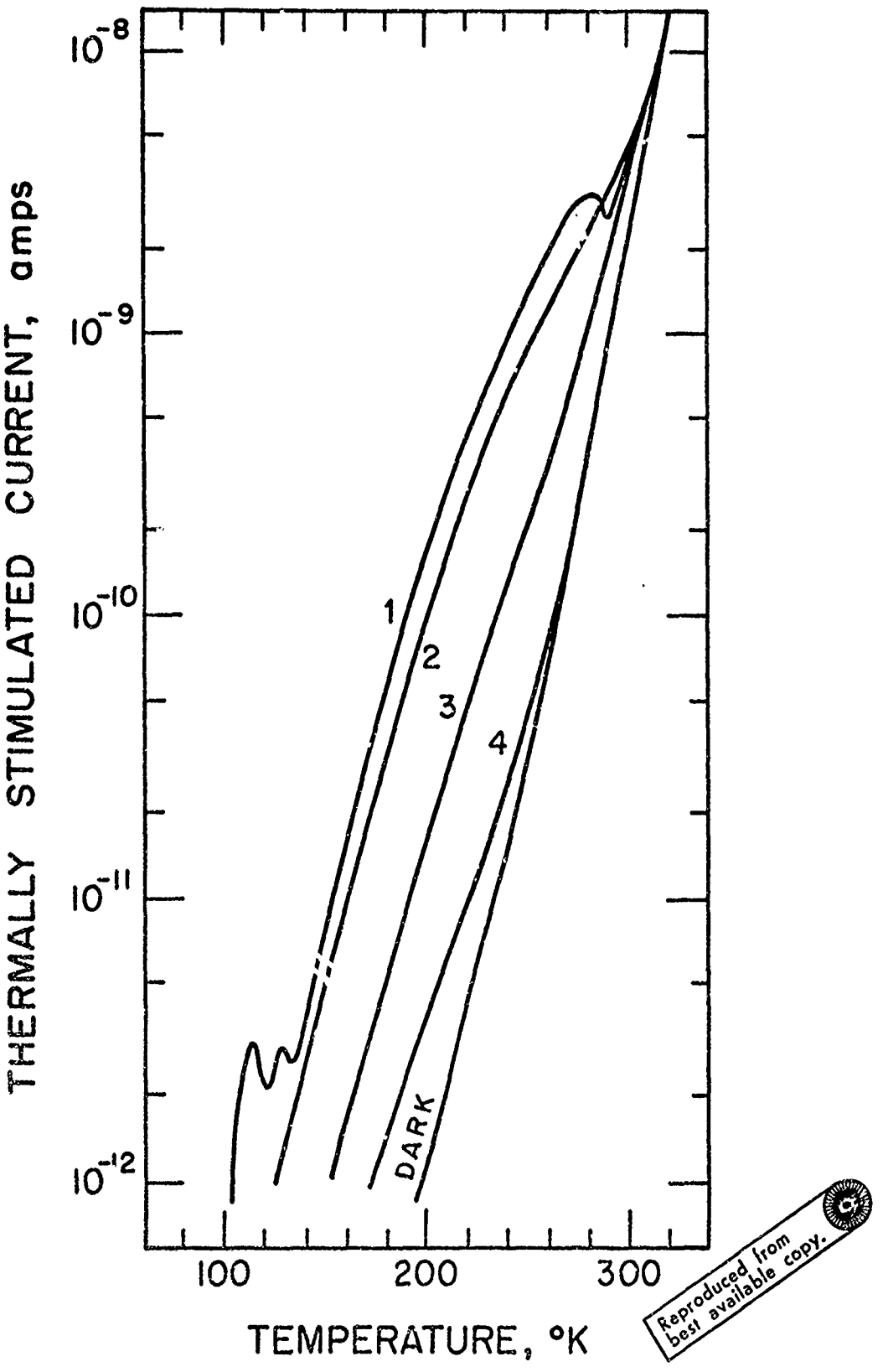

Figure V-8. Thermally stimulated current curves for deformed GaAs:Cr after the following photoexcitations: (1) white light, f = 1.0; (2) white light, f = 0.14; (3) white light, f = 0.013; (4) 0.85-eV radiation for 30 min. followed by 1.08-eV

VI. SCIENTIFIC ASPECTS OF SEMICONDUCTOR CRYSTAL PREPARATION

W. A. Tiller, B. Jindal and Hyo-Sup Kim.

A. PROGRAM OBJECTIVE

The objective of this investigation is to develop an understanding of the important interfacial parameters that govern the growth of GaAs crystals. The study includes the structure and energetics of the GaAs solid/Ga-As liquid interface as a function of (i) the composition of the liquid phase and (ii) the orientation of the solid GaAs. In addition, the concentration distribution in the vicinity of the interface is to be calculated.

B. PROGRESS

In the previous studies, a semi-microscopic method was developed to determine the structure and energetics of the solid-liquid solution interfaces for the III-V compounds, and sample calculations were made for the Ga-As system by using simple parametric interatomic interaction functions. The most recent progress falls into three categories:

1. Average Atomic Interaction Energy for Ga-As Liquid Solution

Stressing the importance of accurate knowledge concerning the interatomic interaction energies in our study, we have sought to construct more suitable interaction energy functions for the liquid solution than for those developed previously. Without splitting the energy function into individualized components, average atomic interaction energy functions have been determined in the Morse potential function form at given concentrations by using the available data on atomization energies, average atomic positions, and compressibilities. The parameters for the

functions were found to exhibit a satisfying self-consistency and are tabulated in Table VI-I.

2. Distribution of the Interaction Energies in the Interface Region

More details on the quasi-chemical contributions have been studied using a similar method to that introduced in previous reports. The solid-liquid interaction energies, ΔE_{SL}, and the excess energies, ΔE^{X}, associated with the formation of the planar interface at each layer on the liquid side of the interface region, have been calculated for different concentrations along the liquidus line and for different orientations of the crystal. The energy distributions for (111A and B)/liquid solution are tabulated in Table VI-II.

3. Relaxation of the First Layer Spacing at the Interface.

Minimizing the total interaction energies, one can determine the relaxed (equilibrium) spacing of the atomic layers at the interface region. The first layer spacings, d_I, and the variation of the interaction energies, ΔE^{X}, due to the relaxation have been calculated and tabulated in Table VI-III.

C. FUTURE WORK

Using the composition and orientation dependence of interface adsorption, the situation at layer edges will be evaluated to determine both interfacial energy and interface attachment kinetics as a function of orientation and liquid composition. From the edge energy aspects, one can evaluate the ease or difficulty of creating layer edges at certain orientations. From the density of edge kinks and adsorbed Ga atoms, one can evaluate the driving forces needed for motion of the layer edges

along faces of different orientations and along different directions in those faces.

In addition, using a recent theoretical advance relating to the creation of interfaces during phase transformations, the stability of different faceted interfaces in the GaAs system will be evaluated and a quantitative condition governing their breakdown developed. Using an experimental procedure involving the growth of bulk GaAs from solution at different temperatures and different supersaturations, this instability condition will be experimentally tested. The results of this experimental theoretical correlation should be directly applicable to the epitaxial growth of GaAs layers.

TABLE VI-I

The atomic interaction parameters in the standard Morse potential function form for the liquid Ga-As solution.

X_{AS}(atomic fraction)	$\phi°$(e.v.)	$\alpha(A^{-1})$	R°(A)
0.00	0.203976	0.857234	3.589085
0.10	0.174711	0.767667	3.733942
0.20	0.156923	0.709857	3.829738
0.30	0.147839	0.679004	3.872832
0.40	0.140965	0.655274	3.896439
0.50	0.141090	0.656150	3.869273
0.60	0.146616	0.675621	3.806210
0.70	0.158089	0.712791	3.715169
0.80	0.176336	0.765399	3.612313
0.90	0.195202	0.810284	3.552667
1.00	0.210711	0.837179	3.573365

TABLE VI-II

The solid-liquid interface energy (E_{SL}) and the excess energy (E^X) due to the formation of the interface at each atomic layer in the liquid phase at the interface region.

(a) The solid (111A)/liquid solution interface:

X_{AS}(atom. fract.)		1st layer	2nd layer	3rd layer	4th layer	5th layer	6th layer
0.025	E_{SL}(erg/cm^2)	-798.4	-96.7	-17.9	-1.0	-0.1	0.0
	E^X "	1420.3	361.0	-17.9	-1.0	-0.0	0.0
0.050	E_{SL} "	-905.0	-111.5	-21.0	-1.2	-0.1	0.0
	E^X "	1309.7	362.5	-21.0	-1.2	-0.0	0.0
0.100	E_{SL} "	-1091.8	-140.8	-27.3	-1.7	-0.2	0.0
	E^X "	1087.9	355.3	-27.3	-1.7	-0.0	0.0
0.200	E_{SL} "	-1409.1	-193.1	-39.2	-2.8	-0.3	0.0
	E^X "	757.6	340.0	-39.2	-2.8	-0.0	0.0
0.300	E_{SL} "	-1672.4	-238.2	-49.6	-3.7	-0.5	0.0
	E^X "	503.5	320.3	-49.6	-3.7	-0.0	0.0
0.400	E_{SL} "	-1903.4	-279.4	-59.1	-4.7	-0.6	0.0
	E^X "	259.9	287.5	-59.2	-4.7	-0.0	0.0
0.500	E_{SL} "	-2102.7	-309.4	-65.9	-5.3	-0.7	0.0
	E^X "	73.7	259.2	-65.9	-5.3	-0.0	0.0

TABLE VI-II

(continued)

(b) The solid (111B)/liquid solution interface:

X_{AS}(atom. fract.)		1st layer	2nd layer	3rd layer	4th layer	5th layer	6th layer
0.025	E_{SL}(erg/cm^2)	-1297.2	-138.7	-18.9	-1.4	-0.1	0.0
	E^X "	921.5	319.1	-18.9	-1.4	-0.0	0.0
0.050	E_{SL} "	-1452.3	-159.1	-22.3	-1.8	-0.2	0.0
	E^X "	762.4	314.9	-22.3	-1.8	-0.0	0.0
0.100	E_{SL} "	-1713.7	-198.8	-29.4	-2.5	-0.3	0.0
	E^X "	465.9	297.2	-29.4	-2.5	-0.0	0.0
0.200	E_{SL} "	-2159.5	-268.5	-42.6	-3.9	-0.5	0.0
	E^X "	7.2	264.5	-42.6	-3.9	-0.0	0.0
0.300	E_{SL} "	-2533.3	-328.9	-54.3	-5.3	-0.6	0.0
	E^X "	-357.3	229.6	-54.3	-5.3	-0.0	0.0
0.400	E_{SL} "	-2860.6	-384.4	-65.4	-6.6	-0.8	0.0
	E^X "	-697.3	182.4	-65.4	-6.0	-0.0	0.0
0.500	E_{SL} "	-3154.2	-425.4	-72.8	-7.4	-0.9	0.0
	E^X "	-978.4	143.2	-72.8	-7.4	-0.0	0.0

TABLE VI-III

The relaxed first interphase spacing (d_I) and the relaxation effect on the excess energy (ΔE^X)

Orientation	X_{AS}	d_I(A)	ΔE^X(erg/cm^2)
(111A)/liquid	0.500	2.3442	-257.26
	0.400	2.3653	-207.19
	0.300	2.3939	-151.07
	0.200	2.4307	- 93.83
	0.100	2.4827	- 38.77
	0.050	2.5188	- 16.28
	0.025	2.5414	- 7.33
(111B)/liquid)	0.500	2.2543	-641.82
	0.400	2.2757	-532.94
	0.300	2.3044	-416.69
	0.200	2.3405	-292.31
	0.100	2.3908	-162.99
	0.050	2.4255	-101.17
	0.025	2.4478	- 69.97
(110)/liquid)	0.500	2.2067	-181.75
	0.400	2.2284	-135.47
	0.300	2.2572	- 86.34
	0.200	2.2939	- 40.03
	0.100	2.3456	- 5.53
	0.050	2.3811	- 0.04
	0.025	2.4037	- 3.06

VII. VAPOR-PHASE GROWTH OF AlN, GaN AND AlN-GaN SOLID SOLUTIONS

D. A. Stevenson and H. P. Maruska

A. PROGRAM OBJECTIVES

AlN is a wide bandgap (5.9 eV) semiconductor with an as-grown resistivity of about 10^{12} ohm-cm. Owing to the lack of a center of symmetry in its wurtzite crystal structure, it exhibits piezoelectricity and, thus, is of interest as an ultrasonic transducer material. Little information is available concerning its electrical and optical properties.

GaN has a bandgap of 3.5 eV, and much more interest has developed recently in this material. Green and blue electroluminescent diodes have been fabricated in i-n junction layers of GaN. The n-layer is unintentionally doped but always contains more than 10^{18} electrons/cm^3 (probably due to a native defect) while the insulating (i) layer is produced by compensating with the deep acceptor zinc.

It is of interest to study solid solutions of AlN and GaN. Both materials are hexagonal (wurtzite) with similar lattice parameters, and the radii (either ionic or covalent) of Al and Ga are almost identical. Therefore, it is reasonable to expect that a continuous series of solid solutions should form. However, no report of these has ever been made in the literature. Since the resistivity of "undoped" GaN is 10^{-3} ohm-cm, the resistivity should change by 15 orders of magnitude for the series of solid solutions formed between GaN and AlN. If these can be formed, the carrier concentration should also drop through the series by many orders of magnitude, and a useful range of about 10^{14}-10^{15} electrons/cm^3 may be found.

B. PROGRESS

To pursue this study, an open flow straight-tube vapor growth system has been assembled. This type of apparatus has already been used to produce single-crystal epitaxial layers of both GaN and AlN on sapphire substrates. It is also capable of producing most of the other III-V compound semiconductors, such as GaAs, GaP, InAs and InP. In this system, shown schematically in Figure VII-1, the Group V element (such as nitrogen) is introduced in the form of its hydride (NH_3) and the Group III material is placed in its elemental form in a boat inside the furnace area. Anhydrous HCl is passed over this boat, resulting in the formation of the volatile monochloride, which passes downstream to react with the Group V element at the substrate. The reaction occurs in a 1-1/4" quartz tube, with three separately controlled furnace zones. The Group III element is placed in the first zone, while the hydride passes through this zone inside a 1/4" tube so that it does not contact the boat. The gases mix in the center zone, and deposition occurs in the third zone. The substrate is carried into this zone, on a long ground quartz rod which is moved into and out of the furnace area through a true-bore bearing. The substrate is placed parallel to the gas stream. The quartz tube is fitted with a large valve just outside the furnace area, so that substrates may be introduced or removed while the furnaces are at temperature. A hydrogen atmosphere is maintained in the growth-tube. The hydrogen is palladium diffused. The effluent gases are bubbled through halocarbon oil, and the exhaust chimney is open to the atmosphere. All the gas flows are monitored on flow meters.

After the apparatus was completed and tested, a number of samples

of AlN were grown. They all proved to be polycrystalline. Conditions were then changed to grow GaN, and these runs were successful, in that typical colorless single crystal epitaxial layers were produced. Next, a small quantity of aluminum was mixed into the gallium boat. A number of interesting samples were then produced. One epitaxial layer showed a change in electrical properties from high to low conductivity across the width of the sample. The upstream end showed high conductivity (the sample was about 1/2" wide). The growth tube was protected with a tungsten liner, and highly oriented polycrystalline material was deposited on this liner. This material also showed a graded resistivity, and small samples picked from various positions in the tube were taken for optical absorption measurements. It was found that sharp absorption edges, from 3650 Å (GaN) to 2100 Å (AlN) were present. Representative pieces for any intermediate wavelength could be found. The material grown on the liner right at the exit port of the ammonia inlet tube absorbed at 3650 Å, while the absorption moved monotonically to 2100 Å, as samples were taken from positions further upstream toward the Al-Ga source. Evidently, some ammonia must have diffused upstream, and since the aluminum-ammonia reaction is much more energetically favorable than the gallium-ammonia reaction, it appears that the AlN is deposited first, with GaN content increasing downstream. The optical absorption measurements indicate that the complete series of solid-solutions between AlN and GaN has been formed. However, x-ray diffraction only showed the presence of GaN and AlN in the samples. No intermediate lattice parameters were found. This would indicate a mechanical mixture. But a mechanical mixture cannot have the optical properties described above. An emission spectrographic analysis of the samples showed that they were

indeed only compounds of aluminum, gallium and nitrogen, so the adsorption is not being caused by some spurious unknown material. We have tentatively surmised that the samples may be amorphous (with the crystals grown during the initial pure GaN and AlN runs.)

C. FUTURE PLANS

The apparatus is being modified so that the Al and Ga sources can be placed in separate tubes with separate controls. Substrates will be placed between the ammonia inlet tube port and the source boat so that the grown layers can be easily removed, since the tungsten liner itself is difficult to remove, and requires dismantling the system.

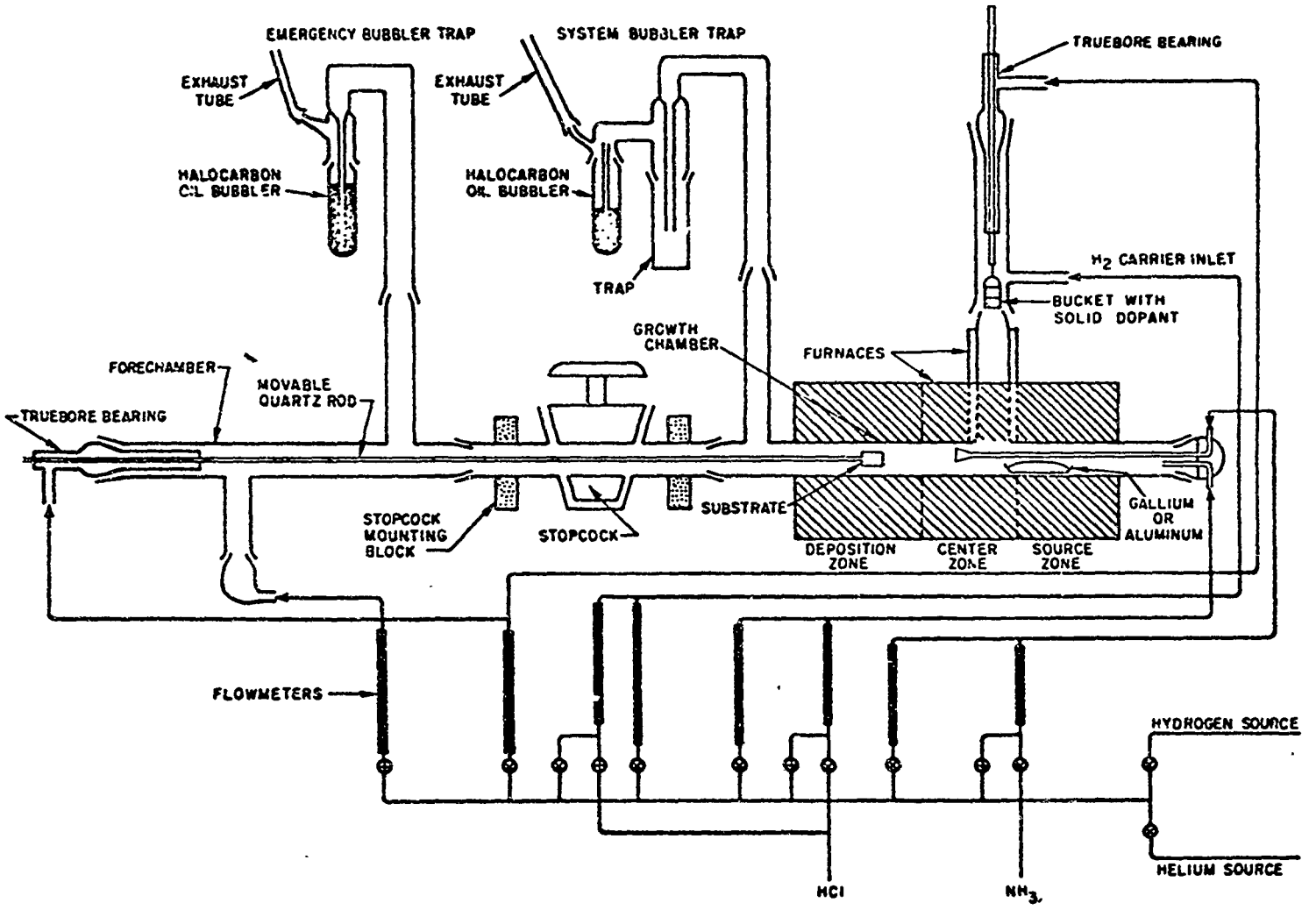

Figure VII-1. System for Preparing Gallium and Aluminum Nitride.